NORTHWESTERN UNIVERSITY

An Atomic-Scale X-ray View of Functional Oxide Films

A DISSERTATION

SUBMITTED TO THE GRADUATE SCHOOL

IN PARTIAL FULFILLMENT OF THE REQUIREMENTS

for the degree

DOCTOR OF PHILOSOPHY

Field of Materials Science and Engineering

By

I-Cheng Tung

EVANSTON, ILLINOIS

December 2014

ABSTRACT

An Atomic-Scale X-ray View of Functional Oxide Films

I-Cheng Tung

Complex oxides are a class of materials that exhibit a wide variety of physical functionalities, such as ferroelectricity, colossal magnetoresistance, mulitferroicity and superconductivity, with outstanding potential for meeting many of our technological demands. The primary objective of this dissertation is to understand the structural and electronic behavior of complex oxide ultrathin films subjected to confinement, lattice misfit and broken symmetry at the interface. In complex oxide ultrathin films, heteroepitaxial synthesis has evolved into a reliable strategy to engineer orbital-lattice interactions in correlated materials and led to new and entirely unexpected phenomena at their interfaces. I experimentally demonstrated that the bulk crystal symmetry directs the atomic and orbital responses adopted by coherently strained ultrathin films of $RNiO_3$ (R = La, Nd) with detailed X-ray scattering, polarization-dependent X-ray absorption spectroscopy (XAS) and supported by a mathematical point group symmetry analysis, found that strain-stabilized phases maintain a "memory" of their bulk state. This topic, however, touched only upon the properties of such films. A fundamental challenge in this research area occurs before this and centers around the understanding of how to create high-quality films with arbitrary configurations. A longstanding challenge in the oxide thin film community has been the growth of $A_{n+1}B_nO_{3n+1}$ Ruddlesden-Popper (RP) compounds. To

understand this problem, we have utilized a newly constructed oxide MBE with *in situ* synchrotron X-ray scattering capability to study the initial growth of such layered oxides and track the dynamic evolution. X-ray results are supported by theoretical calculations that demonstrated the layered oxide films dynamically rearrange during growth, leading to structures that are highly unexpected, and suggest a general approach that may be essential for the construction of metastable RP phases with performing the first atomically controlled synthesis of single-crystalline $La_3Ni_2O_7$. By building upon this knowledge, I have completed the first to date study of *in situ* surface X-ray scattering during homoepitaxial MBE growth of $SrTiO_3$, which demonstrates codeposition is consistent with a 2D island growth mode with $SrTiO_3$ islands, but shuttered deposition proceeds by the growth of SrO islands which then restructure into atomically flat $SrTiO_3$ layer during the deposition of the TiO_2. From this point, we have conducted a detailed microscopic study of epitaxial $LaNiO_3$ ultrathin films grown on $SrTiO_3$ (001) by using reactive MBE with *in situ* surface X-ray diffraction and *ex situ* soft XAS to explore the influence of polar mismatch on the resulting structural and electronic properties. Overall, this thesis highlights the power of artificial confinement to harness control over competing phases in complex oxides with atomic-scale precision.

Approved:

Professor Michael J. Bedzyk

Department of Materials Science and Engineering

Northwestern University

Evanston, Illinois

Acknowledgements

It is a great pleasure to thank the many people who made this thesis possible. First, I would like to thank my advisors, Prof. Michael Bedzyk and Dr. John Freeland. I have learned a great deal from working with each of them, and I am grateful for their support throughout my time at Northwestern University. I thank Prof. Bedzyk for impressing upon me the importance of conducting research with an acute attention to detail. express my sincere gratitude to my advisor, Dr. John Freeland at Argonne because of his selfless guidance throughout my graduate studies. I greatly appreciate his mentoring based on trust and friendship, working with him is an unforgettable experience. I also appreciate Prof. Vinayak Dravid and Prof. James Rondinelli for serving on my final exam committee.

I am grateful for the opportunity I have been given to work in the Advanced Photon Source (APS) at Argonne National Laboratory. I have benefited not only from access to these facilities, but also from working with the scientists and postdocs there. I would like to acknowledge the following collaborators at Argonne, Drexel University, and University of Wisconsin–Madison for their valuable contributions to this dissertation. I especially thank Dr. Dillon Fong (Materials Science Division, Argonne) for his tireless and invaluable work on the oxide molecular-beam epitaxy (MBE) project. I thank Dr. Prasanna Balachandran and Prof. James Rondinelli for the first-principles calculations and fruitful discussions for the RNiO3 studies. I thank Dr. Guangfu Luo and Prof. Dane Morgan (U.W.–Madison) for providing theory calculations for the oxide MBE project. In addition, I need to thank Dr. June Hyuk Lee, Dr. Seohyoung Chang, and Dr. Yang Liu for the precious partnership in

all experiments, and especially Dr. June Hyuk Lee for enriching my knowledge in reactive MBE. Besides, Dr. Christian Schlepütz, Dr. Zhan Zhang, and Dr. Hawoong Hong at sector 33 who provided important suggestions and helps in setting up X-ray scattering experiments. I am very thankful for having been a member of the Magnetic Materials Group and I appreciate every single person in this group.

I also would like to give special thanks to my former and present Bedzyk group members, including Dr. Yuan-Chieh Tseng, Dr. Phillip Lin, Dr. Jeff Klug, Dr. Curtis Leung, Dr. Martin McBriarty, Dr. Sudeshna Chattopadhyay, Bor-Rong Chen, Li Zeng, Xiao Chen, Liane Moreau, Gavin Campbell, Dr. Parasmani Rajput, Changrui Gao, Kurinji Krishnamoorthy, Dr. Guennadi A Evmenenko, and Boris Harutyunyan for their friendships and discussions about life. I especially give thanks to Dr. Zhenxing Feng, Dr. Jonathan Emery, Dr. Sumit Kewalramani, and Dr. Sven Stoltz for sharing their knowledge and helping me with many X-ray experiments.

Finally, I would like to dedicate this dissertation to my dear parents and family in Taipei, Taiwan—it is their encouragements that gave me the initial motivation to study in the U.S. and their endless support and strong encouragement to continue my degree.

Above all I also would like to express my great gratitude to Shin-Huey for joining my life at Northwestern and for her love, sacrifices and support in my graduate study, making my life never alone. I could not have done this without you. Nor would I wish to.

Table of Contents

List of Tables

List of Figures

CHAPTER 1

Introduction

Complex oxides are a class of materials that exhibit a wide variety of physical functionalities, ranging from features as diverse as ferroelectricity and colossal magnetoresistance to mulitferroicity and high-temperature superconductivity [1], with immense scientific richness and outstanding potential for meeting many of our technological demands because of a variety of strong interaction between charge, spin, orbital, and lattice with competing energy scales. The combination of several such materials into artificial heterostructures has led to new and entirely unexpected phenomena at their interfaces.

Strains can exist in thin films when one material is deposited on another [2], imparted via lattice mismatch and differences in thermal expansion behavior between the film and the substrate or arising from defects formed during film deposition. The structural and physical properties of thin films can be significantly altered from those of the bulk by epitaxial strain [3, 4, 5, 6]. It is well established that strain can significantly affect the properties of high-Tc superconductors [7] and colossal magnetoresistive compounds [8, 9]. Therefore, strains provide an opportunity to modify particular properties of a thin film material, and strain engineering is an appealing route to controlling electronic [10], ferroelectric [5], and structural properties in complex oxide heterostructures [11].

Owing to the remarkable progress in achieving high-quality coherent perovskite oxide thin films and superlattices, heteroepitaxial synthesis has evolved into a reliable strategy to engineer orbital-lattice interactions in correlated oxide materials [12, 13]. In ultrathin

film perovskite oxides, strain fields at the thin film-substrate interface directly tune the local electronic states of the correlated transition metal (TM) d orbitals, from which novel functionalities and phases prohibited in bulk phases are stabilized [14, 15, 16]. Rotationally distorted ABO_3 oxides, in particular, are susceptible to strain-induced changes in bond lengths and bond angles, which modify the crystal field symmetry and lead to differential orbital occupation (polarization). However, despite the recent progress, there is very limited experimental understanding of factors conducive to large orbital polarizations [17, 18, 19, 20, 21]. What governs the orbital-lattice response of the BO_6 units to the substrate-induced heteroepitaxial constraints? Isolating the principal interactions remains challenging: The orbital occupation can be significantly influenced by elastic strain (substrate–film lattice mismatch), octahedral rotation dissimilarities (crystallographic symmetry mismatch), and electrostatic (polarity) mismatch [22].

Moreover, functional materials based on complex oxides in thin film form offer new and exciting strategies with potentially transformative properties for meeting many of our outstanding challenges in the field of energy technology [23, 12, 22]. The atomic-level synthesis of functional oxides and an understanding of their growth behavior provide opportunities to explore and control the intriguing properties of artificial layered oxide heterostructures [24, 25, 26]. Unfortunately, synthesis of such oxide films can be a major challenge even when utilizing reactive molecular-beam epitaxy (MBE), the most precise and powerful deposition technique that is often regarded to allow the construction of materials atomic plane by atomic plane and permits delivery of the cation fluxes to the substrate either at the same time (codeposition) or separately (shuttered deposition) [27].

While the mechanisms of epitaxial growth for thin films comprised of metals or semiconductors have long been the focus of study [28, 29, 30], the science of oxide heterostructure synthesis remains very much in a state of development [31]. The mobilities of various species on the surface can vary widely [32, 33], and the local composition depends on the relative cation and oxygen reaction rates at interfaces [34], which in turn are sensitive to the surface structure [35], strain [36, 37], crystal orientation, and the effects of polarity [38, 39]. In doped systems, cation segregation to the interfaces has been observed to occur dynamically during growth, with a driving force that can depend on the growth environment [40, 41, 42, 43]. Despite these challenges, researchers have now discovered many examples of remarkable behavior in oxide heterostructures not easily predicted from the bulk properties of the oxide [44], providing a tremendous opportunity for the development of new technologies [45, 46, 47] and new materials [48, 13, 49]. However, the physics of these systems are ultimately subject to a myriad of both intrinsic and extrinsic factors [50], and it behooves the crystal grower to understand how these materials form at the atomic-level to improve control over synthesis as well as clarify their fundamental structure-property relationships.

Oxide molecular beam epitaxy (MBE) is a growth technique that permits delivery of the cation fluxes to the substrate either at the same time (codeposition) or separately (shuttered deposition) [27]. The latter allows manipulation of the cation sublattice on a monolayer level, permitting the growth of layered oxide materials [51] and studies on the effects of cation ordering on ground state properties and phase transitions [52, 53, 54]. Although either technique can be used to grow simple perovskites of the form ABO_3, the processes occurring during synthesis can be quite distinct. The usual in situ deposition

monitor, reflection high energy electron diffraction (RHEED), provides direct information on surface roughness evolution during growth, but due to the strong interaction between the high energy electrons and the growing material, it has been difficult to quantitatively detail the atomic mechanisms taking place at the surface. A report by Haeni et al. [55] has shown that the observed growth oscillations with RHEED at the specular spot can differ substantially from sample to sample, even for the homoepitaxial growth of $SrTiO_3$(001), highlighting a fundamental lack of understanding of what takes place during oxide deposition.

The organization of this thesis is described as follows: Chapter 2 provides background information about strain engineering in epitaxial oxide thin films and MBE. The primary X-ray characterization methods used in this dissertation are introduced in Chapter 3. Chapter 4 describes the structural and orbital properties of strained $RNiO_3$ (R = La, Nd) epitaxial thin films grown on $SrTiO_3$ (001) substrates which is based on the manuscript published in *Physical Review B* in 2013 [56]. Chapter 5 describes the dynamic layer rearrangement during growth of layered oxide films by reactive MBE, leading to structures that are highly unexpected on the basis of the intended layer sequencing which is based on the manuscript published in *Nature Mater* in 2014 [57]. Chapter 6, the highlight of this dissertation, consists of homoepitaxial growth of $SrTiO_3$ by utilizing reactive MBE studied with *in situ* time-resolved X-ray specular reflectivity and surface diffuse X-ray scattering. Chapter 7 describes the effect of polar discontinuity on the MBE growth of epitaxial $LaNiO_3$ thin films on $SrTiO_3$ (001) subsrates. Chapter 8 concludes this dissertation with a summary of the results and suggests future work that could be performed to further understand the thin film growth mechanism.

CHAPTER 2

Background

2.1. Strain Engineering in Oxide Thin Films

Owing to the remarkable progress in achieving high-quality coherent perovskite oxide thin films and superlattices, heteroepitaxial synthesis has evolved into a reliable strategy to engineer orbital-lattice interactions in correlated oxide materials [12]. In ultrathin film of perovskite oxides, strain fields at the thin film-substrate interface directly tune the local electronic states of the correlated transition metal (TM) d orbitals, from which novel functionalities and phases prohibited in bulk phases could be stabilized [14, 15, 16]. The strain state in thin films can be manipulated by epitaxially growing on the appropriate substrates.

Epitaxial strain can significantly alter the structure and physical properties of a material, and even stabilize a phase not present in bulk which has been extensively studied in ferroelectric materials [4, 3, 5, 6]. For example, perovskite oxide thin films under biaxial strain showed enhanced ferroelectric polarization [4], hundreds of degrees shift in Curie temperatures, and room temperature ferroelectricity in non-ferroelectric materials [3].

Strains can be imparted into thin films through differences in lattice parameters and thermal expansion behavior between the film and the underlying substrate [5]. Utilizing lattice mismatch between the substrate and the film, coherent films can be grown to

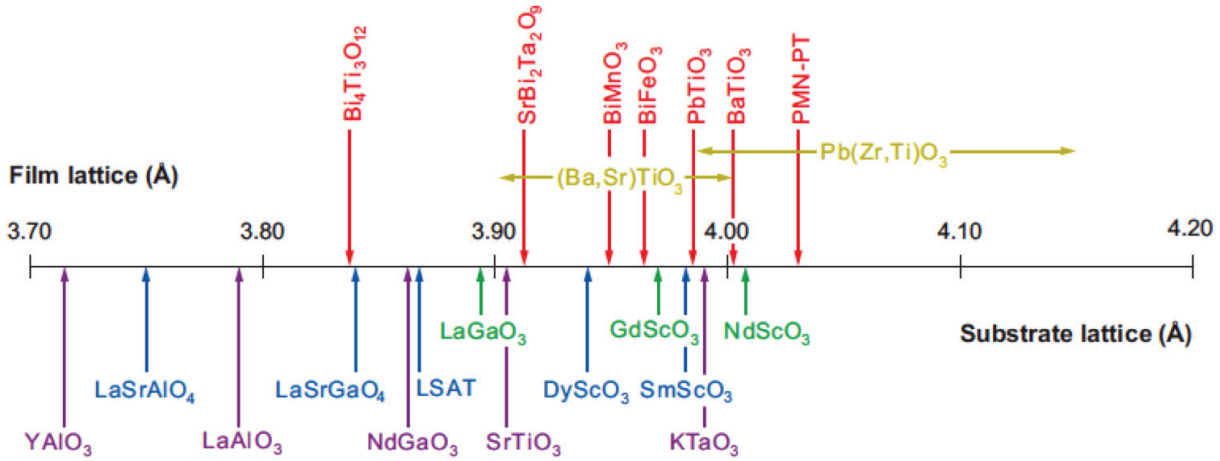

Figure 2.1. A number line showing the pseudotetragonal or pseudocubic a-axis lattice constants (in Å) of some perovskites of current interest (above the number line) and some commercially available perovskite and perovskite-related substrates (below the number line). This graph is reproduced from Ref. [5].

impose uniform strain on films that do not exceed their critical thickness where they start to relax. Fully coherent, epitaxial thin films have the advantage that high densities of threading dislocations are avoided. The strain field around dislocations in the film locally makes its ferroelectric properties inhomogeneous and often degraded.

In order to achieve fully strained films, the appropriate high-quality substrates are crucial. The high-quality substrates need structurally and chemically compatible with the films. Chemical incompatibility can result in interfacial reaction layers or interdiffusion of unwanted elements into the films. Structural incompatibility also can lead to strain relaxation of the films. The commercially available high quality oxide substrates and corresponding perovskite thin films are shown in Figure 2.1 [5].

Additionally, methods to prepare atomically defined surfaces are critical to achieve strained film. For (001)-oriented $SrTiO_3$ substrates, a TiO_2-terminated (001) $SrTiO_3$

surface has been perfected by Koster et al. [58]. and has been extensively used in the growth of $RNiO_3$ (R = La, Nd), $SrTiO_3$, $Sr_{n+1}Ti_nO_{3n+1}$, and $La_{n+1}Ni_nO_{3n+1}$ thin films in this work. For rare earth substrates ($DyScO_3$, $NdScO_3$, and $GdScO_3$), atomically sharp ScO_2-terminated surfaces have been recently reported [59].

2.2. Molecular beam epitaxy

The desire to engineer materials at increasingly smaller levels has led to the development of several thin film growth techniques capable of controlling the deposition of materials on an atomic scale. Molecular-beam epitaxy (MBE) is a thin film deposition technique that utilizes the highly-controlled thermal evaporation of atoms or molecules from individual cells in a high vacuum environment. Beams of molecules generated by each source cell react on the substrate surface to produce an epitaxial thin film. The temperature of the source cell controls the molecular beam flux and a shutter located in front of the cell controls the duration of deposition. In comparison to other deposition techniques such as pulsed-laser deposition (PLD) and sputtering, this technique is uniquely capable of controlling the layering at one-unit-cell level in a clean vacuum environment with the absence of highly energetic species [27]. Thus MBE is the technique of choice for the deposition of complex heterostructures in a variety of crystal systems and allows the growth of many metastable compounds and structures that cannot be realized by bulk synthesis techniques. MBE was initially developed for the deposition of compound semiconductors of GaAs and GaAs/AlGaAs in the 1960s [60, 61] and its use has expanded to other semiconductors, metals, and insulators [62, 63]. In general, ion gauges, mass spectrometers, and reflection high energy electron diffraction (RHEED) are the common flux calibration tools utilized

in III-V MBE systems. Especially, RHEED is one of the widely used *in situ* analysis techniques in MBE systems [64]. It can reveal the evolution of thin film surface during MBE growth. The electron beam with energy of 10 to 100 keV is incident on the film surface at a grazing angle of a few degrees and is diffracted toward a phosphorous detector screen.

Oxide MBE, which is used for the growth of $Sr_{n+1}Ti_nO_{3n+1}$ (Chapter 5), $La_{n+1}Ni_nO_{3n+1}$ (Chapter 5), $SrTiO_3$ (Chapter 6), and $LaNiO_3$ (Chapter 7) thin films in this work, is the result of a recent development oxide MBE system with *in situ* synchrotron X-ray scattering capability. Different from conventional MBE systems, oxide MBE uses the oxidizing agents such as oxygen or oxygen/ozone mixture to oxidize thin films. The schematic of our newly

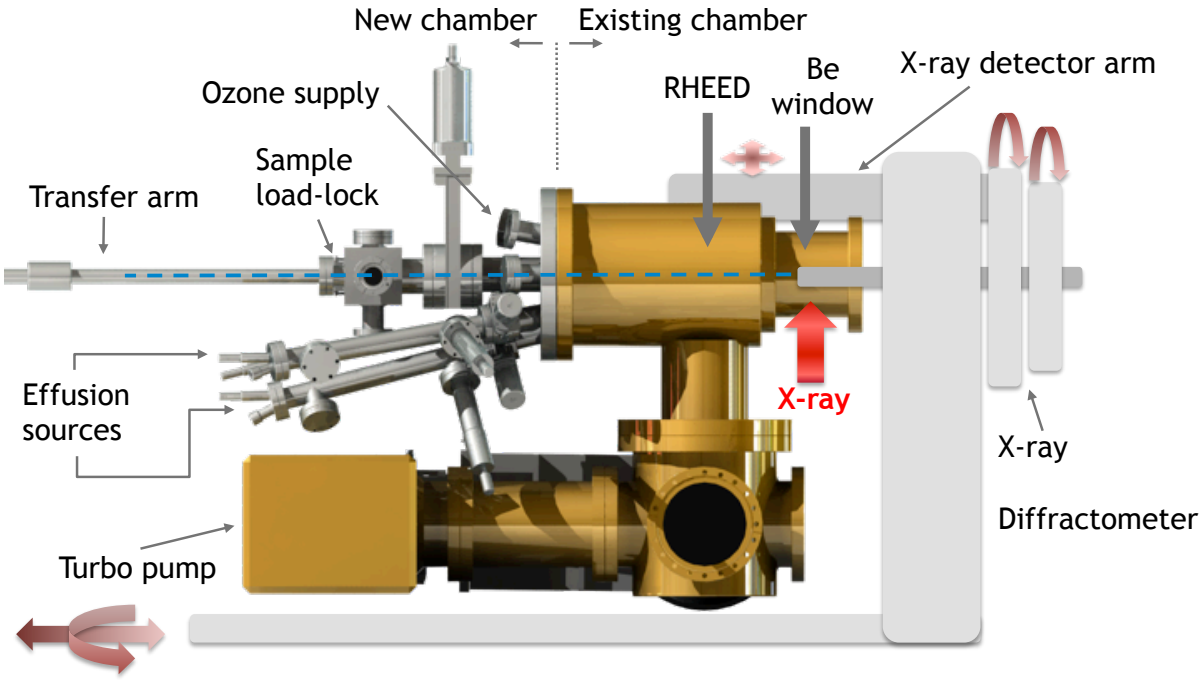

Figure 2.2. A schematic of the molecular-beam epitaxy system at beamline 33-ID-E of Advanced Photon Source.

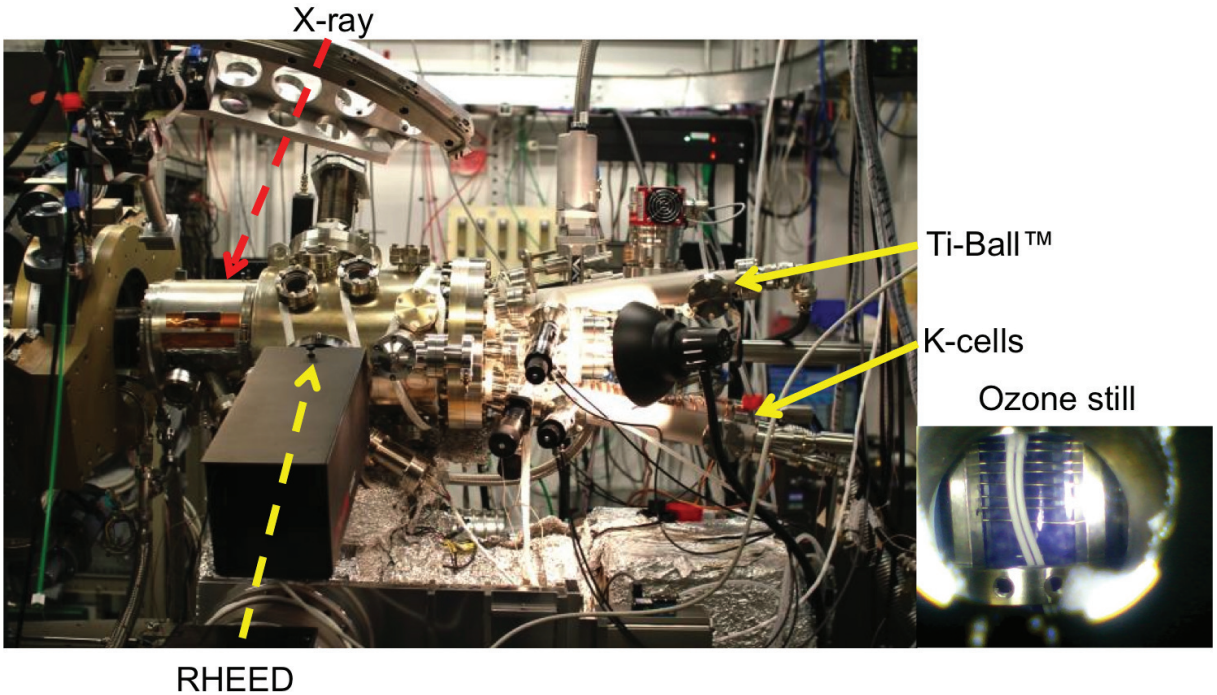

Figure 2.3. Photo of the *in situ* oxide growth chamber upgrade from the existing molecular beam epitaxy system in research station of beamline 33-ID-E at Advanced Photon Source with a snap shot of the ozone stiller.

constructed oxide MBE system, built from an existing *in situ* X-ray chamber at beamline 33-ID-E of Advanced Photon Source (APS) [65] is shown in Figure 2.2, and the photo in the research station of beamline 33-ID-E with a snap shot of the ozone still is shown in Figure 2.3.

An oxidant is supplied through through a leak valve and travels down a water-cooled electropolished stainless steel tube that is directed perpendicular and close to the substrate surface. The tolerable pressure of the oxidant is limited so as not to destroy the long mean free path necessary for MBE. The high temperature components such as heater filaments, crucibles, and substrate holders also must be made of materials that are resistant to the oxidant. Some oxides that are difficult to oxidize in oxygen require the use of more reactive

oxidant such as pure ozone or oxygen plasma sources [66]. Ozone, however, is highly toxic and flammable and therefore careful operation is necessary.

Among the many thin film growth techniques in MBE, codeposition and shuttered deposition are utilized in this work. In codeposition growth, all the component molecules are deposited on the substrate surface simultaneously by opening the source shutters at the same time. The flux of individual molecular beam is calibrated before deposition by a quartz crystal microbalance (QCM) to yield the desired film composition. The film thickness is controlled by the duration of shutter opening. In shuttered deposition, both sources were shuttered to deposit alternating monolayer doses of all the component molecules. This sequence repeats until the desired thickness is reached. This shuttered deposition technique is very similar to migration enhanced epitaxy of GaAs, proposed in the late 1980s [67]. In the shuttered growth technique only one shutter is actuated at a time and the total dose of an element deposited is the product of the time the shutter is open and the flux of the molecular beam. The relative doses of each element are adjusted, usually through the time the shutter is open, to deposit a single stoichiometric monolayer. For this work the shuttered deposition technique was used exclusively, the heated substrate is exposed to alternating monolayer doses of molecular beams from all components under a steady flux of oxygen or a mixture of oxygen and ozone ($\sim 10\%$ O_3).

CHAPTER 3

X-ray Characterization Methods

3.1. Surface X-ray Diffraction (SXRD)

In the study of structure of surfaces, scientists have typically used electron based techniques, such as low energy electron diffraction (LEED), in which an electron beam of 10–100 eV in energy is irradiated on a sample surface with nearly normal incidence to obtain backscattered diffraction patterns. Due to the strong interaction of electrons with matter, LEED is extremely surface sensitive but also resulting in multiple scattering. Thus LEED cannot be quantitatively analyzed with the kinematical approximation and requires dynamical theory for thorough analysis. In contrast, X-ray interacts much more weakly with matter, and the advent of high brightness synchrotron X-ray radiation sources has led to the creation of powerful X-ray based surface science techniques. The sensitivity of X-ray scattering techniques to interfacial structures arises from the interference of X-rays scattered from surfaces and interfaces, such as X-ray reflectivity, surface and thin-film X-ray diffraction, crystal truncation rods (CTR) [**68**, **69**, **70**].

The X-ray reflectivity can be generalized as $R \propto |F|^2$, where F is the structure factor, which in turn is the Fourier transform of the electron density distribution of the system. For an infinite 3D periodic structure, i.e., a single crystal, the Fourier transformation yields the discrete points, i.e., Bragg peaks, in the reciprocal space. If the real space structure, however, is not infinite along one of the dimensions, but has a surface, i.e., a surface

can be viewed as a defect of a crystal where the periodicity is stopped, or "truncated, in one direction, the Fourier transformation will give a continuous distribution of diffraction intensity. The distribution, in reciprocal space, is perpendicular to the surface, i.e. in the truncated direction of periodicity. Those are the so-called crystal truncation rods (CTRs). In analogy to the Bragg crystallography, in which the Bragg peak positions and intensities are determined by the bulk crystal structure and chemical composition, the intensity modulation of the truncation rods are directly related to the surface structure and species. Because the CTR intensities between Bragg peaks are orders of magnitudes weaker than those on the Bragg peaks, the method was not widely used until synchrotron X-ray sources became available. Perhaps the most comprehensive technique by far for solving surface structure is surface X-ray diffraction (SXRD) [**69**, **70**]. Moreover, SXRD is ideally suited to determine the atomic structure of the entire system across the film-substrate interface [**71**].

Here we briefly review the use of X-ray reflectivity to probe the structure of thin films as well as surfaces and interfaces. X-ray reflectivity, simply defined as the ratio of the reflected and incident X-ray fluxes, is typically measured over a broad range of incident angles. X-rays probe structures along the direction of momentum transfer, $\vec{q} = \vec{k}_{in} - \vec{k}_{out}$, where $|\vec{k}| = 2\pi/\lambda$ is the wave vector of the X-ray photon whose direction is along the photon propagation direction [Figure 3.1(c)]. In the simple case of the mirror-like reflection of X-rays from a surface or interface (i.e., specular reflectivity) the structure is probed only along the surface-normal direction[Figure 3.1(a)]. We are specifically interested in the case of high-resolution specular reflectivity, which probes the laterally averaged interfacial structure. These measurements typically are performed to < 1 Å spatial resolution by

measuring the structure factor well into the regime where the tails of the substrate Bragg peaks modulate the interfacial reflectivity, often referred to as CTR profiles [68]. The measurement and interpretation of X-ray reflectivity data (i.e., the angular variation of reflected X-ray intensities as a function of incident angle) [69, 72, 70] derive from the same theoretical foundation as X-ray crystallography, a technique used widely to study the structure of bulk (three-dimensional or 3D) materials [73, 74]. An important characteristic of X-ray reflectivity data is that these techniques are not only surface sensitive, but also specifically derived from the interfacial structure.

X-ray data for surfaces and bulk materials appear in different forms, as can be seen when scattered the intensity presented in reciprocal space. Surfaces and crystals appear as rods and points, respectively, as shown in Figure 3.1(b). For a rectangular surface unit mesh, each of the Bragg rods are indexed with integer surface Miller indices (H, K) and a continuous index, L, along the rod within this surface coordinate system.

The relationship between the interfacial structure and the reflected X-ray intensity has been discussed previously in detail, but for completeness it is summarized here. The sensitivity of X-ray diffraction to structure is derived from measurements of scattering intensities. As originally derived by Robinson [72], the integrated scattering intensity, I_{int}, due to a surface or interface is

$$I_{int} = I_0 \left(\frac{e^2}{mc^2}\right) \left[\frac{(A\lambda^3 P/a_{uc}^2)}{\Omega}\right] \frac{1}{\sin(2\theta)} |F|^2 \frac{\Delta q_z}{2\pi}, \tag{3.1}$$

where I_0 is the incident photon intensity (in units of photons per area per second), $r_e = e^2/mc^2$ is the classical electron radius, A is the active area of the surface (i.e., the area of the surface that participates in the diffraction measurement), λ is the X-ray wavelength,

P is a polarization factor, a_{uc}^2 is the area of the surface unit cell, Ω is the angular velocity in the rocking scan, $1/\sin(2\theta)$ is the Lorentz factor, 2θ is the scattering angle, F is the structure factor of the interface, and Δq_z is the length of the surface rod that is integrated in the rocking scan (e.g., due to the finite detector resolution). Therefore, I_{int}, has units of photons per second. Many of the pre-prefactors in Equation 3.1 depend on the details of the

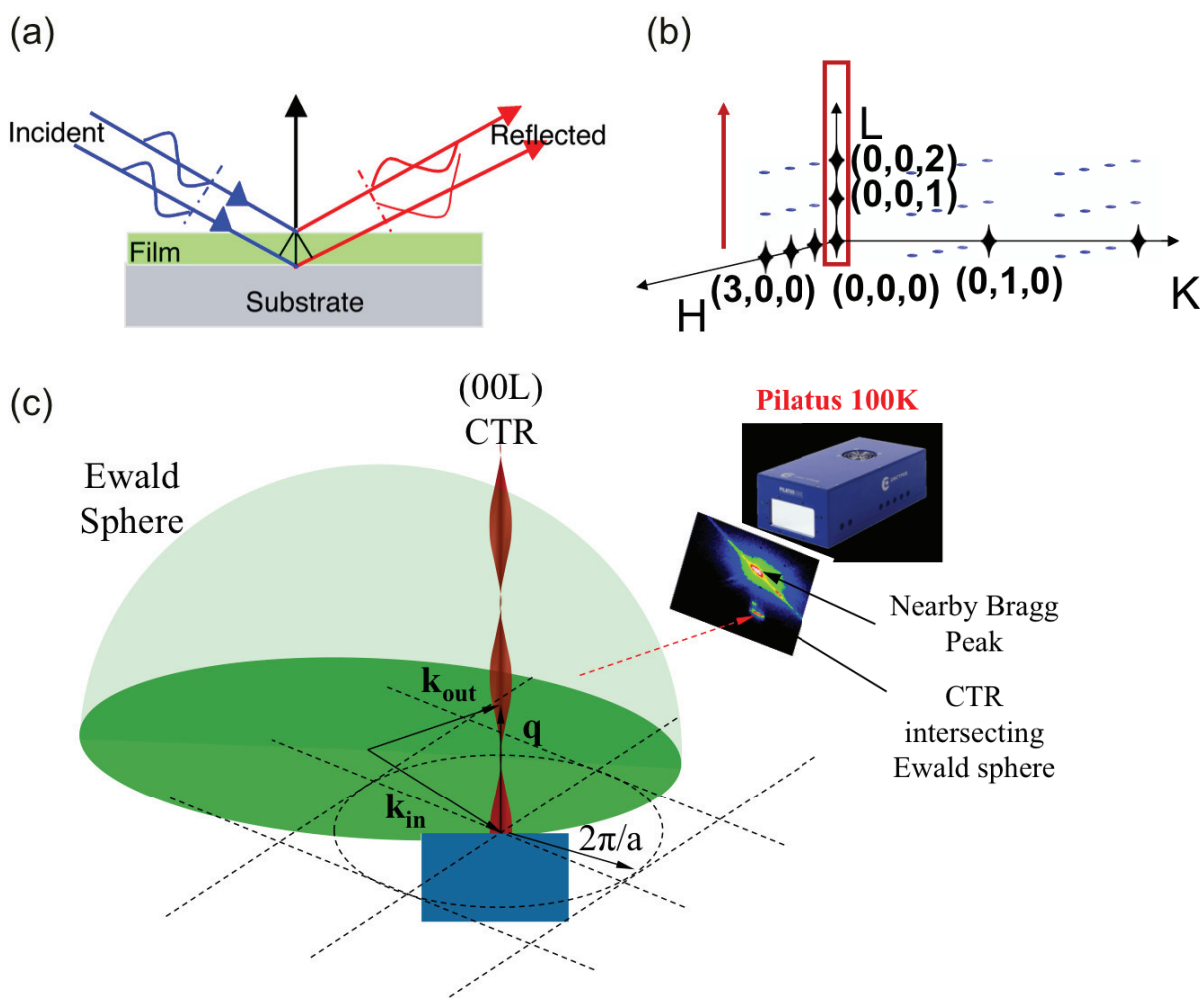

Figure 3.1. Principle and geometry of specular X-ray reflectivity measurement (a) in real space, and (c) in reciprocal space. (b) The reciprocal-space structure for a truncated crystal. Crystal truncation rods extend from Bragg peaks along the surface-normal direction.

scattering experiment and on the choice of diffractometer [75, 76, 77, 78, 79, 80, 81, 82]. Normalizing the scattering intensity to the incident beam flux yields the X-ray reflectivity, which is dimensionless.

The structure factor, F, is proportional to the Fourier transform of the electron density distribution and related to the geometric structure through the relation:

$$F(\mathbf{q}) = \int \rho(\mathbf{r}) e^{i\mathbf{q}\cdot\mathbf{r}} d\mathbf{r}, \tag{3.2}$$

where $\rho(\mathbf{r})$ is the electron density. Therefore, the structure factor for a collection of atoms can be expressed as

$$F(\mathbf{q}) = \sum_j f_j(\mathbf{q}) e^{i\mathbf{q}\cdot\mathbf{r}} e^{-(qu_j)^2/2}, \tag{3.3}$$

where f_j, $\mathbf{r}_j$, and u_j are the atomic scattering factor, position, and vibrational amplitude of atom j. This sum is over all atoms in the sample. The interfacial structure factor in Equation 3.3 can be rewritten in a form that allows for substantial conceptual simplification:

$$F = F_{uc} F_{CTR} + F_{surf} \tag{3.4}$$

Each of these terms is identical to the structure factor as described in Equation 3.3, except that the summation is over a subset of atoms. F_{uc} is summed only over atoms within a single bulk unit cell; F_{surf} is summed over all near-surface atoms that might be displaced from their ideal bulk lattice positions (typically 2–3 layers deep into the crystal) plus any adsorbed layers or films attached to the surface. The structure factor of a truncated crystal (known as a crystal truncation rod, or CTR [176]) which accounts for the semi-infinite

stacking of the surface layer to complete the substrate lattice is

$$F_{CTR} = \frac{1}{1 - exp(i\mathbf{q} \cdot \mathbf{c})}, \tag{3.5}$$

where $\mathbf{c}$ is the vector separation between neighboring substrate layers, with layer spacing c.

In the last few years, the typical method for measuring CTRs has transitioned from the use of point detectors to the use of area detectors. The use of area detectors enables the simultaneous sampling of both the rocking curve and background so that the background-subtracted reflectivity signal can be acquired with a single camera shot. This has led to greatly improved speed and accuracy of CTR data acquisition [83, 84, 85]. In addition, this methodology allows for the visualization of the scattered intensity, effectively enhancing the ability to identify spurious signals in the detector, and thereby improving overall data interpretation and signal integration.

As shown in Figure 3.1(c), in the condition in which the intersection of the Ewald sphere with the CTR is completely encompassed when intersected with the area detector (i.e., PILATUS 100K), the absolute specular reflectivity is derived in Ref. [86] and expressed as

$$R(q_z) = \left(\frac{4\pi r_e}{q_z a_{uc}}\right)^2 |F(q_z)|^2 |B(q_z)|^2, \tag{3.6}$$

where a_{uc}^2 is the surface unit cell area and $B(q_z)$ is the Robinson roughness factor [68],

$$|B(q_z)|^2 = \frac{(1-\beta)^2}{1 + \beta^2 - 2\beta\cos(q_z c)}, \quad 0 \leq \beta \leq 1 \tag{3.7}$$

Typically, the measured CTR data is compared to the theoretical calculations to test the validity of some modeled electron density profile. The model structure parameters, such as film lattice constant and thickness, atomic layer position, density, and interface roughness (Equation 3.6 and Equation 3.7) can all be tuned until agreement is reached between data and theory, and is traditionally done by using a least-squares minimization routine. While this approach is powerful, it suffers from several limitations, especially for complex systems which a large number of fitting parameters are necessary, such as, it is difficult to ensure that the optimization minima, the dependence of the final result of the starting model, parameter choices, and fitting procedures, all of which are subjective values chosen by the researcher, and the inability to explore the entire parameter space due to computational practicalities. To address this shortcoming, some have employed various iterative algorithms for phase retrieval from intensity data that should allow for the structure to be derived directly from CTR data, such as Fienup phase retrieval algorithms [**87**, **88**] or coherent Bragg rod analysis (COBRA) [**89**, **90**, **91**].

3.2. X-ray Absorption (XAS)

X-ray absorption spectroscopy (XAS) offers an advantage over visible-light spectroscopy because it is element-specific and has been used to obtain valuable information about the local density of the unoccupied states. In particular, polarized XAS provides information on composition through its elemental specificity, on the local bonding environments of the atoms through its chemical specificity via binding energy shifts, and structural sensitivity in absorption fine structure [92, 93].

In the X-ray absorption process, an incident photon with energy near the target element absorption edge creates a photoelectron from a core-level. The core-hole will be filled by an X-ray fluorescence or an Auger electron process which are two kinds of byproducts

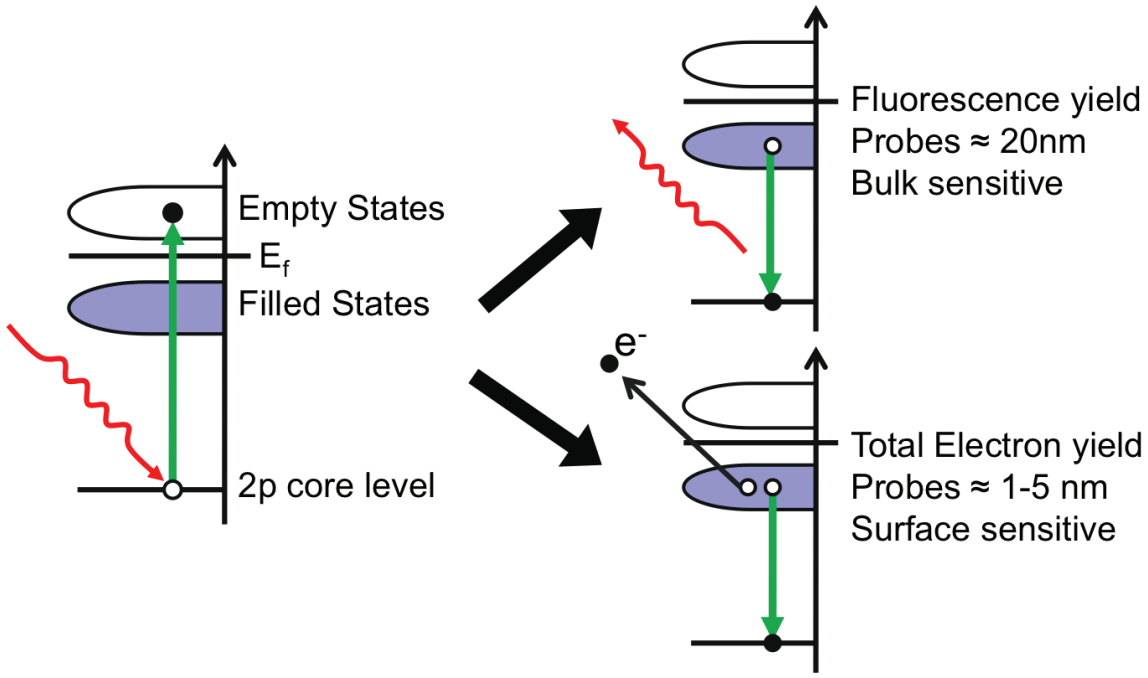

Figure 3.2. Schematic illustration of the X-ray absorption induced electronic transition, fluorescence yield (FY) and total electron yield (TEY). The transition corresponds to the L absorption edge.

generated by XAS process, and the intensities of them are proportional to the X-ray absorption. Therefore, we can get the information of the absorption process by measuring the byproducts of X-ray absorption. As a result, there are two ways to measure the X-ray absorption process, one is measuring X-ray fluorescence so called "fluorescence yield," and the other is measuring Auger electrons which is "total electron yield," as shown in Figure 3.2.

The X-ray absorption spectral shape is described with the Fermi Golden rule.

$$I_{XAS} \sim |\langle \Phi_f | \hat{e} \cdot r | \Phi_i \rangle^2 \delta_{E_f - E_i - \hbar\omega} \tag{3.8}$$

The intensity I_{XAS} is proportional to a dipole matrix element $(\hat{e} \cdot r)$ coupling the initial state (Φ_i) and the final state (Φ_f). The delta function (δ) takes care of the conservation of energy [93].

At the absorption thresholds of the elements, the spectrum shows strong resonances arising from transitions to unfilled valence states. In the case of $3d$ transition metals, the states are the unfilled $3d$ valence band as shown in Figure 3.2. Since the transitions are governed by the $\Delta l = \pm 1$ selection rule of primarily electronic dipole transitions, transition metals are best studied using $L_{2,3}$-edges ($2p \rightarrow 3d$ transitions) in the soft X-ray regime.

In addition, XAS is governed by Fermi's Golden Rule (Equation 3.8) so the absorption will be depend on the direction of the polarization of X-ray and the direction of the orbital and the transition intensity is directly proportional to the number of empty valence states in the direction of the electric field of X-ray. Thus the electric field $(\vec{E})$ of the linearly polarized X-ray acts like a searchlight for the direction of the maximum number of empty valence states of the atomic volume as illustrated in Figure 3.3. Therefore, polarization

dependent X-ray absorption measurements are able to provide detail information of different orbital symmetries. Linear polarized X-ray absorption can probe element-resolved orbital occupation and sense the charge anisotropy of the valence states involved in the core excitation process [94]. In most cases the anisotropy of the charge in the atomic volume is due to an anisotropy in the bonding although there can be a contribution from magnetism as well [95].

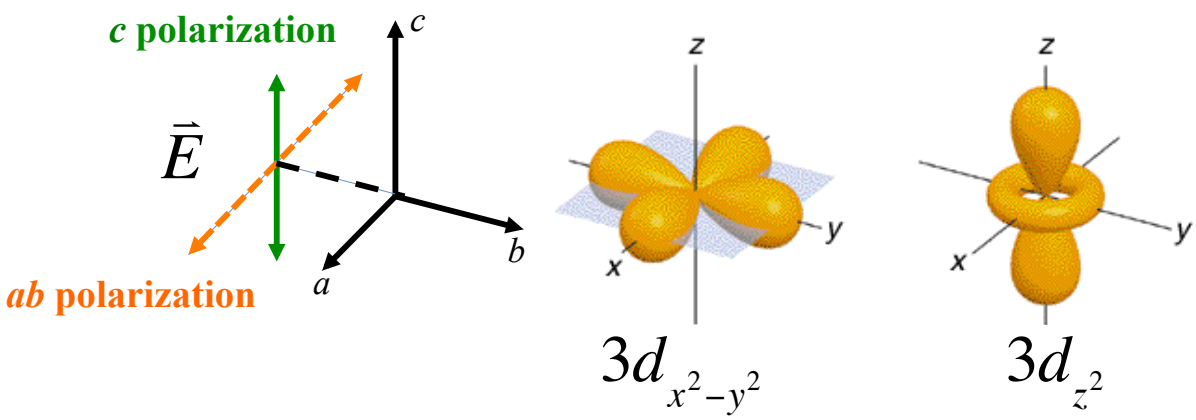

Figure 3.3. Schematic illustration of the vectorial-probe characteristic of X-ray Linear Dichroism (XLD). $\vec{E}$ represents the electric field direction of the linear polarized X-ray.

CHAPTER 4

Connecting Bulk Symmetry and Orbital Polarization in Strained $RNiO_3$ Ultra-Thin Films

Overview

We examine the structural and electronic properties of $LaNiO_3$ and $NdNiO_3$ *epitaxial thin films* grown on cubic (001) $SrTiO_3$ from the viewpoint of *bulk* crystal symmetry and misfit strain. X-ray scattering and polarization-dependent X-ray absorption spectroscopy measurements are performed to determine the crystal symmetry and extract the local Ni $3d$ orbital response, respectively, to understand the strain-induced distortions of the bulk structure. A strain-induced orbital polarization is found in $NdNiO_3$ films, but is absent in $LaNiO_3$ films. The difference in electronic structure is attributed to the bulk thermodynamic phases through group theoretical methods, which reveals that thin film perovskites retain a "memory" of their preferred electronic and structural configurations.

4.1. Introduction

Owing to the remarkable progress in achieving high-quality coherent perovskite oxide thin films and superlattices, heteroepitaxial synthesis has evolved into a reliable strategy to engineer orbital–lattice interactions in correlated oxide materials [12, 13]. In ultrathin film perovskite oxides, strain fields at the thin film-substrate interface directly tune the local electronic states of the correlated transition metal (TM) d orbitals, from which novel functionalities and phases prohibited in bulk phases are stabilized [14, 15, 16]. Rotationally distorted ABO_3 oxides, in particular, are susceptible to strain-induced changes in bond lengths and bond angles, which modify the crystal field symmetry and lead to differential orbital occupation (polarization). However, despite the recent progress, there is very limited experimental understanding of factors conducive to large orbital polarizations [17, 18, 19, 20, 21]. What governs the orbital–lattice response of the BO_6 units to the substrate-induced heteroepitaxial constraints? Isolating the principal interactions remains challenging: The orbital occupation can be significantly influenced by elastic strain (substrate–film lattice mismatch), octahedral rotation dissimilarities (crystallographic symmetry mismatch), and electrostatic (polarity) mismatch [22].

In this chapter, we experimentally demonstrate that the *bulk* crystal symmetry directs the atomic and orbital responses adopted by a coherently strained ultrathin film of perovskites. Using $RNiO_3$ perovskite nickelate thin films (R = rare-earth, i.e., La and Nd) on cubic $SrTiO_3$ (STO) substrates, in particular, we isolate the role of the parent crystal's symmetry on the orbital–lattice evolution. Detailed X-ray crystal truncation rod (CTR) measurements and X-ray linear dichroism (XLD) show that tensile strain generates a small orbital splitting consistent with out-of-plane lattice contraction for

nominally *orthorhombic* $NdNiO_3$ (NNO) films, while no experimentally observable orbital splitting is found in *monoclinic* $LaNiO_3$ (LNO) films, which also exhibit a comparable tetragonal lattice contraction. We trace the key feature to the symmetry unique NiO_6 octahedral distortions present in the bulk NNO and LNO phases, which produce distinct rotational patterns in thin films identified from a systematic survey of the half-order Bragg reflections. A quantitative group theoretical analysis of the epitaxial stabilized crystal structures computed from density functional theory (DFT) reveals that the preferred orbital configurations adopted by the thin films is the one that stays closest to the bulk, suggesting the strain-stabilized phases maintain a "memory" of their bulk state. Knowledge of the structural distortions present in the bulk thermodynamic phases emerges as a simple descriptor to guide materials selection for epitaxial thin films with designed large orbital polarizations.

We chose to study the correlated RNiO$_3$ system, which exhibits a bandwidth-controlled metal-insulator transition (MIT) [96] driven by changes in the Ni-O-Ni structure with pressure [97], different size R cations [98], and epitaxial strain [99, 100]. Rhombohedral $LaNiO_3$ (LNO) and orthorhombic $NdNiO_3$ (NNO) are selected because in bulk at room temperature (RT), both compounds are metallic (nominal Ni^{3+} valence) and are only distinguished by their different crystal structures: LNO exhibits out-of-phase NiO_6 octahedral rotations about the three-fold axis along the pseudocubic [111] direction ($a^-a^-a^-$ in Glazer notation, space group $R\bar{3}c$), and NNO is orthorhombic with one in-phase and two out-of-phase octahedral rotations ($a^-a^-c^+$, space group $Pbnm$), as illustrated in Figure 4.1 [101]. Ultrathin films of 10-15 unit cell (uc) thickness with a 2 uc $LaAlO_3$ (LAO) buffer layer [102] were synthesized on TiO_2-terminated (001)-oriented STO substrates by

pulsed laser deposition (PLD) with *in-situ* monitoring by reflection high energy electron diffraction (RHEED). The fixed sign of the lattice mismatch due to the STO substrate – both LNO and NNO are subjected to a tensile strain of 1.8% and 2.6%, respectively – allows us to isolate the contribution of the bulk symmetry difference (rhombohedral versus orthorhombic *vis á vis* the three or two out-of-phase rotations) on the orbitally polarized ground states.

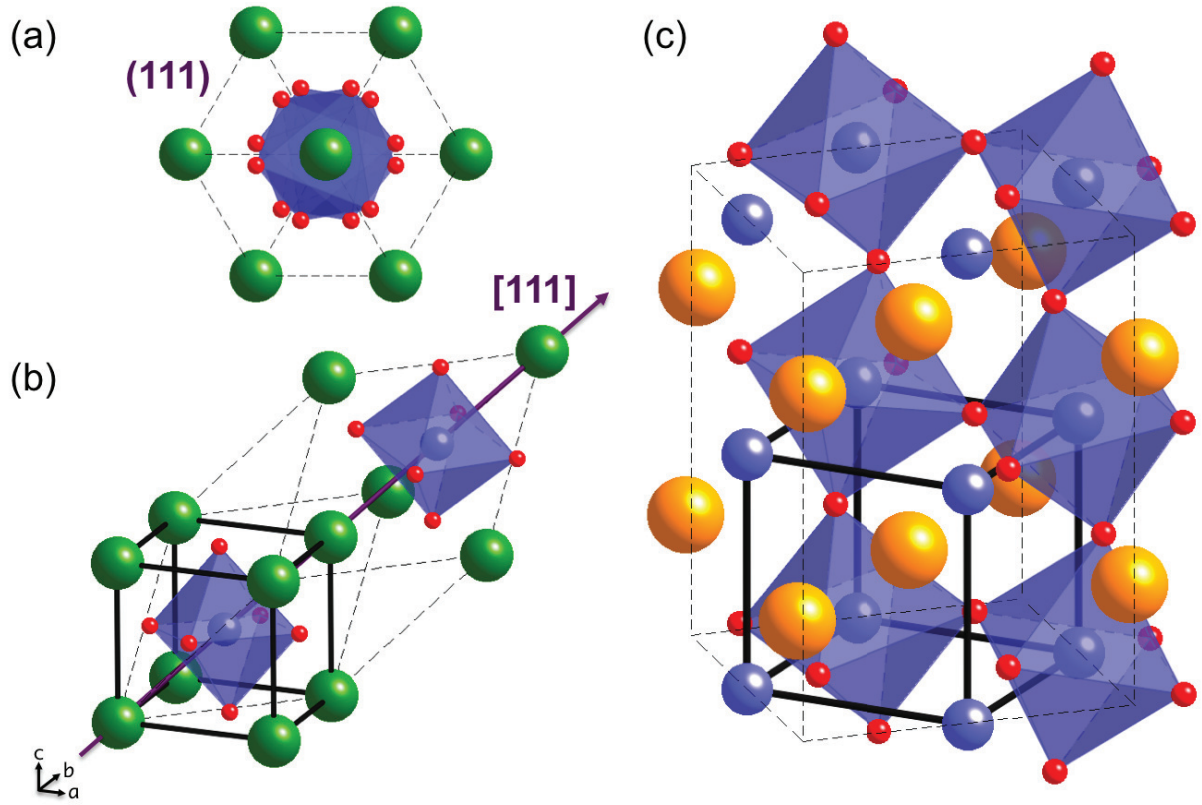

Figure 4.1. Schematic of the bulk $LaNiO_3$ (a)(b) and $NdNiO_3$ (c) structures showing both rhombohedral ($R\bar{3}c$) unit cell (dashed line) and orthorhombic ($Pbmn$) unit cell (dashed line) and the relationship to the pseudocubic unit cell (solid line). Part of the oxygen atoms and octahedra are not shown in (c) for clarity. La atoms shown in green; Nd atoms shown in orange; Ni atoms shown in blue at center of oxygen (red) octahedra. © 2013 American Physical Society.

4.2. Experiments

Coherent epitaxy, confirmed by reciprocal space mapping, and proper composition of the thin films is maintained during the layer-by-layer growth with the interrupted deposition approach [103] on single crystal STO substrates with TiO_2-terminated (001) surfaces prepared by a chemical wet-etch procedure [104]. The growth temperature was set in the range of 730-780 °C for LNO and 670-730 °C for NNO, while the oxygen partial pressure is maintained at 75-120 mTorr. After deposition, the samples are post-annealed *in-situ* for 30 minutes and cooled down to room temperature in one atmosphere of ultrapure oxygen to maintain the proper oxygen content [99]. The film structures were studied by X-ray scattering experiments in air at room temperature with standard four-circle diffractometers performed at beamlines 5-BM-D and 33-BM-C of the Advanced Photon Source (APS) at Argonne National Laboratory. The electronic and orbital properties of the samples were obtained with polarized soft X-ray absorption (beamline 4-ID-C of the APS) acquired in the bulk sensitive fluorescence yield (FY) mode with a NiO (Ni^{2+}) standard measured simultaneously in the diagnostic section of beamline 4-ID-C for spectral alignment [105].

4.3. Results and Discussions

4.3.1. Structure Analysis

Figure 4.2 shows the specular X-ray reflectivity data (dots) with error bar along the (00L) crystal truncation rod (CTR) for the NNO/LAO/STO (001) and LNO/LAO/STO (001) heterolayer structures. A ridge scan was used to acquire the specular scattering profile in the vicinity of the STO (002) peak as a function of out-of-plane scattering vector

Q_z. The background was subtracted from the reflectivity data by measuring rocking curves at several points along the scan [86], and a simulated curve (black line) was generated using a layered structural model. The $H = K$ reciprocal space maps (RSM) around the off-specular (113) Bragg peaks for the film and the substrate confirms both nickelate films are tetragonally strained and coherently lattice matched in-plane to the STO substrate [inset,

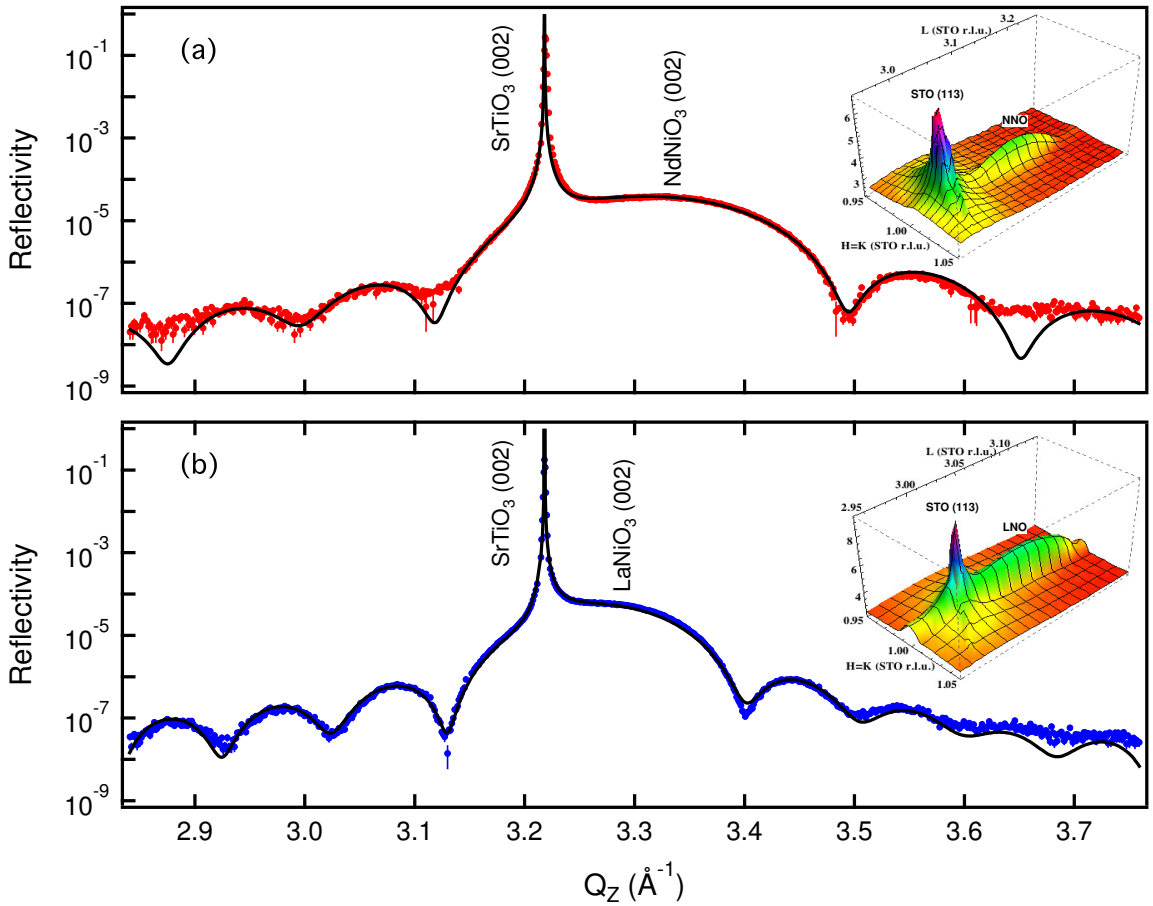

Figure 4.2. X-ray reflectivity data (dots) and fit (solid line) for scattering along the (00L) specular CTR through the $Q_z = 3.217$ Å^{-1} (002) Bragg peaks of the $SrTiO_3$ substrate and (a) $LaNiO_3$ and (b) $NdNiO_3$ film. Reciprocal space map around the (113) Bragg reflection showing the films are coherent with the STO substrate (inset). © 2013 American Physical Society.

Figure 4.2(a) and (b)]. In addition, we found no evidence of lateral strain modulations, which has been observed in other oxide films and was related to strain accommodation [**106**, **107**].

Least-squares fitting was performed where the film structure parameters were allowed to vary while fitting various models to the data, but the bulk STO structure was fixed. All films were fit with 5 free parameters (out-of-plane lattice constant of the LAO buffer layer and the film, c_1 and c_2, film offsets at each interface relative to the substrate u.c. origin, δ_1 and δ_2 (see Figure 4.3), and film thickness in u.c., N. The data points near the sharp STO (002) Bragg peak were omitted from fitting because the analysis only considers scattering in the kinematical approximation, and the data in this region do not contain information about the film structure itself. From the model-based analysis of the specular X-ray reflectivity, we experimentally determined that the unit cell thickness is N = 12 and 15 for NNO and LNO, and the out-of-plane lattice constants of NNO and LNO films are 3.760 ± 0.005 Å [**100**] and 3.815 ± 0.005 Å [**108**], respectively. The out-of-plane lattice constants of the LAO buffer layer and the interface film offsets are 3.840 ± 0.02 Å with $\delta_1 = 0.088$ Å, $\delta_2 = 0.168$ Å and 3.830 ± 0.04 Å with $\delta_1 = 0.098$ Å, $\delta_2 = 0.126$ Å for NNO and LNO hetrerostructures. The ranges of the upper and lower limit of the uncertainties of out-of-plane lattice parameters are determined from the $\Delta\chi^2 \sim 3$ contours [**109**] in the parameter space (90% confidence limits [**110**]). The results for NNO are consistent with an out-of-plane contraction, which is expected for a volume conserving scenario. Surprisingly, despite the fact that the LNO film was coherently strained by 1.8% tensile strain, the out-of-plane lattice constant is only 0.6% smaller than the bulk value. This anomalous lack of out-of-plane contraction is suggestive of a new structural

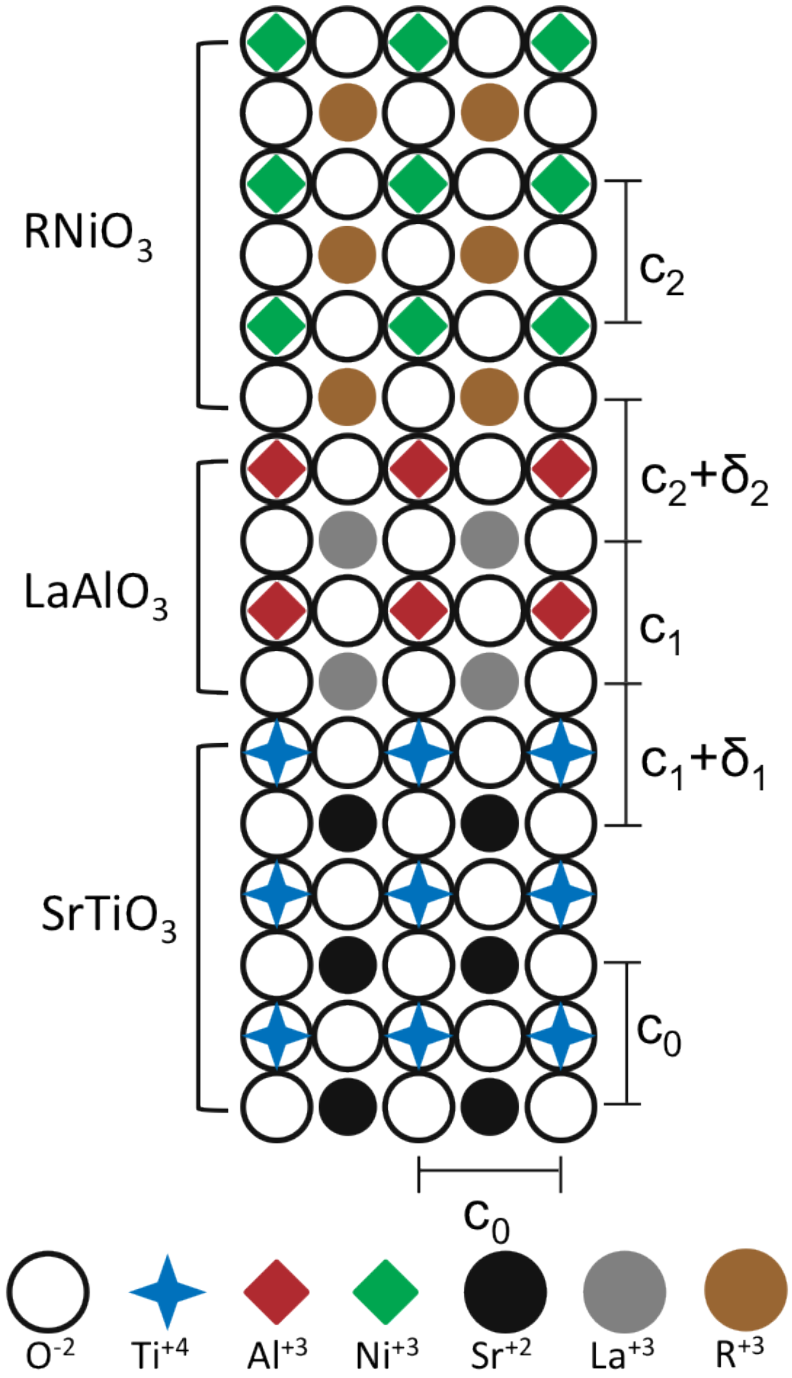

Figure 4.3. Schematic of $RNiO_3$ (R=rare earth) film, $LaAlO_3$ buffer layer and $SrTiO_3$ substrate with TiO_2terminated top layer heteroepitaxial layer structure. The in-plane lattice constant, a, out-of-plane lattice constants, c_0, c_1, and c_2, and interface film offsets, δ_1 and δ_2, are shown.

phase with larger unit cell volume, which was reported previously [18, 111]. Moreover it requires that the biaxial tensile strain is accommodated by both octahedral distortion and rotations perpendicular to the substrate or about an axis parallel to the substrate plane simultaneously or alternatively [13].

To address why such a distinct lattice response exists between LNO and NNO, a systematic survey of the half-order Bragg peaks for both films was conducted to determine the octahedral rotations, distortions, and underlying crystal symmetry. Since the octahedral rotations effectively double the pseudocubic unit cell, extra Bragg reflections unique to each tilt system are expected at a distinctive set of half-order reciprocal-lattice points [112]. Consequently, we can identify the rotation pattern of the $RNiO_3$ films by observing the presence and absence of specific half-order Bragg peaks [113].

As anticipated, we find half-order peaks for both LNO and NNO films (Figure 4.4), which confirms that heteroepitaxial growth on a cubic substrate does not suppress octahedral rotations even though they are likely modified in the first few unit cells of the film [114, 115]. To identify the octahedral tilt pattern, we search for signature half-order peaks that arise from rotations along the three principle axes [Figure 4.4(a)]. First, we examine in-plane rotations using the $(1/2, 1/2, 3/2)$ reflection [Figure 4.4(b)]. This peak implies that the in-plane unit cell is doubled from out-of-phase rotations for both LNO and NNO. To probe the out-of-plane rotations, we use peaks with integer L to determine the lack or presence of in-phase rotations along the film normal (z) direction. Figure 4.4(c) shows the presence of a $(3/2, 1/2, 1)$ Bragg peak for NNO but not for LNO, indicating the NNO film adopts the $a^-a^-c^+$ tilt pattern. To isolate the tilt pattern of LNO, we examine the $(3/2, 1/2, 1/2)$ reflection [Figure 4.4(d)], which contains information about rotations both in-

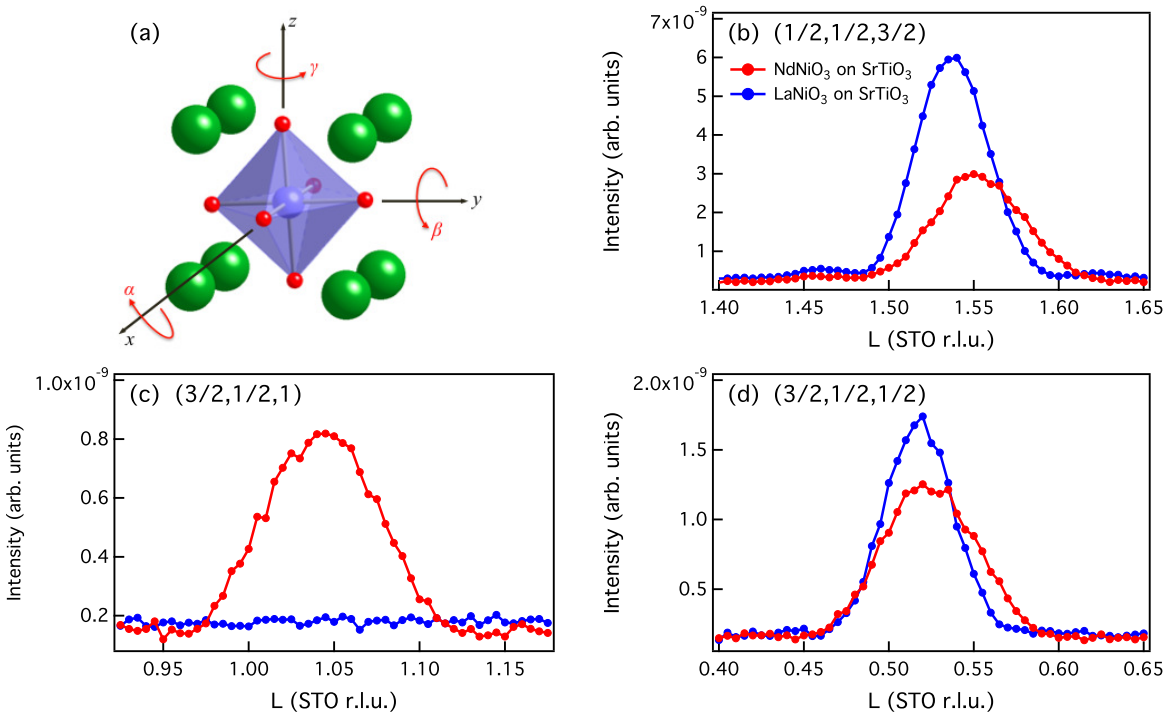

Figure 4.4. Half-order Bragg reflections through L at various H and K points. (a) A schematic illustration of the octahedral rotation axes (b) $H = K = 1/2$ (c)(d) $H = 3/2$ and $K = 1/2$. © 2013 American Physical Society.

and out-of-plane. The lack of integer L peak for LNO and reduction of the $(3/2, 1/2, 1/2)$ peak height [Figure 4.4(d)] with respect to the $(1/2, 1/2, 3/2)$ peak [Figure 4.4(b)] is consistent with an $a^-a^-c^-$ tilt pattern, where the out-of-plane tilts are reduced by the epitaxial strain [**111**, **116**]. From these tilt patterns, we conclude that LNO film has a lower monoclinic symmetry (space group $C2/c$) compared to the bulk LNO (rhombohedral, space group $R\bar{3}c$), consistent with earlier reports [**113**]. On the other hand, the NNO films remain in the same orthorhombic symmetry ($Pbnm$) as found in bulk at RT.

4.3.2. Electronic and Orbital Properties

To explore the link between structure and the local Ni orbital configuration, X-ray absorption spectra (XAS) of metallic NNO and LNO films on STO substrates were measured at the Ni L-edge with linearly polarized X-ray to measure X-ray linear dichroism (XLD), i.e., the difference between out-of-plane and in-plane polarization absorption. With a grazing incidence angle of 15° and by setting the linear polarization from the undulator to be either parallel or perpendicular to the film plane, we use XLD to probe the local occupied $3d$ orbital symmetry and the delocalized states imposed from the coordinating oxygen ligands. From the polarization-averaged XAS (average of out-of-plane and in-plane polarization absorption), shown in Figure 4.5, we quantitatively determine that the

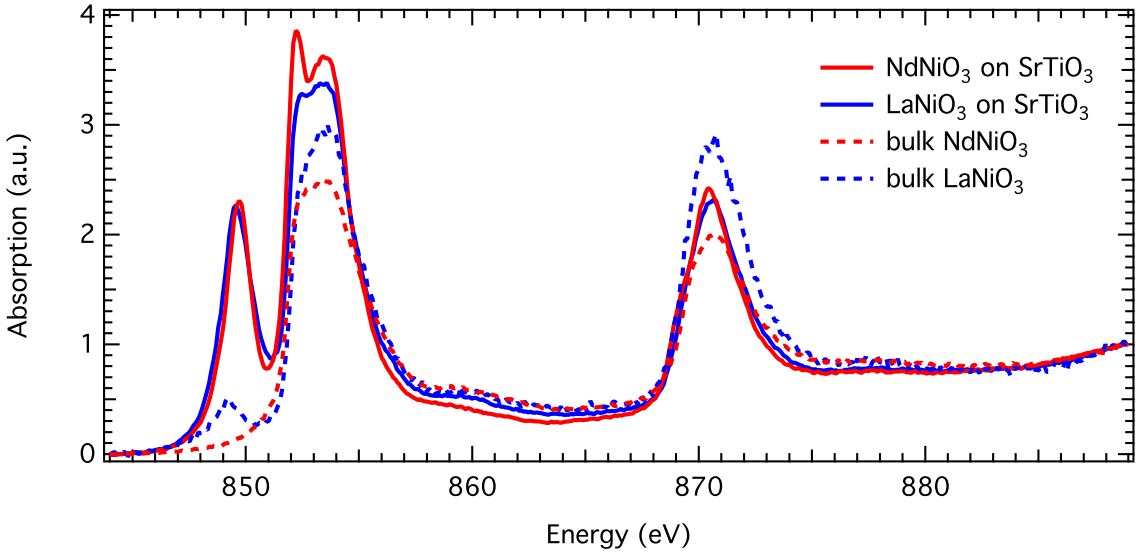

Figure 4.5. Polarization averaged XAS (average of out-of-plane and in-plane polarization absorption) measured in fluorescence yield (FY) mode at Ni L-edge. © 2013 American Physical Society.

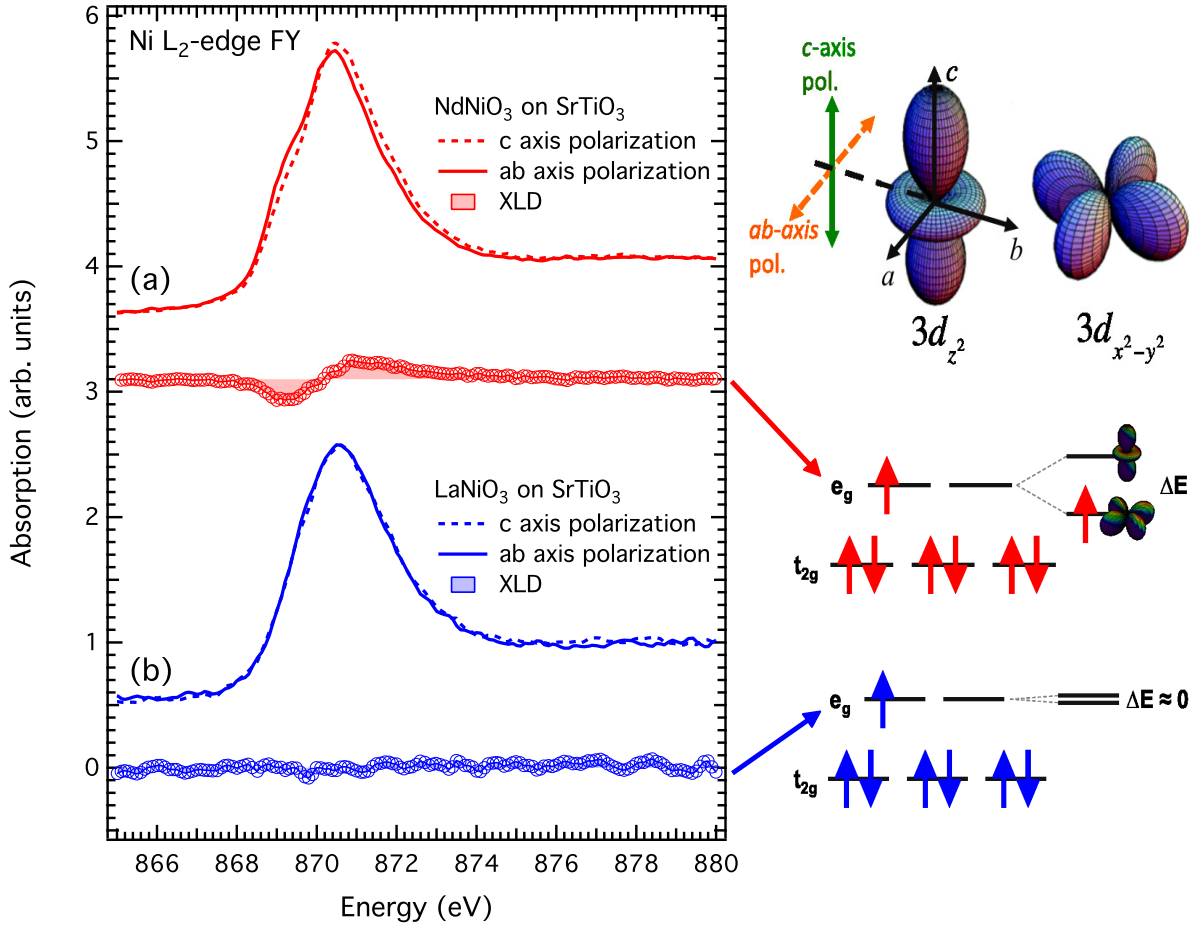

Figure 4.6.]
Polarization dependent X-ray absorption and X-ray linear dichroism (XLD) at the Ni L_2-edge for (a) $NdNiO_3$ and (b) $LaNiO_3$ on $SrTiO_3$. On the right, schematic orbital level diagram of $NdNiO_3$ on $SrTiO_3$ with the anticipated strain-induced orbital polarization effect on the e_g doublet and $LaNiO_3$ on $SrTiO_3$ without splitting of e_g orbitals. [Due to the overlap of M_4-edge of La (853 eV) with the Ni L_3-edge (852.7 eV), the spectra of films at the Ni L_3-edge is strongly distorted. Thus, the XLD was focused on the Ni L_2-edge (870 eV) where the line shape is free from distortions.] © 2013 American Physical Society.

valence of Ni is identical to bulk-like octahedrally coordinated Ni^{3+} testifying to the proper stoichiometry [117].

First, consider the XAS of the NNO film [Figure 4.6(a)]. The c-axis contraction shown by X-ray reflectivity ($c/a = 0.96$) clearly leads to a distortion of the octahedra as seen by an increase of the c-axis d-orbital ($3d_{z^2}$) energy. The absorption for polarization perpendicular to the ab-plane is shifted ∼0.2 eV higher in energy than the in-plane polarization absorption [Figure 4.6(a)]. The sign of the dichroism indicates a conduction band splitting, ΔE, between the e_g orbitals of Ni consistent with anisotropic Ni-O bonding, and it is in agreement with the strain-induced orbital polarization concept [**17**, **118**]. On the other hand, we would anticipate that the same orbital-lattice coupling should lead to an identical orbital polarization for LNO as in the case of NNO. However, our polarized XAS of the LNO film as shown in Figure 4.6(b) shows no observable orbital polarization. The absence of linear dichroism indicates no splitting of e_g orbitals as expected for undistorted octahedra in bulk crystal. The observed electronic structure suggests the presence of *uniform* Ni-O bond lengths despite the 1.8% tensile strain [**18**, **113**], and a c-axis lattice parameter with a small contraction in the out-of-plane direction. The data shown here is for bulk sensitive FY, but the surface sensitive total electron yield (TEY) displays the same response. This indicates that the bulk of the film and the surface have a similar orbital configuration. This is consistent with the fact that the tilts should be representative of the entire film. While the tilt pattern might be modified within ∼2-3 uc of the STO interface [**22**], the average of the entire film is the dominant signal.

4.3.3. Atomic Structure–Electronic Function Analysis

To reconcile this discrepancy, we emphasize that the presence or absence of linear dichroism should be directly attributed to the flavor of structural distortions in NNO and

LNO films, which originate from intrinsic ferroelastic tendencies of the bulk phases. To establish this relationship, we adapt an approach based on distortion modes [119, 120] which provides a description of the distorted strained structures in terms of irreducible representations (irreps), i.e., static structural displacements, of the ideal cubic perovskite phase. For an ideal cubic structure, each irrep within this basis has zero amplitude. However, the irreps compatible with the symmetry breaking from cubic ($Pm\bar{3}m$) to $C2/c$ and $Pbnm$ acquire finite amplitudes.

In the RNiO$_3$ perovskites, three symmetry-unique irreps describe the common octahedral distortions: (i) NiO$_6$ octahedral rotations (R_4^+ and M_3^+), (ii) Jahn-Teller distortions (R_3^+ and M_2^+), which lift the e_g degeneracy leading to orbital polarization, and (iii) NiO$_6$ breathing distortions (R_1^+), which causes the octahedra to dilate or contract according to the magnitude of charge δ transferred between Ni sites [121]. We hypothesize that the XLD seen in NNO films [Figure 4.6(a)] requires the presence of local Jahn-Teller distortions to the NiO$_6$ octahedra. To confirm this relationship between crystal symmetry and orbital polarization, Dr. Prasanna Balachandran and Prof. James M. Rondinelli used the `ISODISTORT` package [119] to decompose the LNO and NNO films' crystal structure obtained from density functional calculations and make a comparison to their bulk equilibrium phases in terms of these irreps.

4.3.3.1. Groundstate NdNiO$_3$ Structures

The ground state structure for NNO on STO substrates was determined from density functional calculations within the spin-polarized generalized gradient approximation (GGA) PBEsol exchange-correlation functional [122] plus Hubbard-U method as implemented in

Table 4.1. Theoretical crystallographic data for bulk $LaNiO_3$ on $SrTiO_3$. The space group is $P2_1/c$, with $a = b = 5.515$ Å, $c = 9.439$ Å, and $\gamma = 125.8°$. © 2013 American Physical Society.

Atom	x	y	z
La	0.255	0.473	0.25
Ni1	0.5	0	0.5
Ni2	0	0	0
O1	0.183	0.01	0.245
O2	0.254	0.731	0.0339
O3	0.302	0.221	0.0334

Table 4.2. Theoretical crystallographic data for bulk $LaNiO_3$ on $SrTiO_3$. The space group is $C2/c$, with $a = 9.406$ Å, $b = c = 5.523$ Å, and $\gamma = 125.95°$. © 2013 American Physical Society.

Atom	x	y	z
La	0	0	0.25
Ni	0	0	0
O	0.5456	0	0.25

the *Vienna Ab initio Simulation Package* (VASP) [**123**, **124**, **125**, **126**]. In our simulations, we do not explicitly include the substrate but rather impose the mechanical constraint that the in-plane lattice parameters are fixed to those of the experimental lattice constant of STO and the out-of-plane lattice constant is given by our experimental measurements. We then optimize the internal degrees of freedom. The Dudarev approach [**124**] was followed to include an effective Hubbard term $U_{\text{eff}} = U\text{-}J$ of 4 eV and accurately treat the correlated Ni $3d$ orbitals. The core and valence electrons were treated with the projector-augmented wave method [**127**] and the Brillouin-zone integrations were performed with a Gaussian smearing of 0.05 eV over a $7 \times 7 \times 7$ Monkhorst-Pack k-point mesh [**128**] centered at Γ, and a 500 eV plane-wave cut-off. In all calculations, ferromagnetic spin order was imposed.

We surveyed four NNO crystal structures belonging to space groups $P\bar{1}$, $P2_1/m$, $P2_1/c$, and $Pnma$ informed by symmetry-breaking selection rules and calculated the

Table 4.3. Theoretical crystallographic data for bulk $NdNiO_3$ on $SrTiO_3$. The space group is $P2_1/c$, with $a = b = 5.5225$ Å, $c = 9.30913$ Å, and $\beta = 53.67408°$. © 2013 American Physical Society.

Atom	x	y	z
Nd	-0.25798	0.04783	0.24991
Ni1	0	0	0.5
Ni2	0.5	0	0
O1	-0.17115	0.48182	0.25477
O2	-0.33629	0.28027	0.04319
O3	0.26387	0.20784	-0.04232

equilibrium geometry to determine the ground state structure for NNO on STO substrate. In symmetries $P\bar{1}$ and $P2_1/m$ the long axis about which the in-phase rotations of octahedra occur is oriented parallel (∥) to the epitaxial plane, whereas in $P2_1/c$ and $Pnma$ the long axis is perpendicular (⊥) to the epitaxial plane. The crystal structure data for all relaxed configurations can be found in Ref. [121], and shown in Table 4.1 [18], Table 4.2 [113] for theoretical crystallographic data of $LaNiO_3$ on $SrTiO_3$ and Table 4.3, Table 4.4 for theoretical crystallographic data of $NdNiO_3$ on $SrTiO_3$ (this work). The published crystal structure data used for mode-decomposition analysis of bulk $LaNiO_3$ [101] and $NdNiO_3$ [129] have also been shown in Table 4.5 and Table 4.6, respectively. For NNO we find that the lowest energy structure belongs to monoclinic $P2_1/c$ symmetry (Table 4.7), thereby favoring in-phase octahedral rotations that occur about an axis perpendicular to the epitaxial plane concommitant with breathing distortions of the NiO_6 units. The next lowest energy structure exhibits essentially the same octahedral tilt pattern, but lacks the later breathing distortion.

Table 4.4. Theoretical crystallographic data for bulk $NdNiO_3$ on $SrTiO_3$. The space group is *Pnma*, with $a = c = 5.5225$ Å, $b = 7.5$ Å. © 2013 American Physical Society.

Atom	x	y	z
Nd	-0.04758	0.25	-0.49145
Ni	0	0	0
O1	-0.48271	0.25	0.41738
O2	0.28668	-0.45785	0.21518

Table 4.5. Experimental crystallographic data for bulk $LaNiO_3$. The space group is $R\bar{3}c$, with $a = b = 5.4573$ Å, $c = 13.1462$ Å, and $\gamma = 120°$. © 2013 American Physical Society.

Atom	x	y	z
La	0	0	0.25
Ni	0	0	0
O	0.5456	0	0.25

Table 4.6. Experimental crystallographic data for bulk $NdNiO_3$. The space group is *Pbnm*, with $a = 5.3888$ Å, $b = 5.3845$ Å, $c = 7.6127$ Å. © 2013 American Physical Society.

Atom	x	y	z
Nd	0.9935	0.0359	0.25
Ni	0.5	0	0
O1	0.0743	0.4930	0.25
O2	0.714	0.2879	0.0332

Table 4.7. Energy difference (ΔE) obtained from DFT calculations of NNO on STO substrates for in-phase octahedral rotations either parallel ($\|$) or perpendicular ($\perp$) to the plane of epitaxial strain. ΔE is given in meV per formula unit (meV/f.u.) © 2013 American Physical Society.

Space group	Orientation	ΔE (meV/f.u.)
$P\bar{1}$	$\|$	11.315
$P2_1/m$	$\|$	17.55
$P2_1/c$	$\perp$	**0**
Pnma	$\perp$	7.86

Table 4.8. Mode-decomposition analysis results as obtained from `ISODISTORT` group theoretical tool. Amplitudes of symmetry-adapted irreps are given in Å units. *Abbreviations*: Sp. gr. stands for space group. © 2013 American Physical Society.

Type	Sp. gr.	R_1^+	R_3^+	R_4^+	R_5^+	X_5^+	M_2^+	M_3^+	M_5^+
$LaNiO_3$									
Bulk	$R\bar{3}c$	–	–	0.4371	–	–	–	–	–
on $SrTiO_3$	$P2_1/c$	0.07004	0.00205	0.50111	0.03443	0.15781	0.00137	0.26445	0.00274
on $SrTiO_3$	$C2/c$	–	–	0.49954	0.03485	–	–	–	–
$NdNiO_3$									
Bulk	$Pbnm$	–	–	0.535	0.046	0.197	0.01	0.4	–
on $SrTiO_3$	$Pnma$	–	–	0.64307	0.04703	0.27582	0.01013	0.38956	–
on $SrTiO_3$	$P2_1/c$	0.08026	0.01174	0.65159	0.0452	0.27878	0.00239	0.39223	–

4.3.3.2. Symmetry-adapted Mode Decompositions

Mode-decomposition analysis results as obtained from ISODISTORT group theoretical tool are shown in Table 4.8. The LNO films on STO with $C2/c$ monoclinic structure are decomposed into R_4^+ and R_5^+ [Figure 4.7(a)] irreps associated with the out-of-phase octahedral rotations and out-of-phase bending mode, respectively (A schematic representation of symmetry-adapted distortion modes can be found in Table 4.9). In bulk LNO, however, the rhombohedral $R\bar{3}c$ symmetry [101] prohibits the R_5^+ and consists of only the R_4^+ mode. This analysis also finds a key structural feature missing: Despite the tetragonal strain on the crystal lattice, we do not find any NiO_6 Jahn-Teller mode in the LNO films, which supports the observed absence of dichroism in our polarized XAS measurements [Figure 4.6(c)]. Note that although earlier work [18] showed that LNO films under tensile strain on STO at low temperature show a semiconducting gap of 0.10 eV (space group $P2_1/c$), stabilized by an emergent strain-induced octahedral breathing

distortion not found in the bulk, the relatively small amplitudes of the Jahn-Teller irreps, M_2^+ and R_3^+ [Figure 4.7(inset)], should also lead to no appreciable dichroism.

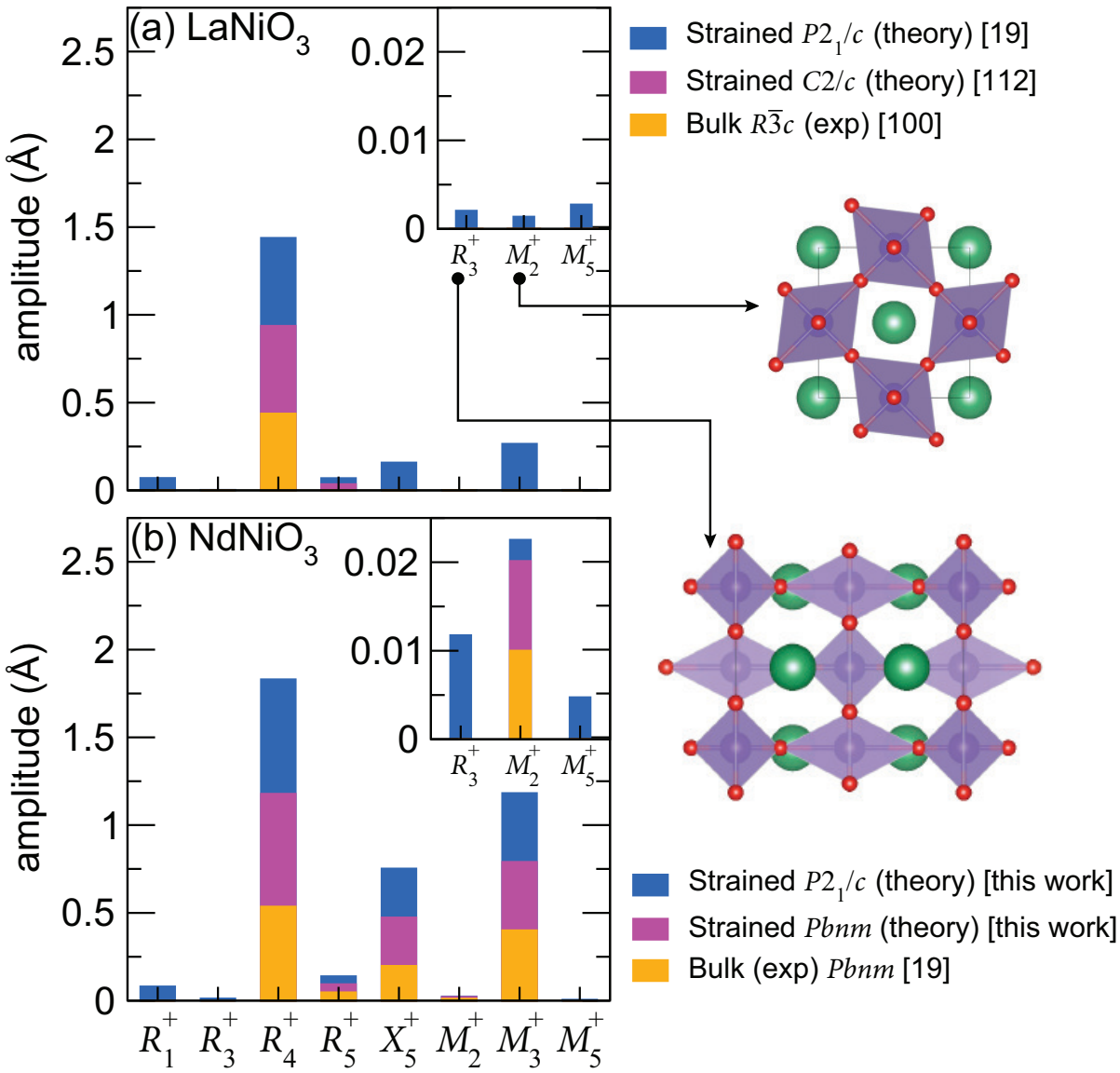

Figure 4.7. Distortion-mode analysis of (a) LNO and (b) NNO structures in both thin film and bulk phases with bond elongation modes producing orbital polarizations shown schematically to the right. © 2013 American Physical Society.

Table 4.9. Irreps and associated octahedral distortions. © 2013 American Physical Society.

Irreps	**Octahedral distortions (amplitudes exaggerated for clarity)**	**Description**
Undistorted	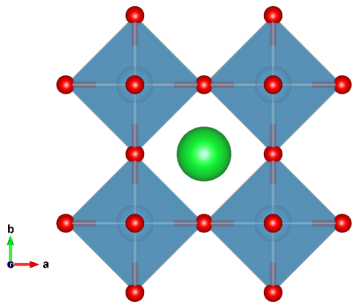	Ideal octahedra no distortion
M_2^+	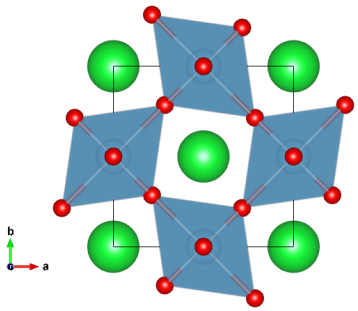	Type-d Jahn-Teller distortion
M_3^+	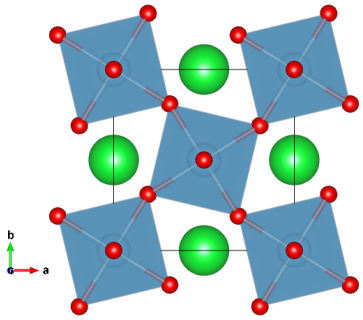	In-phase octahedral rotation
M_5^+	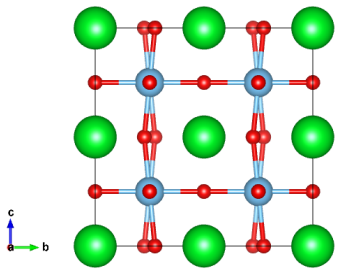	Out-of-phase octahedral tilting

R_1^+	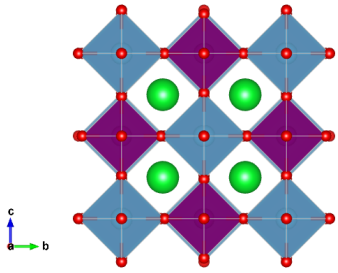	Breathing distortion
R_3^+	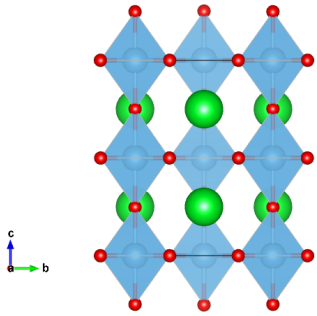	Type-a Jahn-Teller distortion
R_4^+	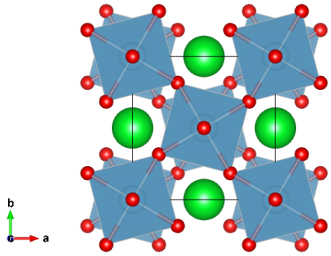	Out-of-phase octahedral rotation
R_5^+	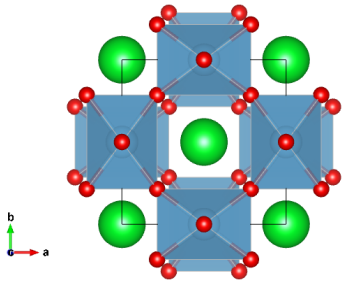	Out-of-phase octahedral buckling/bending mode
X_5^+	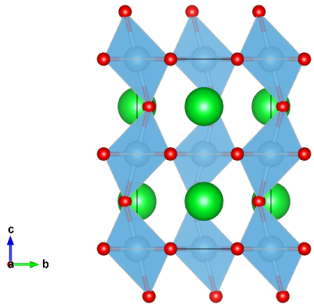	In-phase tilting + A-site cation displacement

In the case of NNO on STO thin films, our experimental results suggest the same orthorhombic *Pbnm* symmetry as in the bulk, albeit with modified internal coordinates. These NNO phases are decomposed into five irreps [Figure 4.7(b)] with the only difference between bulk NNO and thin film NNO being that the thin film NNO is relatively more distorted than the bulk phase. Note that our zero-kelvin DFT calculations identified $P2_1/c$ as the ground-state crystal structure for homoepitaxially strained NNO under experimentally determined lattice parameters, consistent with the experimental structure at low temperature [**121**]. In Figure 4.7(b), we compare the relative distortion-mode amplitudes of NNO on STO thin films and bulk NNO (RT phase). In all cases, we find large and finite amplitudes for the M_2^+ Jahn-Teller mode in NNO on STO film with $P2_1/c$ symmetry; we also detect a relatively large amplitude for R_3^+ Jahn-Teller mode. It is the presence of these dominant Jahn-Teller distortions in the NNO thin films that produce the large dichroism and orbital polarization [Figure 4.6(a)].

Therefore, our distortion-mode analysis clearly discerns the difference in the lattice response of LNO and NNO thin films subjected to large epitaxial tensile strain. The propensity for orbital polarization in $R\mathrm{NiO}_3$ thin films is strongly influenced by the crystal symmetry of bulk materials. In NNO thin films and bulk, we find clear evidence of Jahn-Teller distortions present, suggesting that further distortions of this type due to epitaxial constraints would cost small (if any) energy. It appears rather that bulk orthorhombic nickelates without regular NiO_6 octahedra and bond distortions prefer to accommodate epitaxial strain through additional bond elongations and contractions. In sharp contrast, the absence of orbital polarization in LNO films with regular NiO_6 octahedra is directly attributed to its bulk ground-state structure (space group $R\bar{3}c$), where the Jahn-Teller

modes are *prohibited by symmetry.* In this case, strain-induced Jahn-Teller distortions would likely result in large energetic penalties.

4.4. Summary

In summary, using a combination of high-resolution X-ray diffraction, polarization-dependent soft X-ray absorption spectroscopy, and a quantitative group theoretical analysis computed from DFT, we report that the preferred orbital configurations adopted by the thin films is the one that stays closest to the bulk, suggesting the strain-stabilized phases retain a "memory" of their bulk state. We suggest that knowledge of the structural distortions present in the bulk thermodynamic phases emerges as an essential and critical descriptor to guide materials selection for epitaxial thin films with desired orbital polarizations. Additional studies of different symmetry mismatch under different strain of perovskites should be done to advance our understanding for the rational design of heterostructure materials with orbital-lattice interaction.

CHAPTER 5

Dynamic layer rearrangement during growth by oxide molecular beam epitaxy

Overview

The $A_{n+1}B_nO_{3n+1}$ Ruddlesden-Popper homologous series offers a wide variety of functionalities including dielectric, ferroelectric, magnetic and catalytic properties. Unfortunately, the synthesis of such layered oxides has been a major challenge owing to the occurrence of growth defects that result in poor materials behavior in the higher-order members. To understand the fundamental physics of layered oxide growth, we have developed an oxide molecular beam epitaxy system with *in situ* synchrotron X-ray scattering capability. We present results demonstrating that layered oxide films can dynamically rearrange during growth, leading to structures that are highly unexpected on the basis of the intended layer sequencing. Theoretical calculations indicate that rearrangement can occur in many layered oxide systems and suggest a general approach that may be essential for the construction of metastable Ruddlesden-Popper phases. We demonstrate the utility of the new-found growth strategy by performing the first atomically controlled synthesis of single-crystalline $La_3Ni_2O_7$.

5.1. Introduction

The atomic-level synthesis of functional oxides and an understanding of their growth behavior provide opportunities to explore and control the intriguing properties of artificial layered oxide heterostructures [23, 12, 22]. Oxide molecular beam epitaxy (MBE) has long been known to be a technique uniquely suited to the deposition of layered oxide materials that cannot be stabilized in bulk form [130, 131, 27], as the shuttered deposition process permits the construction of a material atomic layer by atomic layer. However, the desire for high crystal quality requires sufficient adatom mobility to achieve the two-dimensional growth mode, where each layer is completed before the next layer begins. With the elevated temperatures necessary for this mobility, other kinetic pathways (or other phases) may become competitive, and the resulting structure will be dictated by local thermodynamic and kinetic considerations [132].

A long-standing challenge in the oxide thin-film community has been the growth of $(AO)(ABO_3)_n$ Ruddlesden-Popper compounds [133], which consist of n unit cells of perovskite ABO_3 alternated with a layer of rocksalt AO along the crystallographic c-axis. As an illustration of the utility of oxide MBE for the synthesis of layered phases, Ref. [134] reported the growth of the first five members of the $(SrO)(SrTiO_3)_n$ homologous series ($n = 1$–5), and Ref. [26] recently demonstrated the growth of a structure with n=10. However, only a few members of the series are thermodynamically stable [135, 136, 137]. For this reason, as well as the high sensitivity of the material to the local Sr concentration, the resulting structures often exhibit intergrowth defects [138, 139, 140]. This highlights a clear need to quantitatively understand the interrelationships between the deposition

process and naturally driven processes occurring within the growing crystal such that artificially layered structures can be more readily synthesized.

Here, we describe the results of a detailed study conducted on the initial growth of Sr_2TiO_4 ($n = 1$) on TiO_2-terminated $SrTiO_3$ (001) substrates [58, 141], finding that the initial layers reconstruct through layer exchange into $SrTiO_3$ ($n = \infty$). The reaction can be understood from the energetics of different layer configurations determined with computational theory, and insight from these calculations is used to form the Sr_2TiO_4 phase directly by modification of the initial layering sequence. We then show the generality of the layer exchange phenomenon and demonstrate the utility of our growth strategy by stabilizing a new single-crystalline phase in the lanthanum nickelate system.

5.2. Experimental Results and Discussions

5.2.1. Layer swap during the growth of Sr_2TiO_4

We employed a newly constructed oxide MBE system, built from an existing *in situ* X-ray chamber at Sector 33ID-E of the Advanced Photon Source (APS) [65]. The $(SrO)(SrTiO_3)_n$ films were grown at 750 °C and in 10^{-6} Torr of O_2 using a Sr effusion cell and a Ti-Ball^{TM} source. Growth rates ranged from 1 to 3 min per monolayer depending on the species. Immediately following the shuttered deposition of each atomic layer, with the sequence SrO → SrO → TiO_2 → SrO, we measured the scattered intensity under growth conditions along the out-of-plane direction ($00L$) at non-resonant (15 keV, below the Sr K-edge) X-ray energies. The X-ray results are shown in Figure 5.1(a), and the expected structure is shown in Figure 5.1(b). It can be readily observed that the intensity profile along the $00L$, that is, the specular crystal truncation rod (CTR), for SrO no. 3 is virtually

identical to that for SrO no. 2, which corresponds to the structure of a double SrO layer on the $SrTiO_3$ substrate. If the CTR for SrO no. 3 represents the same structure, this suggests that the TiO_2 has exchanged places with SrO no. 2, as depicted by the arrows in Figure 5.1(b). This interpretation was confirmed by quantitative fitting of the specular

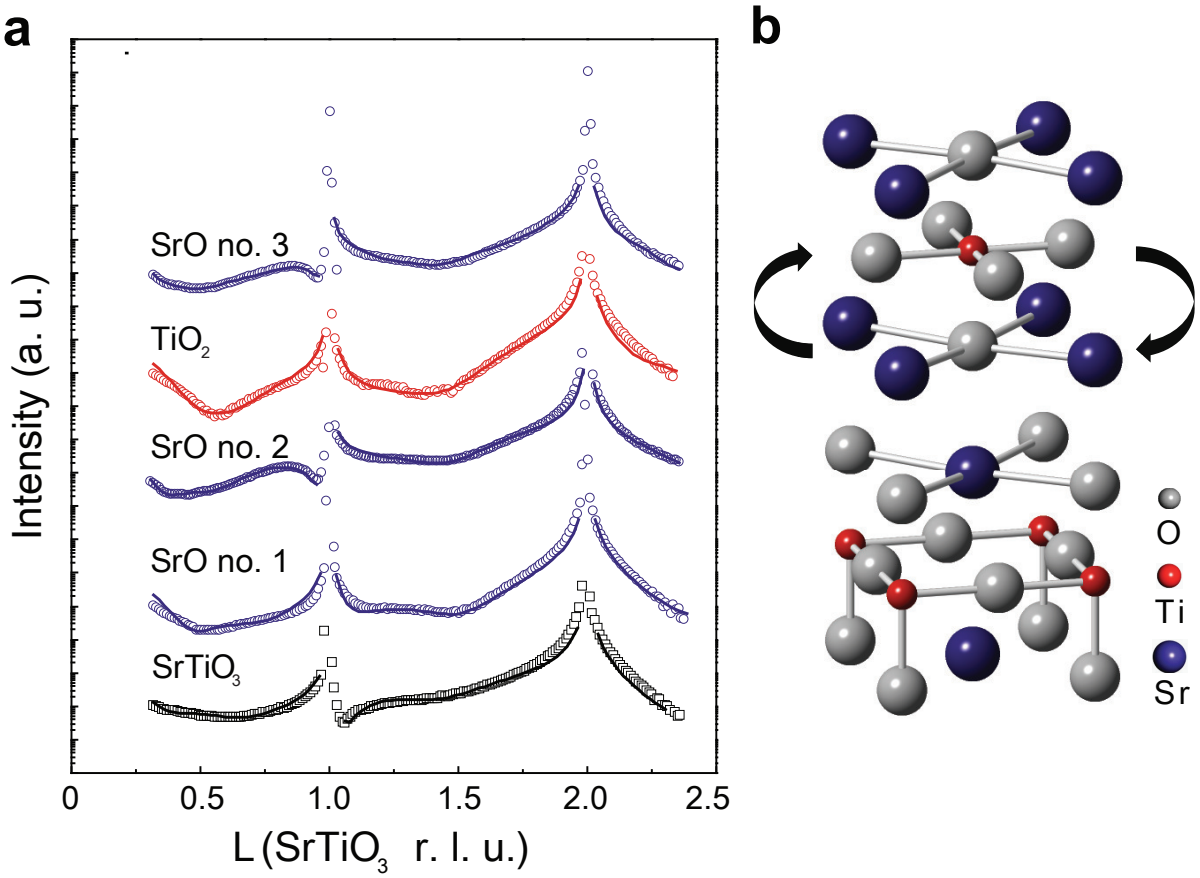

Figure 5.1. Layer swap during the growth of Sr_2TiO_4. (a) Scattered intensities along the $00L$ measured immediately after shuttered growth of each layer in the following sequence: SrO $\rightarrow$ SrO $\rightarrow$ TiO_2 $\rightarrow$ SrO (from bottom to top). The measured data are represented by symbols, and fitted intensities are represented by solid lines. (b) The expected atomic structure of film based on the growth sequence and proposed layer swap that occurs in the real growth. © 2014 Nature Publishing Group.

CTRs, revealing that the rearrangement happened either during or after growth of the TiO_2 layer such that SrO $\rightarrow$ SrO $\rightarrow$ TiO_2 deposition forms the SrO-TiO_2-SrO structure.

In order to obtain the real space structure, we performed an electron density analysis known as coherent Bragg rod analysis (COBRA) [**90**, **142**]. The depth dependences of the electron densities obtained by this analysis on (00L) rods of bare $SrTiO_3$ and SrO no. 1 (Figure 5.1(a)) are shown in Figure 5.2(c) and (d). The peaks with alternating heights correspond to the SrO (higher peaks) and TiO_2 (lower peaks) planes. The origin of the horizontal axis is chosen to lie at the top TiO_2 layer of the TiO_2-terminated $SrTiO_3$ substrate which is labeled by a black dash line. The nominal interface is thus just to the right of the origin, with the peaks in the negative z region belonging to the nominal substrate, and the peaks between $z = 0$ and 5 Å being due to the nominal film region. The flat and very low electron density beyond the sample, $z > 5$ Å, corresponds to the air region. The surface layer of the bare $SrTiO_3$ substrate is, as expected, the TiO_2 plane for the TiO_2-terminated $SrTiO_3$ and the SrO plane for SrO no. 1 which corresponds to the structure after deposited one SrO layer on the $SrTiO_3$ substrate. However, the COBRA result indicates the structure of a partial coverage double SrO layer on $SrTiO_3$ substrate which is consistent with the real time X-ray studies that will be discussed in chapter 6. The atomic layer spacings for both samples as functions of the depth are shown in Figure 5.2(e) and (f). As shown in Figure 5.2(e), there is a significant expansion of the top $SrTiO_3$ cell volume of TiO_2-terminated $SrTiO_3$ substrate. These expansions could be caused by oxygen vacancies, or small changes in the cation stoichiometry.

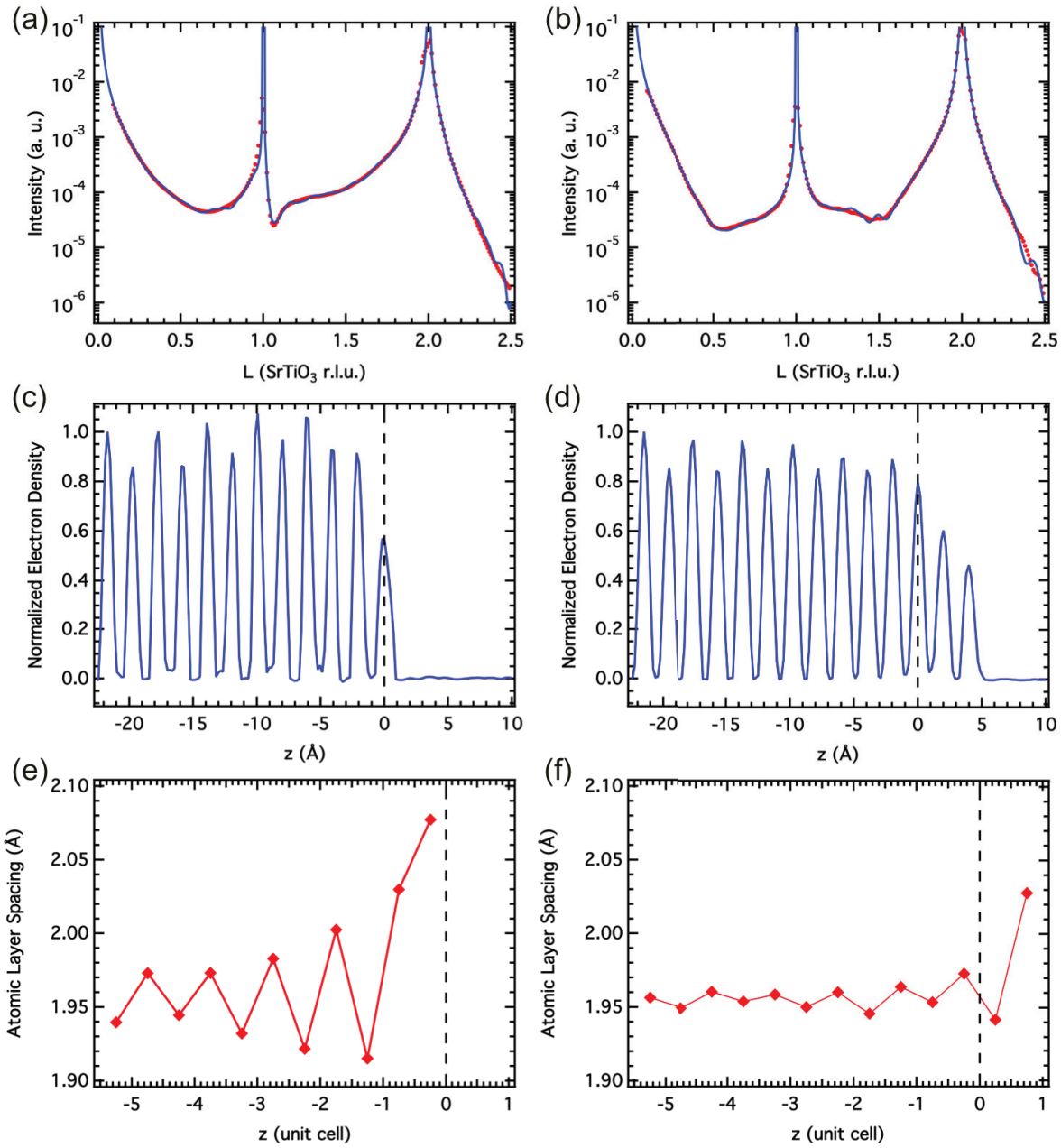

Figure 5.2. X-ray scattering intensity profiles along the (00L) for (a) bare $SrTiO_3$ and (b) SrO no. 1. Reciprocal lattice units (r.l.u.) are defined by the cubic $SrTiO_3$ substrate. Closed symbols show the experimental results, and the solid curve shows the result of the least squares fitting. The depth profiles of the electron density, obtained from the electron density analysis performed on the (00L) rod are shown in (c) for bare $SrTiO_3$ and (d) for SrO no. 1. The depth dependence of the layer spacing of the peaks shown (a) and (b) are shown in (e) for bare $SrTiO_3$ and (f) for SrO no. 1

5.2.2. Time evolution of scattered intensity during growth

During shuttered growth of our films, we monitor the scattered intensity at the $(0, 0, 1/2)$ position (in reciprocal lattice units of $SrTiO_3$). This "anti-Bragg" position is midway between the substrate Bragg peaks and is thus highly sensitive to surface roughness [70]. The time evolution shown in Figure 5.3 takes place after the deposition of two consecutive SrO layers and during the shuttered growth of TiO_2. We employed a Pilatus detector [Dectris®], which allows the specification of regions of interest for both the signal (blue

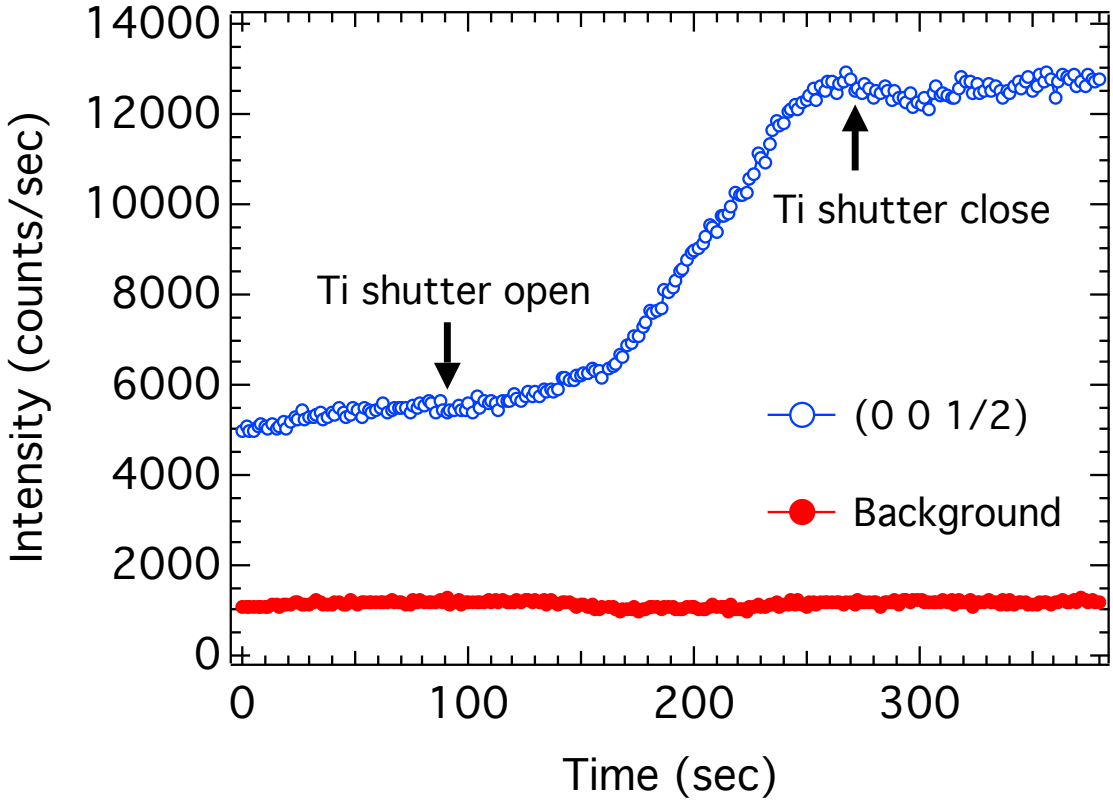

Figure 5.3. Time evolution of the scattered intensity at the $(0, 0, 1/2)$ position during TiO_2 layer deposition on a SrO bilayer. Intensities from the both the signal (blue curve) and background (red curve) regions of interest are shown. © 2014 Nature Publishing Group.

curve) and the background (red curve). The opening and closing of the shutter for the Ti-Ball^{TM}are indicated with arrows. As seen from the time evolution of scattered intensity at the highly surface-sensitive anti-Bragg position (Figure 5.3), no evolution in surface roughness takes place before the opening of the shutter or after the closing of the shutter and changes are observed only with the Ti shutter open, implying that layer exchange occurs during TiO_2 growth and is complete by the time one monolayer coverage of TiO_2 is reached.

5.2.3. Energetics for different layer sequencing during growth

To understand the energetic driving force for this layer rearrangement, Dr. Guangfu Luo and Prof. Dane Morgan calculated and compared the energies of different stacking sequences using density functional theory (DFT) [125, 143] as well as with the empirical modified Buckingham potential [144]. We performed *ab initio* calculations using DFT, as coded in the *Vienna Ab initio Simulation Package* (VASP) [125, 143]. We chose the PBEsol functional [122], which was demonstrated to be excellent for the description of bulk $SrTiO_3$ (Ref. [145]). The projector augmented wave method is used with the following potentials for $SrTiO_3$:O ($2s^2 2p^4$, E_{cut}=400.0 eV), Ti ($3p^6 3d^{10} 4s^2$, E_{cut}=274.6 eV) and Sr ($4s^2 4p^6 5s^2$,E_{cut}=229.3 eV). The plane-wave energy cutoff is set to 500 eV. We approximate the substrate with 20 atomic layers (∼3.7 nm) of cubic $SrTiO_3$, with the bottom 10 atomic layers fixed to the optimized bulk positions and the other layers relaxed. To reduce the mirror interactions between neighboring supercells, we add a vacuum slab as thick as 1.5 nm and consider dipole corrections in the out-of-plane direction. The

Table 5.1. Parameters for the modified Buckingham potential for STO [144]. © 2014 Nature Publishing Group.

	A (eV)	ρ (Å)	c (eV·Å^6)
$Sr^{1.331}$–$O^{-1.331}$	139621.961934	0.1963	2.33222
$Ti^{2.662}$–$O^{-1.331}$	18476.9466310	0.1963	0.00000
$O^{-1.331}$–$O^{-1.331}$	21943.2892770	0.2226	4.14616

supercells in the plane are one or two unit cell sizes large and the Monkhorst-Pack k-point grids for Brillouin zone sampling are $6 \times 6 \times 1$ and $4 \times 4 \times 1$, respectively.

The modified Buckingham potential [144] used in structural optimizations and in MD runs has the form

$$V = A_{ij} \exp\left(-\frac{r_{ij}}{\rho_{ij}}\right) - \left(\frac{c_{ij}}{r_{ij}^6}\right) + \frac{1}{2}\sum_{i=1}^{N}\sum_{j\neq i=1}^{\infty}\frac{q_i q_j}{r_{ij}} \ , \tag{5.1}$$

where r_{ij} is the distance between atom i and atom j. The values of the parameters for strontium titanate (STO) are listed in Table 5.1. The optimizations are performed using gradient-based techniques. The convergence criteria for energy and interatomic distances are 0.001 eV and 0.0005 Å, respectively. The molecular dynamics runs are carried out with the Verlet propagator and a step size of 5 fs. A Nosé type thermostat, as implemented in the DL_POLY software package, is used to control the temperature.

The goal of the MD simulations we performed is to shed light on the mechanism of the SrO and TiO_2 layer exchange. The size of the simulation cell in the lateral (x and y) directions, which are replicated using periodic boundary conditions, is 10×10 unit cells of STO. In the z direction (perpendicular to the surface), the simulation cell contains six layers starting with a TiO_2 layer at the bottom and followed by a stacking of SrO–TiO_2–SrO–SrO–TiO_2. The two bottom layers were frozen at the equilibrium

geometry at 0 K to mimic the effect of the bulk as obtained in the optimization of the STO lattice and to make the computation more efficient by reducing the number of atoms tracked by the calculation. The interaction between the atoms is modeled using the same potential given in Equation 5.1. What we were after was how the two upper layers swap to result in an alternating layered structure of STO, which is the energetically most preferred one. To understand this mechanism of rearrangement of the layers, MD simulations with the empirical potentials described above were conducted at different temperature values ranged from 1000 K to 1800 K in increments of 200 K. At each fixed temperature, the simulation time is 50 ns, with an extra 1 ns added at the start of each simulation to allow for full thermalization. As expected, increase of temperature results in increasingly more vigorous displacements of the atoms from their equilibrium positions. As shown

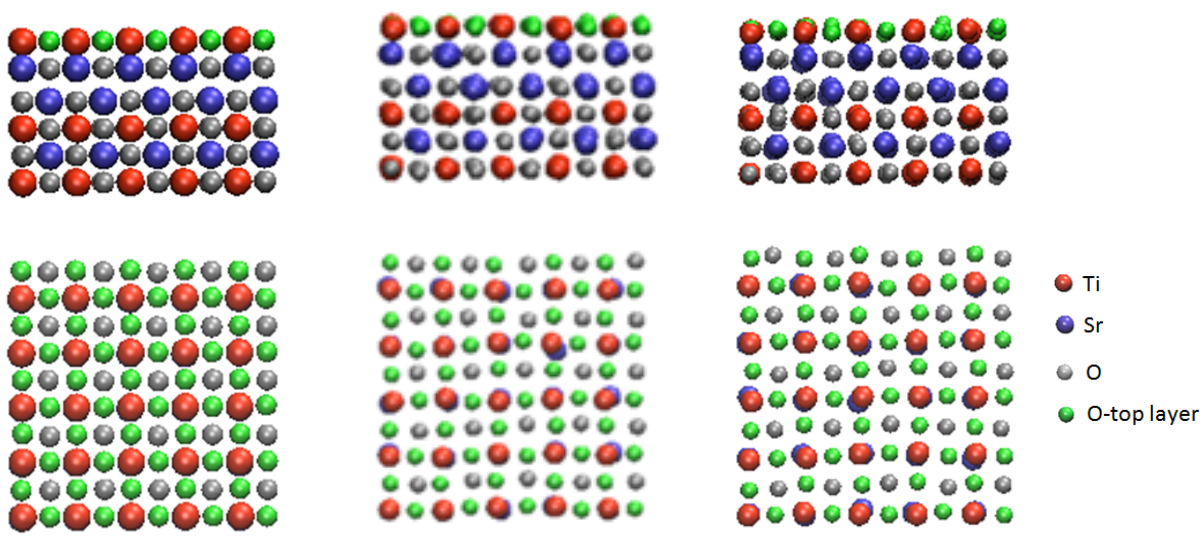

Figure 5.4. Snapshots of MD simulation. (a) Zero-temperature structure with with no defects (input configuration in the MD simulations). (b) Structure of the configuration at $t = 500$ ps in an MD run at 1200 K. (c) The same as (b) but at $t = 30$ ns. Upper: side view; Lower: top view. © 2014 Nature Publishing Group.

in Figure 5.4, simulations with no void defects in the structure do not show exchange of atoms between the surface and subsurface layers on the time scales considered here even at the highest temperatures.

We first compared two structures comprised of the TiO_2-terminated $SrTiO_3$ substrate with two SrO layers and one TiO_2 layer, as shown in Figure 5.5(a),(b), respectively. Relative to the intended SrO–SrO–TiO_2 structure, the SrO–TiO_2–SrO structure is more stable by ∼0.6 eV per Ti atom. This demonstrates that there is a significant thermodynamic driving force to rearrange the layers from SrO–SrO–TiO_2 to a SrO–TiO_2–SrO structure, in agreement with the exchange observed in Figure 5.1. The good agreement between the

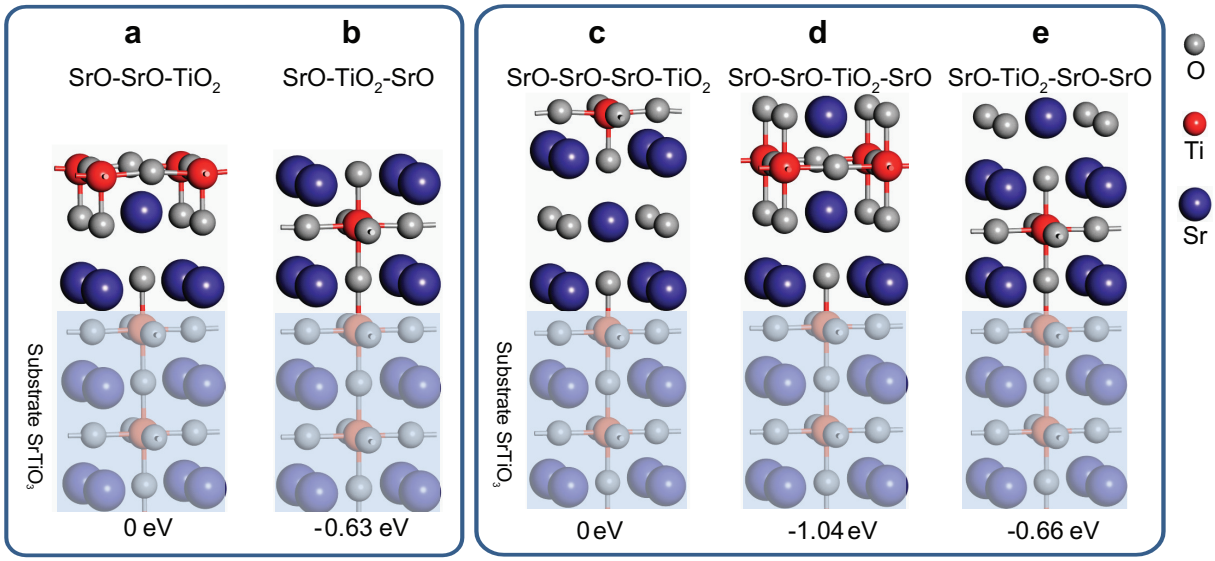

Figure 5.5. Energetics for different layer sequencing during growth. (a)–(e), Optimized structures and relative energies of different stackings of two (a,b) or three (c–e) SrO and one TiO_2 layer on a TiO_2-terminated $SrTiO_3$ substrate. Stackings are labelled by their layers from the first layer above the substrate surface to the top interface with vacuum. All relative energies are measured per unit cell and have the unit of electronvolts per exchanged Ti atom. Part of the substrate is indicated by shaded areas to guide the eyes. © 2014 Nature Publishing Group.

DFT and empirical potential results shows that the physics captured by the latter, that is, short-range bonding and electrostatics, dominates the exchange energetics.

5.2.3.1. Deposition order for the growth of Sr_2TiO_4 and $(SrO)_m(SrTiO_3)_n$ films on $SrTiO_3$(001)

We then considered the effect of a third consecutive SrO layer in the stacking sequence, as shown in Figure 5.5(c). The SrO–SrO–TiO_2–SrO structure [Figure 5.5(d)] was determined to be ∼1 eV per Ti atom more stable than SrO–SrO–SrO–TiO_2 and ∼0.4 eV per Ti atom more stable than SrO–TiO_2–SrO–SrO [Figure 5.5(e)]. TiO_2 will then exchange with the topmost SrO layer but not with the layer underneath. This result suggests that the immediate growth of the Ruddlesden-Popper phase can be accomplished by following the SrO → SrO → SrO → TiO_2 deposition sequence. We tested this hypothesis experimentally, again measuring the scattered intensity along the specular CTR after the growth of each layer. The final structure was SrO–SrO–TiO_2–SrO, as predicted, and continued growth of Sr_2TiO_4 can be accomplished by following the SrO → SrO → TiO_2 deposition sequence. Note that each TiO_2 layer will continue to exchange with the underlying SrO throughout the growth process, as the energetics for rearrangement change little as a function of film thickness [Figure 5.6(a)]. When the atomic layers SrO → SrO → SrO → TiO_2 are deposited on the TiO_2-terminated $SrTiO_3$(001) substrate, one unit cell of Sr_2TiO_4 capped with an extra SrO layer (SrO–SrO–TiO_2–SrO) are grown because of the layer swapping, as shown in Figure 5.6(a) (upper). When the atomic layers SrO → SrO → TiO_2 are deposited subsequently, the situation is similar to the deposition of SrO → SrO → SrO → TiO_2 considering the SrO layer capping. Figure 5.6(a) (lower) illustrates that the layer

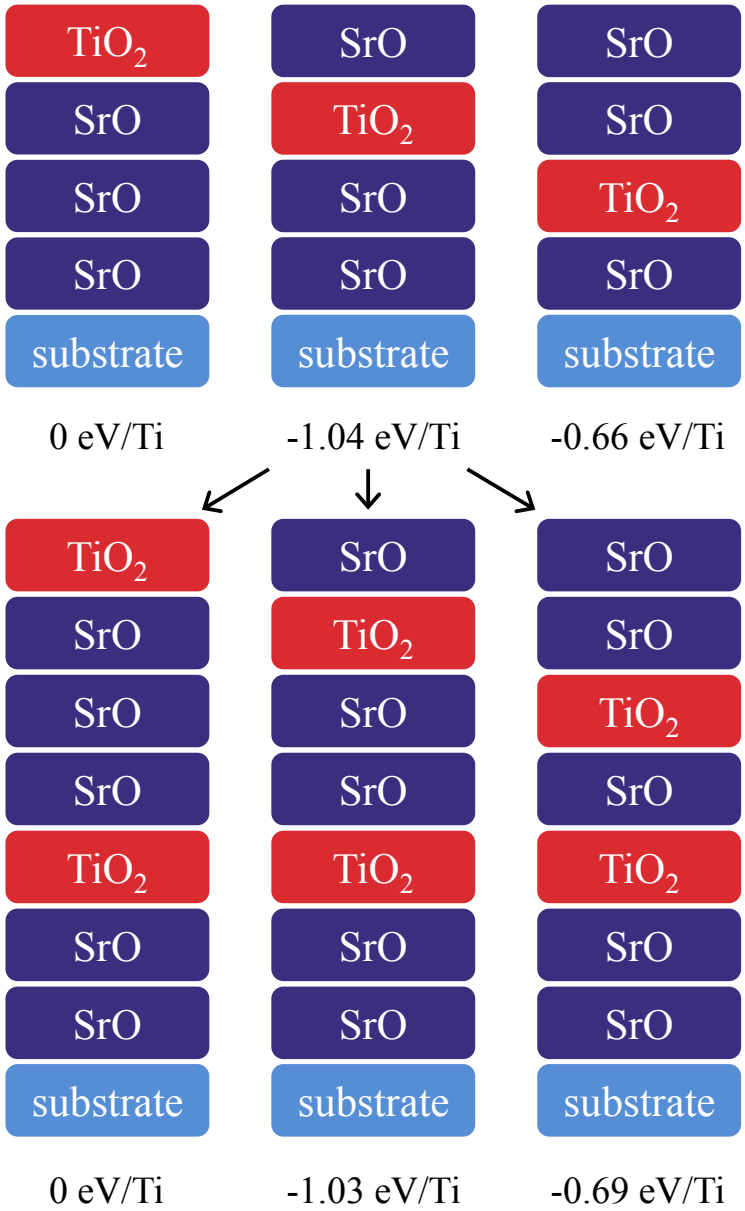

Figure 5.6. Strategy to grow Sr_2TiO_4 and $(SrO)_m(SrTiO_3)_n$. (a) Energy differences among different stackings in the growth of Sr_2TiO_4 films. (upper) Different possible stackings after the deposition of SrO → SrO → SrO → TiO_2; (lower) Different possible stackings after the subsequent deposition of SrO → SrO → TiO_2. The relative energy of each stacking is labeled at the bottom. (b) Illustration of the relationship between deposition order and the actual grown stacking for the first two unit cells of $(SrO)_m(SrTiO_3)_n$ film. © 2014 Nature Publishing Group.

swapping continues and the second unit cell of Sr_2TiO_4 is grown capped with a SrO layer. As a result, further growth of Sr_2TiO_4 films can be realized by continuing depositing atomic layers SrO → SrO → TiO_2. Thus, only one extra SrO layer in the initial sequence is needed to stabilize the proper sequencing for the Ruddlesden-Popper phase.

5.2.3.2. Structure of SrO bilayer with absorbing TiO_2 molecules

Although rearrangement of the initial SrO–SrO–TiO_2 structure is energetically favorable, the atomic pathway by which the configuration change occurs is less clear. One possible path is that Ti can move directly into the SrO layer, with the displaced SrO species presumably diffusing on top of the forming TiO_2 plane during deposition. Although direct insertion into a SrO layer by an isolated TiO_2 is a high-energy process, with a 2.71 eV energy barrier, our DFT studies show that a TiO_2 molecule on the SrO bilayer attracts two neighboring O atoms in the topmost SrO layer and forms a tetrahedral-like TiO_4 molecule, significantly disrupting the SrO layer and making it vulnerable to further attack. The topmost SrO layer is thus greatly distorted and a large hole around one O site of the SrO layer is created, similar as introducing an O vacancy in the plane. Figure 5.7 shows the structure of a TiO_2 molecule absorbing on the SrO bilayer.

When two TiO_2 molecules absorb on the SrO bilayer, as shown in Figure 5.8(a), both of the two molecules drag two O from the top SrO layer and form two tetragonal-like TiO_4 molecules, which subsequently induce two O vacancies in the SrO layer. Through a rotation [Figure 5.8(a)] and downward [Figure 5.8(b)] movement, one TiO_4 molecule squeezes a Sr atom out and inserts itself into the top SrO layer. As shown in Figure 5.8(c), this TiO_4 finally has its Ti atom at the original position of the squeezed-out Sr atom,

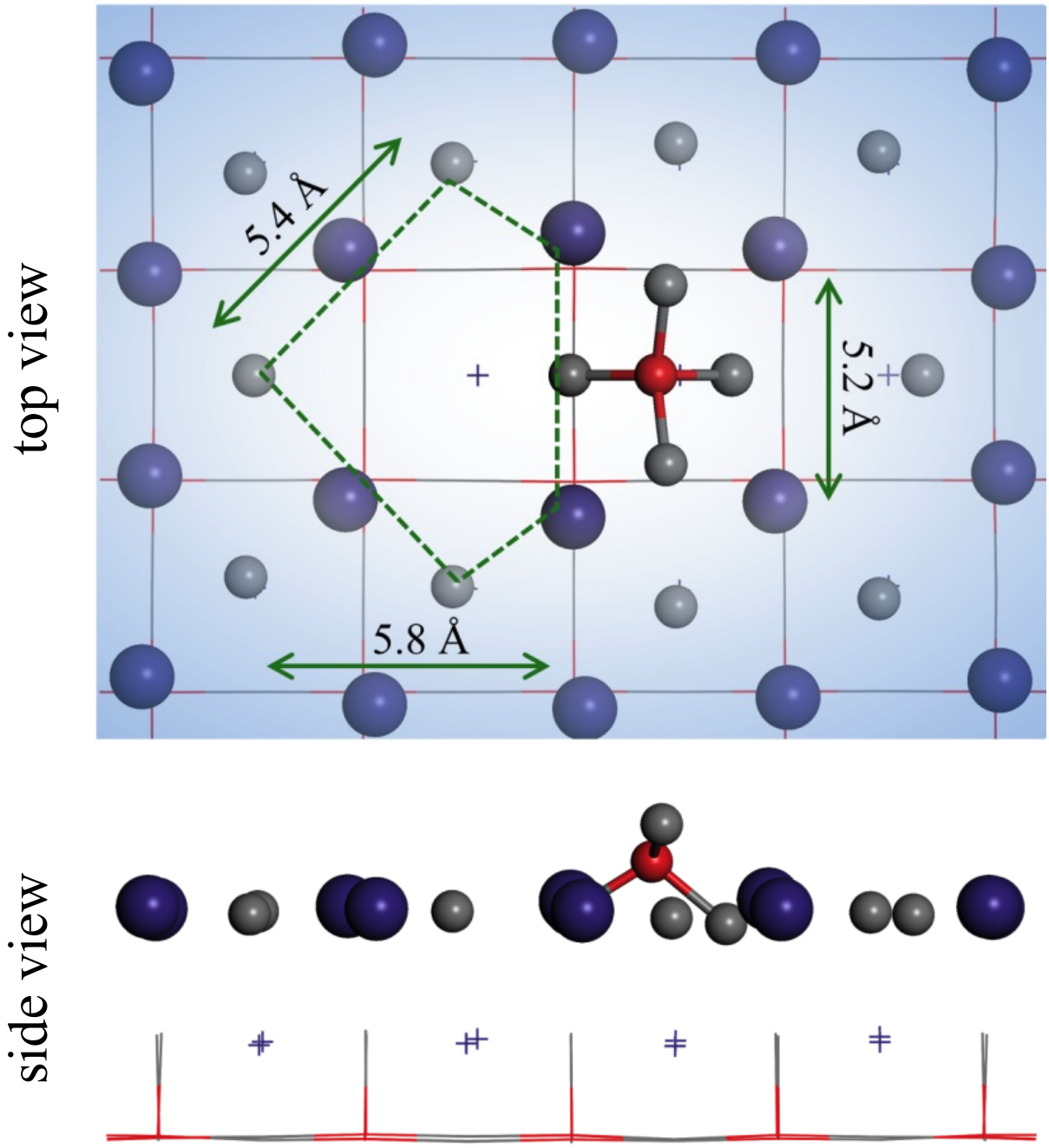

Figure 5.7. Structure of a TiO_2 molecule on the SrO bilayer. The hole and its size are indicated. Sr = large purple balls/dots, O = small grey balls/dots, Ti = small red ball/dots. © 2014 Nature Publishing Group.

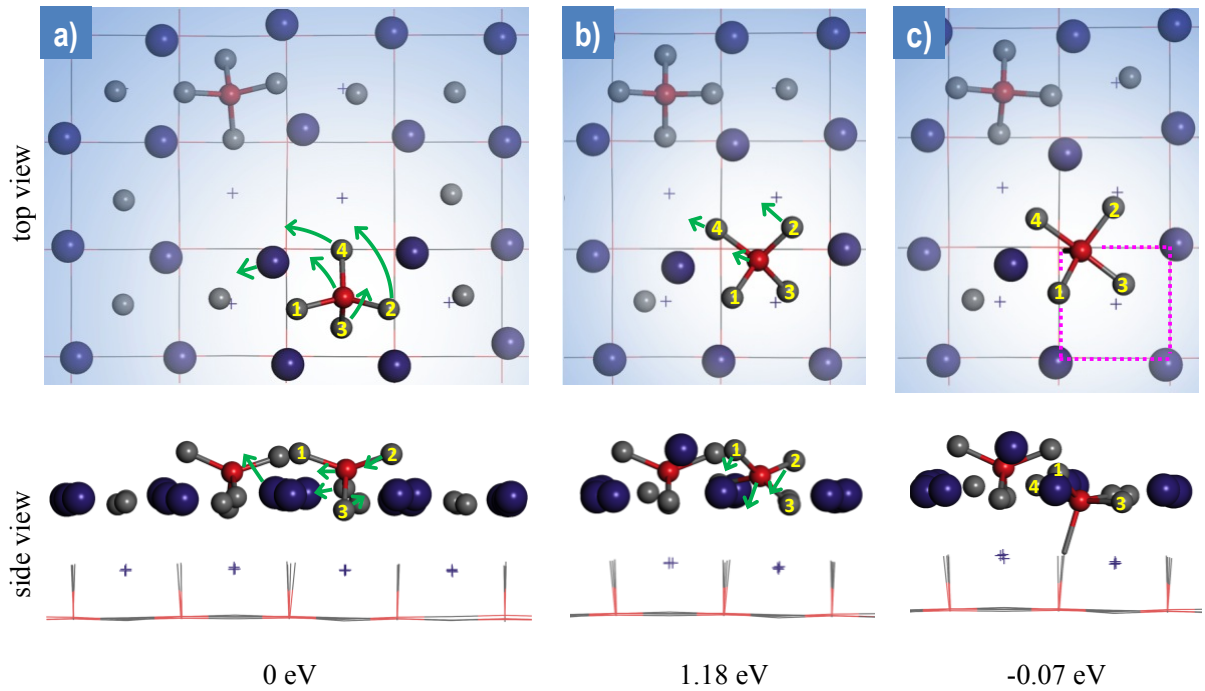

Figure 5.8. Insertion of a TiO_2 molecule into the SrO bilayer surface with the presence of another TiO_2 molecule. (a) Initial, (b) transitional, and (c) final state of this process. The green arrows indicate the atom movements from one state to another. Several atoms are labeled with yellow numbers to guide the eyes. Magenta dashed square indicates the TiO_2 lattice above the bottom SrO layer. Sr = large purple balls/dots, O = small grey balls/dots, Ti = small red balls/dots. © 2014 Nature Publishing Group.

three O (labeled as 2, 3, and 4) close to the O sublattice of the original SrO layer, and one O (labeled as 1) in the new TiO_2 network (magenta dashed square). The squeezed-out Sr becomes an adatom residing above the original SrO layer. The barrier of this insertion process is 1.18 eV, a process tacking place at the time scale of 10^{-7} sec at T = 1023 K. Thus, with two nearby TiO_2 molecules, the disruption can reduce the energy barrier to 1.18 eV ([Figure 5.8), and in the presence of a Sr vacancy there is no barrier to TiO_2 incorporation, yielding a potentially rapid exchange process that can easily occur during

the relatively slow TiO_2 deposition, especially given the presence of step edges, islands and defects that are connected to the synthesis of oxide thin films.

Molecular dynamics simulations with partial coverage of TiO_2 show movement of Sr atoms close to the edge of the TiO_2 island from the underlayer to the surface, which is also consistent with role of defects as a pathway for layer swapping (Figure 5.9). The vacancies are created by removing atoms from the optimized zero-temperature structure of the defect-free case. As shown in Figure 5.9, individual Sr atoms migrate from the SrO subsurface layer into and onto the TiO_2 surface layer pulling oxygen atoms from the surface layer with them. The vacancies created in the subsurface SrO layer by the interlayer migration of the Sr atoms are mobile. The situation is similar when vacancies are present in both the surface TiO_2 and the subsurface SrO layers, only the extent of the interlayer migration of atoms and the intralayer migration of vacancies is even more extensive. The simulations show that defects could be critical in initiating and sustaining an interlayer migration of atoms that could drive layer swapping for an existing SrO–SrO–TiO_2 stacking.

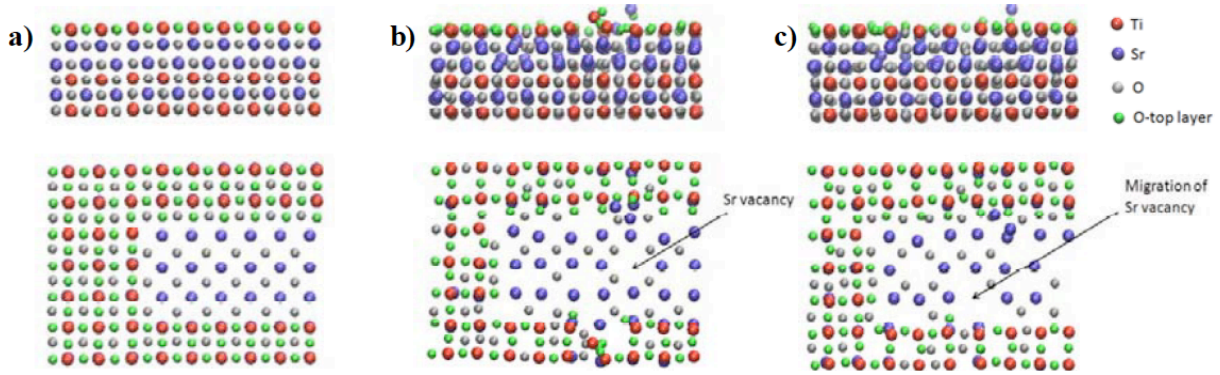

Figure 5.9. Snapshots of MD simulation. (a) Zero-temperature structure with an island vacancy in the surface TiO_2 layer (input configuration in the MD simulations). (b) Structure of the configuration at t=4 ps in an MD run at 1200 K. (c) The same as (b) but at t=12 ps. See the text for details. Upper: side view; Lower: top view. © 2014 Nature Publishing Group.

However, these results show only possible first steps in layer swapping and include only the simplest kind of disorder (point defects). Therefore, significant further work is needed to fully characterize the kinetics of layer swapping. Although the actual path that the system follows has not been observed directly, all of these mechanisms are consistent with our finding that the exchange is driven by TiO_2 layer deposition.

5.2.4. Layer swapping in additional systems

The results presented so far have been specific to strontium titanate Ruddlesden-Popper structures and Sr_2TiO_4 in particular. Such strategy can be easily generalized to the growth of $(SrO)_m(SrTiO_3)_n$ film, as shown in Figure 5.6(b). Moreover, our calculations indicate that layer exchange is expected quite generally for different stoichiometries and materials systems. First, as shown in Figure 5.10(a), we illustrate that it is always energetically favorable for a TiO_2 surface layer to exchange with the underlying SrO layer without regard to the number of consecutive SrO layers. According to Figure 5.10(a), deposited TiO_2 on $(SrO)_{m+1}$ always has a driving force to swap with the top SrO layer, after which kinetic limitations and almost zero energy gains are expected to stop the swapping, thereby forming $(SrO)_m(TiO_2)(SrO)$. To obtain the correct stacking of the first unit cell, one needs to deposit $(SrO)_{m+1}(SrTiO_3)_n$, which ends up with the stacking of $(SrO)_m(SrTiO_3)_n(SrO)$ because of the swapping. To obtain a subsequent unit cell, one needs to deposit $(SrO)_m(SrTiO_3)_n$ because of the existing SrO layer. With this understanding, one can gain atomic-level control over the growth of any arbitrary $(SrO)_m(SrTiO_2)_n$ Ruddlesden-Popper sequence, as illustrated in Figure 5.6(b).

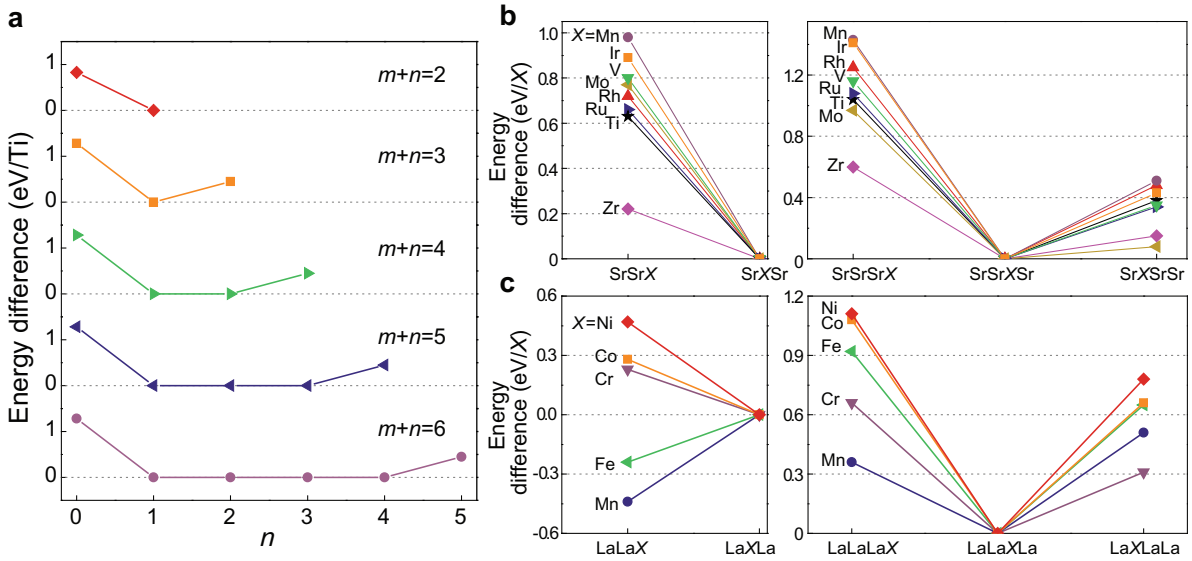

Figure 5.10. Layer swapping in additional systems. (a) Energy differences among stackings of (TiO_2-terminated substrate)–(mSrO)TiO_2(nSrO) for $m + n = 2, 3, 4, 5, 6$. For simple stacking notation, hereafter, we leave out the substrate and the O in an oxide layer. Thus, the (TiO_2-terminated substrate)–(mSrO)TiO_2(nSrO) is written as (mSr)Ti(nSr). (b) Energy differences among stackings of (mSr)X(nSr) at $m + n = 2$ and 3 for X = Ti, V, Mn, Zr, Mo, Ru, Rh and Ir in the B-site. (c) Energy differences among stackings of (mLa)X(nLa) at $m + n = 2$ and 3 for X=Cr, Mn, Fe, Co and Ni in the B-site. All calculations for magnetic systems are done with ferromagnetic ordering. © 2014 Nature Publishing Group.

Among stackings of (mSrO)TiO_2(nSrO), for $m + n > 2$, the most stable configurations are the ones accompanied by at least two SrO planes underneath and at least one SrO plane above the TiO_2 (that is, $m \geq 2$ and $n \geq 1$). These energies are in accordance with the results of Ref. [51], which reported that single TiO_2 planes surrounded by more than two consecutive SrO layers could be stabilized in a superlattice geometry even when the overall stoichiometry was not thermodynamically stable. Furthermore, we predict that layer rearrangement also occurs with other cations in the B-site, as shown in Figure 5.10(b).We considered seven other perovskite-forming B-site cations: V, Mn,

Zr, Mo, Ru, Rh and Ir. These systems have cation radii ranging from ∼67 to ∼86 pm and different magnetic moments, but all show trends similar to those in the Ti system. Cations in the antiferromagnetic (AFM) and nonmagnetic (NM) states behaved similarly to those in the ferromagnetic (FM) state, suggesting that magnetism plays a minor role in driving the rearrangement. Figure 5.11 and Figure 5.14 shows that the layer swapping persists in many systems and in different magnetic configurations. For the eight Sr-based systems (B cation X = Ti, V, Mn, Zr, Mo, Ru, Rh, Ir), the swapping from SrSrX to SrXSr and from SrSrSrX to SrSrXSr are always energetically favorable while that from SrSrXSr to SrXSrSr are unfavorable (Figure 5.11), regardless of the magnetic configuration.

5.2.5. Theoretical model on the relative energies of the substrate–mSrO–TiO_2–$_n$SrO stackings

Detailed analyses of the strontium titanate system reveal that the driving force for layer exchange can be understood in terms of the cleavage energies (for example, energy to pull two surfaces apart) of three relevant interfaces, which are largely independent of the surrounding environment. These interfaces are S/S, T/ST and T/SS, where S, T and / represent the SrO plane, the TiO_2 plane and the interface, respectively, and the energy differences of different stackings can be quantitatively modeled by cleavage energy differences. As illustrated in Figure 5.12(a), by adding a capping structure mSrO-substrate (A for short) on the top of two stackings, substrate–$(m+n)$SrO–TiO_2 (B for short) and substrate–mSrO–TiO_2-nSrO (C for short), we obtain the same complex, substrate–$(m+n)$SrO–TiO_2–mSrO–substrate (D for short). Therefore, the energies have

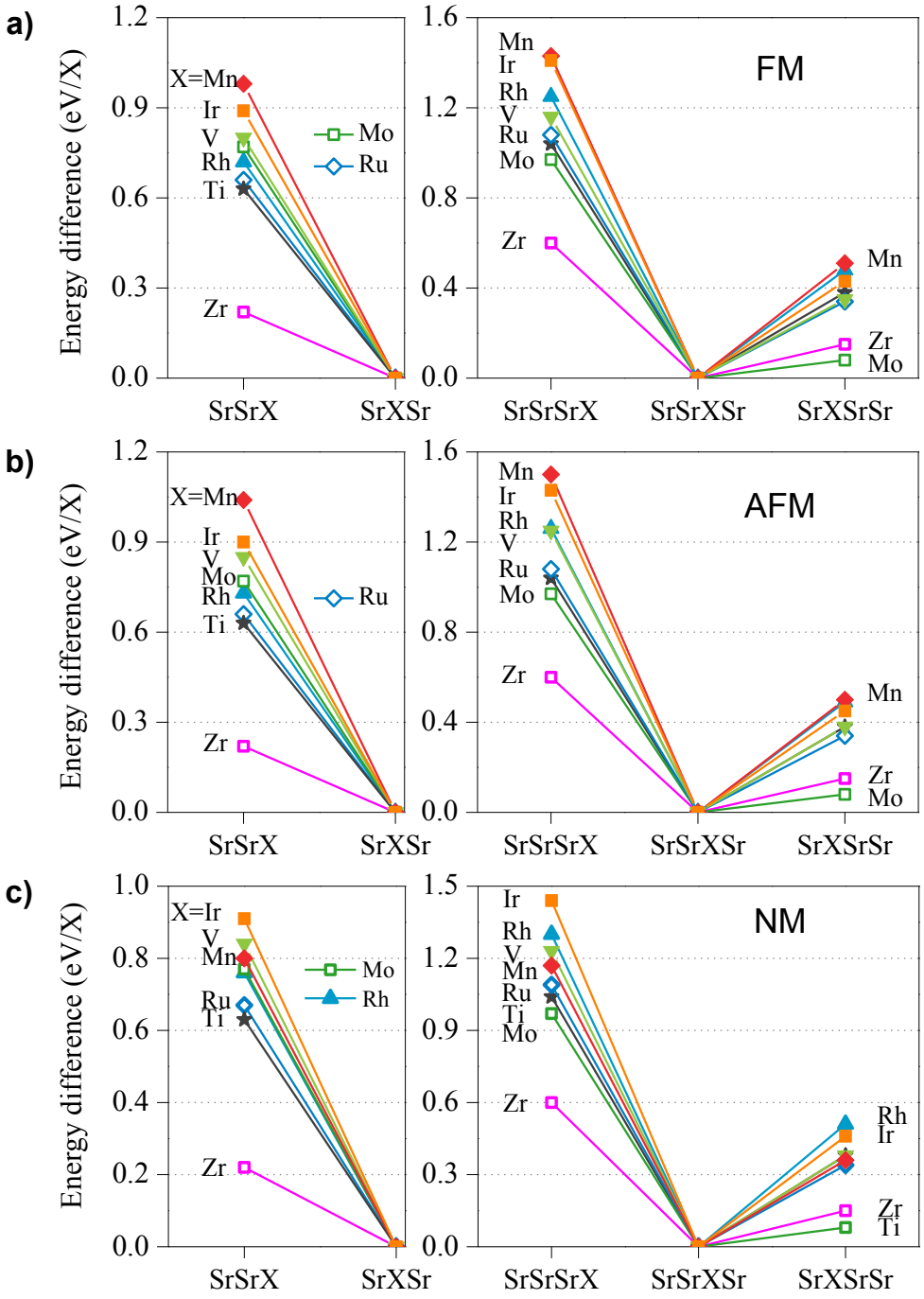

Figure 5.11. Swapping energies in different systems. (a)–(c) Energy differences among stackings (mSr)X(nSr) ($m + n = 2$ and 3) at the (a) FM, (b) AFM, and (c) NM states. The AFM state has the configuration of each spin up (down) X surrounded by four spin down (up) X. © 2014 Nature Publishing Group.

the following relationship

$$E_A + E_B = E_D + CE_{A/B}$$
$$E_A + E_C = E_D + CE_{A/C} \ , \tag{5.2}$$

where the $CE_{A/B}$ and $CE_{A/C}$ are the energy costs of cleaving D to A and B, and D to A and C, respectively. Simply subtracting these two equations shows that total energy difference $E_B E_C$ equals the cleavage energy difference $CE_{A/B} CE_{A/C}$. A careful check shows that the local stacking around the cleavage interface of A/B is TiO_2/SrOTiO_2 (T/ST for short) at $m = 1$ or TiO_2/SrOSrO (T/SS for short) at $m \geq 2$ and that of A/C is SrO/SrO (S/S for short). Further calculations prove that the cleavage energies of the three interfaces S/S, T/ST, and T/SS depend weakly on the surrounding environment

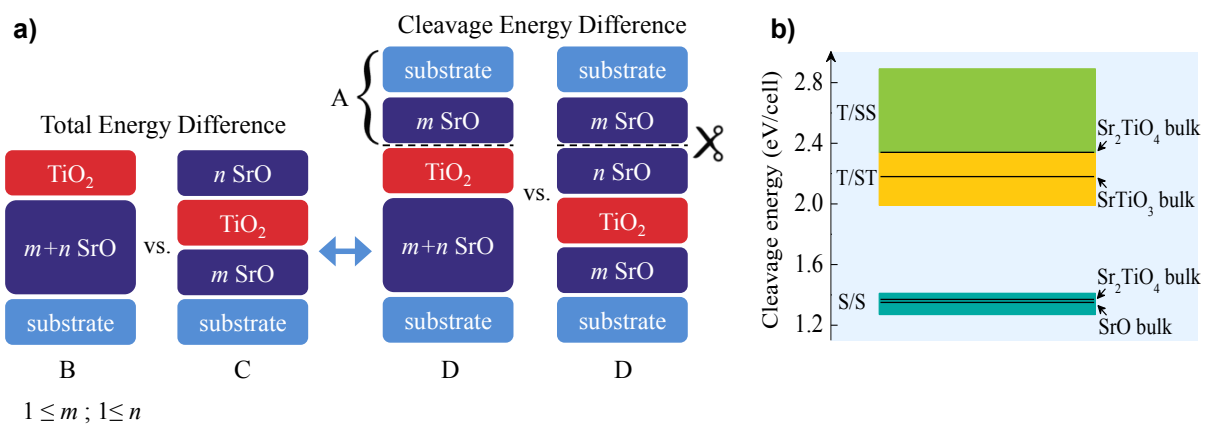

Figure 5.12. Explanation on the driving force of layer swapping. (a) Schematics of transforming the total energy difference between substrate–$(m+n)$SrO–TiO_2 and substrate–mSrO–TiO_2–nSrO to the cleavage energy difference of substrate–$(m+n)$SrO–TiO_2–mSrO–substrate along two different interfaces. The substrate is TiO_2 terminated. (b) Cleavage energy distribution of the S/S, T/ST, and T/SS interfaces surrounded by thick randomly stacked SrO and TiO_2 layers—except the TiO_2–TiO_2 stacking—on both sides. The specific values in the SrO, $SrTiO_3$, and Sr_2TiO_4 bulk (with the in-plane lattice lengths fixed to those of the substrate) are indicated by black lines. © 2014 Nature Publishing Group.

and have the order of S/S < T/ST < T/SS as seen in Figure 5.12(b). Therefore, in our model we can replace $CE_{A/B}$ with the average cleavage energy of T/ST ($m = 1$) or T/SS ($m \geq 2$), which are $\overline{CE}_{T/ST}$ or $\overline{CE}_{T/SS}$, respectively, and replace $CE_{A/C}$ with the average cleavage energy of S/S, which is $\overline{CE}_{S/S}$. Consequently, the relative energies of different stackings substrate–mSrO–TiO_2–nSrO at any fixed $m + n$ can be calculated using the following formula

$$E_B - E_C \approx \begin{cases} \overline{CE}_{T/ST} - \overline{CE}_{S/S} & \text{if } m = 1 \\ \overline{CE}_{T/SS} - \overline{CE}_{S/S} & \text{if } m \geq 2 \end{cases} \tag{5.3}$$

Wherein, $\overline{CE}_{S/S}$, $\overline{CE}_{T/ST}$, and $\overline{CE}_{T/SS}$ are, respectively, 1.34, 2.17 and 2.62 eV according to Figure 5.12(b).

The cleavage energies of the three interfaces are ordered as S/S (∼1.34 eV) < T/ST (∼2.17 eV) < T/SS (∼2.62 eV). This ordering is intuitive: the S/S interface is less stable than the T/ST interface because it contains fewer chemical bonds per unit area, and the T/SS interface is more stable than that for T/ST, owing to weaker bonding in the adjacent SS bilayer. Such energy ordering drives layer rearrangement to form more locally stable interfaces in place of less stable ones. Using the above-mentioned three cleavage energies in our model, we can accurately reproduce the DFT results in Figure 5.10(a), as shown in Figure 5.13.

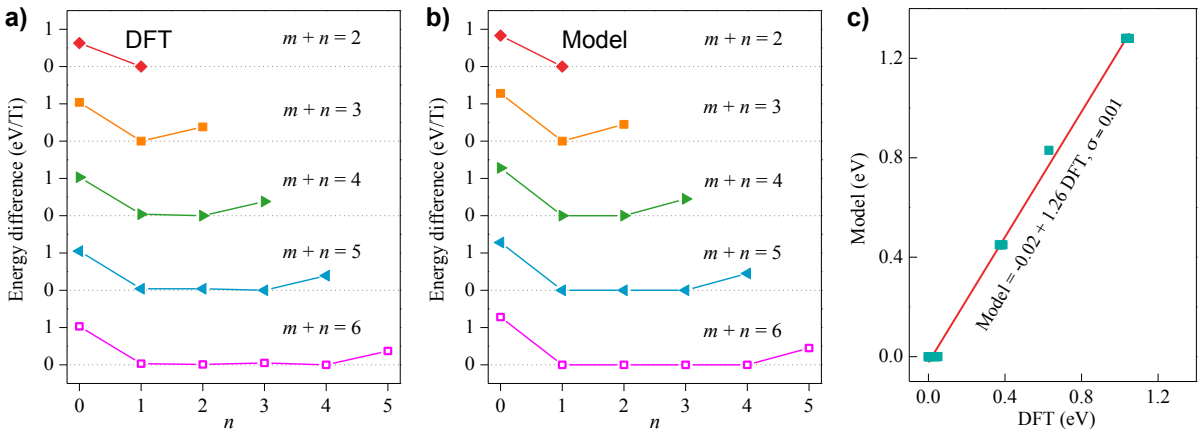

Figure 5.13. Energy differences among substrate–(mSrO)–TiO_2–(nSrO) for $m + n = 2, 3, 4, 5, 6$. Results from (a) DFT calculations and (b) our model based on the average cleavage energies of the S/S, T/ST, and T/SS interfaces. (c) Direct comparison between the DFT and model results. © 2014 Nature Publishing Group.

5.2.6. Synthesis of single-crystal $La_3Ni_2O_7$

Finally, we considered whether layer rearrangement is unique to strontium-based systems or can take place in other materials grown on $SrTiO_3$, such as the lanthanum-based transition-metal oxides, $La_{n+1}B_nO_{3n+1}$ (B cation X = Cr, Mn, Fe, Co, Ni). The La-based materials differ substantially from those of the strontium-based oxides in that the (001) planes are nominally polar [146], in contrast to the mostly charge-neutral planes in strontium systems. As observed in Figure 5.10(c), layer rearrangement is again expected to occur for many B-site cations. The exchange will always take place on LaO trilayers, regardless of the magnetic state (Figure 5.14). We do find, however, that the LaO–LaO–Mn and LaO–LaO–Fe structures are more stable than the LaO–Fe–LaO and LaO–Mn–LaO, whenever Mn or Fe are in the ferromagnetic (FM) or antiferromagnetic (AFM) state, which may originate from large magnetic interactions. However, such abnormality disappears in

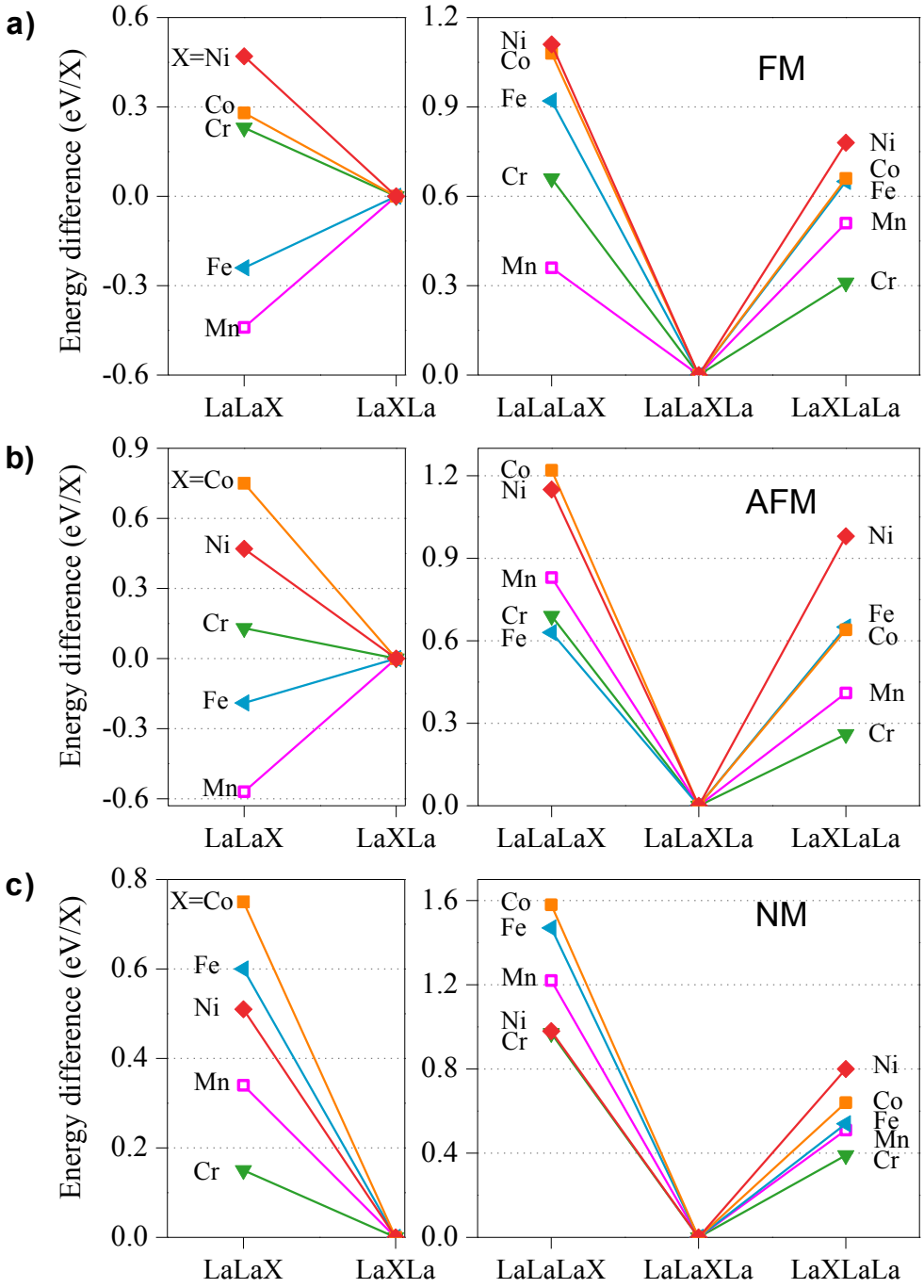

Figure 5.14. Swapping energies in different systems. (a)–(c) Energy differences among stackings (mLa)X(nLa) ($m + n = 2$ and 3) at the (a) FM, (b) AFM, and (c) NM states. The AFM state has the configuration of each spin up (down) X surrounded by four spin down (up) X. © 2014 Nature Publishing Group.

the nonmagnetic (NM) state, which suggests that this feature comes from the magnetic interactions in the two systems.

To illustrate how our insight can provide a pathway to stabilize new phases and to confirm our predictions, we conducted a set of *in situ* growth experiments for $(LaO)(LaNiO_3)_n$ similar to those for the strontium titanates. We used a growth temperature of 600 °C and employed ozone as the oxidant. As predicted in Figure 5.10(c), layer rearrangement was indeed observed, and the same strategy for producing Sr_2TiO_4 was used to grow both La_2NiO_4 and $La_3Ni_2O_7$. The $La_3Ni_2O_7$ structure was obtained by following the deposition sequence LaO → LaO → LaO → NiO_2 → NiO_2, which, after the predicted layer exchange, results in LaO–LaO–NiO_2–LaO–NiO_2 ordering. Note that by combining the shuttered growth technique with this strategy, one achieves a level of control over cation ordering greater than that of direct transfer from stoichiometric target [147]. The specular CTR from a film grown by six repeats of that sequence is shown as the red curve in Figure 5.15(a), and its corresponding X-ray absorption spectroscopy (XAS) profile measured at the Ni L_2-edge is shown in Figure 5.15(b). The specular CTR exhibits strong thickness fringes and film Bragg peaks, indicating sharp interfaces and high crystalline quality. For comparison, a sample grown with the LaO → LaO → NiO_2 → LaO → NiO_2 sequence is shown in black. There are no signs of the $La_3Ni_2O_7$ film Bragg peaks, and the scattered intensity exhibits signatures of a highly defective film. The XAS spectrum in Figure 5.15(b) is compared to that from a $La_3Ni_2O_{7-\delta}$ powder [148], where δ is 0 ± 0.02, as determined by thermogravimetric analysis, illustrating that the nickel valence has the expected value of ∼2.5+.

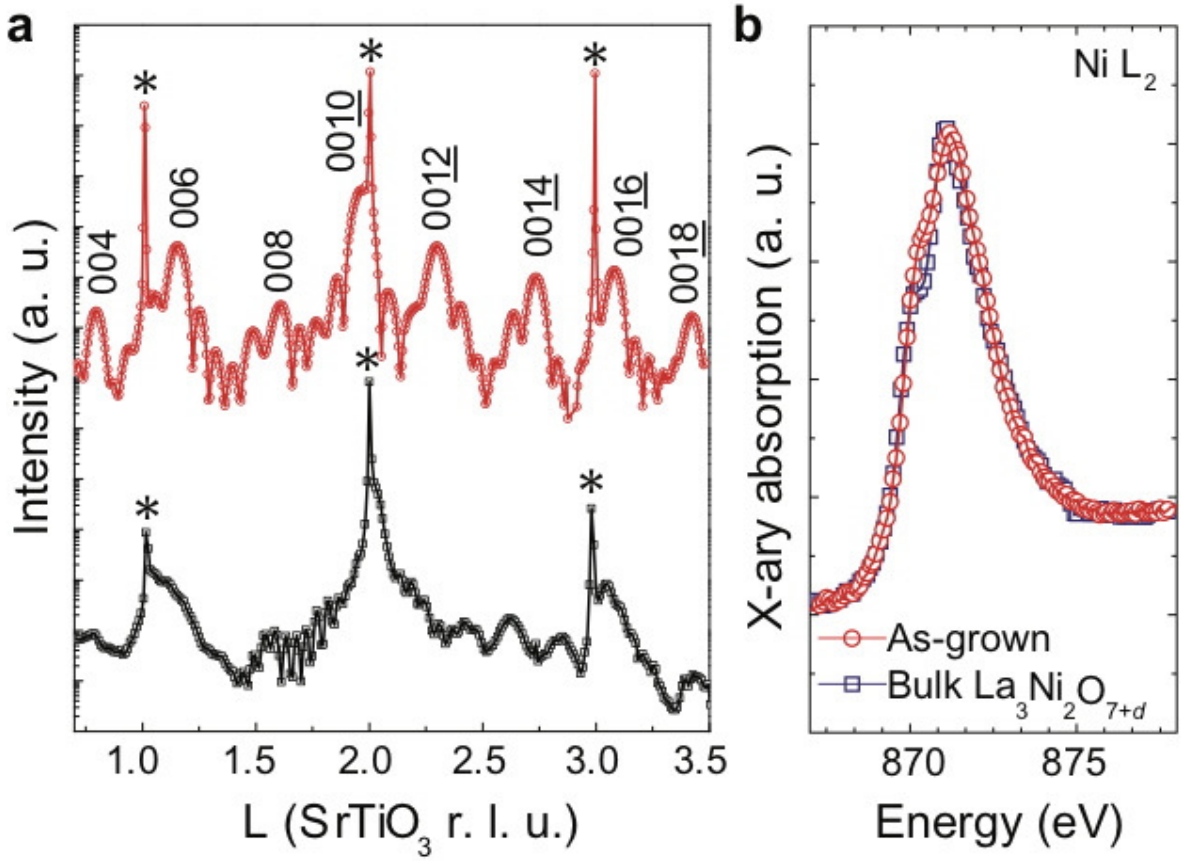

Figure 5.15. Synthesis of single-crystal $La_3Ni_2O_7$. (a) Specular crystal truncation rods for a film grown with the LaO → LaO → LaO → NiO_2 → NiO_2 sequence (red) and for film grown using the LaO → LaO → NiO_2 → LaO → NiO_2 sequence (black). Peaks from the $SrTiO_3$ substrate are indicated with asterisks. (b) X-ray absorption spectroscopy spectra for the $La_3Ni_2O_7$ film (red) and a powder sample (blue). © 2014 Nature Publishing Group.

5.3. Summary

The synthesis methodology used here, coupling quantitative *in situ* X-ray scattering with computational theory, is an approach that can be readily extended to other layered materials and heterostructures. Of particular interest are those predicted to exhibit new

properties but have yet to synthesized owing to various growth challenges, such as the polar $PbSr_2Ti_2O_7$ (Ref. [48]) or many of the layered oxides described in Ref. [149, 25, 49, 150]. One is not limited to simply layered oxides and can use this approach to explore wholly new oxide archetypes that have yet to be synthesized as thin-film heterostructures. We find the insights garnered when *in situ* X-ray results are fed back to computational theory to be of considerable importance as they allow the rapid formulation of growth strategies that may be critical to the material, even for deposition techniques as precise as MBE. This close integration with computational theory is an aspect of synthesis science that will become more essential as we create new materials by design and rapidly seek pathways to stabilize new phases.

CHAPTER 6

Time-resolved *in situ* X-ray Study of Homoepitaxial $SrTiO_3$ Growth Using Reactive Molecular-Beam Epitaxy

Overview

Homoepitaxial growth of $SrTiO_3$ thin films on (001)-oriented $SrTiO_3$ substrates by utilizing reactive molecular-beam epitaxy (MBE) was studied with *in situ* X-ray specular reflectivity and surface diffuse X-ray scattering. The time-resolved low-angle scattering exhibits a well-defined length scale associated with the spacing between unit-cell high surface features. We present *in situ* surface X-ray scattering results demonstrating that codeposition is consistent with a 2D island growth mode with unit-cell-high $SrTiO_3$ islands, but shuttered deposition proceeds by the growth of SrO islands which then restructure into $SrTiO_3$ unit cells during the deposition of the TiO_2 layer to form an atomically flat $SrTiO_3$ layer. Theoretical calculations indicate that the growth of one whole SrO layer is thermodynamically preferable, and the smoothing of SrO bilayer islands during the deposition of TiO_2 is energetically favorable, but kinetic processes cause the formation of SrO islands.

6.1. Introduction

Functional materials based on complex oxides in thin film form offer new and exciting strategies with potentially transformative properties for meeting many of our outstanding challenges in the field of energy technology [23, 12, 22]. The atomic-level synthesis of functional oxides and an understanding of their growth behavior provide opportunities to explore and control the intriguing properties of artificial layered oxide heterostructures [24, 25, 26].

Unfortunately, synthesis of such oxide films can be a major challenge even when utilizing reactive molecular-beam epitaxy (MBE), the most precise and powerful deposition technique that is often regarded to allow the construction of materials atomic plane by atomic plane and permits delivery of the cation fluxes to the substrate either at the same time (codeposition) or separately (shuttered deposition) [27]. Although either codepostion or shuttered deposition can be used to grow simple perovskites of the form ABO_3, the processes occurring during synthesis can be quite distinct, the later is uniquely suited to the manipulation of the cation sublattice on a monolayer level, permitting the growth of layered oxide materials that cannot be stabilized in bulk form [130, 51, 27] and studies on the effects of cation ordering on ground state properties and phase transitions [52, 53, 54].

Homoexpitaxial growth is a standard way of assessing the ability of a thin film growth technique to make materials, and it has been widely used in multiple techniques for the growth of semiconductors [151, 152]. When substrates are available, studies of homoepitaxial oxide thin films offer a straightforward approach to identify the growth modes without any strain and polarity effect. Despite decades of study, a complete description of the fundamental mechanisms of oxide growth by reactive MBE is still a

challenging problem. One question concerns the evolution of a film surface following by the arrival of newly deposited species. The surface may relax via multiple processes, including molecular formation and diffusion. This highlights a clear need to quantitatively understand the interrelationships between the deposition process and naturally driven processes occurring within the growing crystal. In addition, achieving atomic precision in heterostructure growth requires precisely controlled growth techniques and *in situ* characterization tools with atomic spatial resolution and the appropriate time resolution.

Due to the large scattering cross section of electrons, reflection high energy electron diffraction (RHEED) can provide direct information on surface roughness evolution during growth and is frequently the characterization technique used for real-time monitoring of both the thickness and the quality during thin film growth [**153**, **55**, **154**]. A report by Haeni et al. [**55**] has shown that the observed growth oscillations with RHEED at the specular spot can differ substantially from sample to sample, even for the homoepitaxial growth of $SrTiO_3(001)$, highlighting a fundamental lack of understanding of what takes place during oxide deposition. In contrast, the scattering cross section for X-rays is much smaller, thereby it eliminates multiple scattering which simplifying the quantitative interpretation of the data and making X-ray techniques nearly ideal for fundamental structural studies. By studying *in situ* X-ray scattering from the surface with powerful synchrotron radiation sources, it has already been demonstrated that one may determine the specific morphology for a given film-growth system [**155**, **156**].

In this chapter, we present an *in situ* synchrotron X-ray measurement of $SrTiO_3(001)$ homoepitaxial growth, comparing codeposition and shuttered deposition of Sr and Ti. We show that *in situ* surface X-ray diffuse scattering provides critical length scale information

absent from *in situ* specular X-ray reflectivity alone, at time scales appropriate to study oxide MBE. To understand the fundamental growth mechanisms of complex oxide thin films, insight into the results is provided by density functional theory (DFT) calculations. We find that while both techniques can be used to grow high quality $SrTiO_3$ epitaxial films, shuttered deposition takes place via an alternating wetting/non-wetting mechanism due to existence of kinetic barriers at the SrO surface. Finally, we note interesting diffuse scatter behavior when shuttered deposition was performed in the wrong order, i.e., with TiO_y first deposited onto the TiO_2-terminated $SrTiO_3$(001) substrate, followed by SrO_x (i.e., TiO_y/SrO_x).

6.2. Experimental Results and Discussions

To obtain information regarding morphological evolution in this system, we measured the low-angle x-ray scattering during homoepitaxial STO growth by oxide MBE. A 2D area detector (PILATUS 100K) was used to record both the specular X-rays scattering associated with out-of-plane electron density profile and the diffuse X-rays scattering associated with in-plane atomic correlations. Previous studies have taken advantage of this technique to study simultaneous in- and out-of-plane processes during homoepitaxial $SrTiO_3$ Growth by using pulsed laser deposition (PLD) [157, 158]. Moreover, immediately following the deposition of five monolayers (ML) of STO, we also measured the high-resolution X-ray reflectivity along the out-of-plane direction (00L) crystal truncation rod (CTR) at the growth temperature to determine the stoichiometry and thickness of the films.

We employed a newly constructed oxide MBE system, built from an existing *in situ* X-ray chamber at beamline 33-ID-E of the Advanced Photon Source (APS) [65]. The $SrTiO_3$ films were grown at 700 °C and in a background pressure of 10^{-6} Torr of molecular oxygen, using a Sr effusion cell and a Ti-Ball^{TM}source [159]. For shuttered deposition, both sources were shuttered to deposit alternating monolayer doses of SrO and TiO_2. For codeposition, both shutters were open for the duration of the growth. Prior to growth, shutter times were initially set based on flux measurements made using a quartz crystal microbalance (QCM) located directly in front of the substrate, and then precisely tuned by optimizing Kiessig (thickness) fringes with high-resolution X-ray reflectivity measurement on a calibration sample immediately prior to the growth of the sample sets. $SrTiO_3$ substrates were prepared using a termination recipe to achieve a TiO_2-terminated surface [58].

6.2.1. Time-resolved Diffuse X-ray Scattering Studies

The experimental geometry is illustrated in Figure 6.1. As suggested by the figure, steps on the STO surface resulting from the surface miscut are always aligned perpendicular to the incident beam. Then the X-ray scattering in the $Q_{\|}$ direction is only related to the island correlations on the surface [158]. During STO homoepitaxy for both co-deposition and shuttered-growth, we observed that the integrated diffuse and specular intensity oscillate at the same frequency, but out of phase as shown in Figure 6.2(e)(f). The specular oscillations indicate layer-by-layer growth of the STO films [160], while the diffuse peak oscillations indicate the formation and evolution of in-plane features during layer-by-layer growth [157, 158]. The shutter timing diagrams for codeposition and sequential deposition

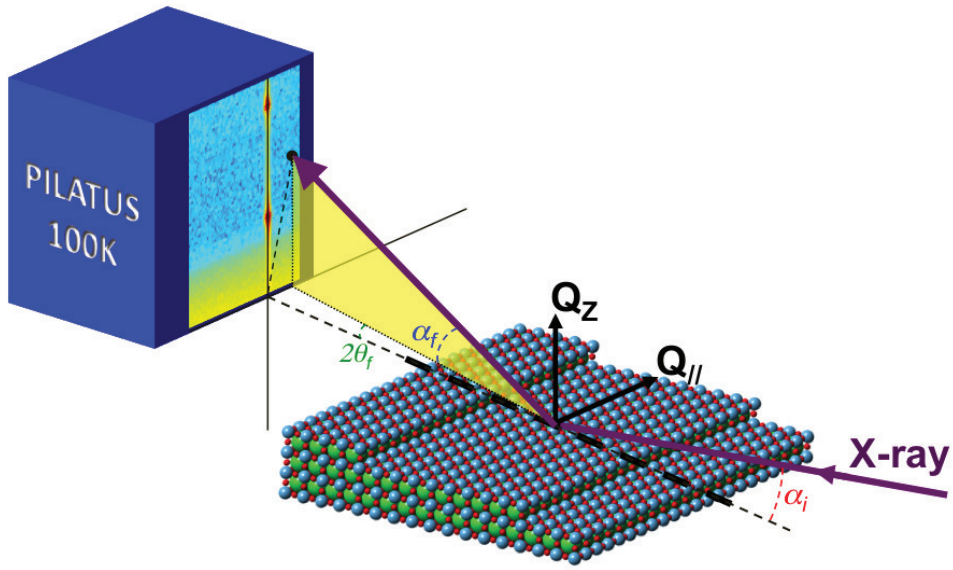

Figure 6.1. Experimental geometry for *in situ*, time-resolved diffuse X-ray scattering studies.

are shown in Figure 6.2(a) and (b) for five unit cells of STO growth. The Sr and Ti deposition rates were matched to provide 1 monolayer (ML) per 200 seconds such that the total growth time for shuttered deposition was roughly twice that for codeposition (with each $SrTiO_3$ unit cell corresponding to 1 ML of SrO and 1 ML of TiO_2). False color images of the specular intensity (at $Q_{\|} = 0$, $Q_z = \pi/3.912$ Å^{-1}) and adjacent diffuse scatter during growth are shown in Figure 6.2(c) for codeposition and (d) for shuttered deposition. As materials are deposited on the surface, the specular intensity drops while diffuse lobes of scattering appear on both sides of the specular rod although only one of them can be clearly seen on the detector due to our experimental geometry. The integrated intensities are shown in Figure 6.2(e) and (f), illustrating that the specular and diffuse intensities oscillate out of phase with each other. Others have shown that the diffuse

lobes are cuts through "Henzler rings" arising from 2D islands on the perovskite surface [161, 162]. While the presence of a distinct diffuse peak indicates a well-defined in-plane correlation length, the peak profile contains little information regarding feature shapes or size distributions [163]. In the case of codeposition, where the fluxes of Sr and Ti are roughly equal, the specular intensity decreases to a minimum and the diffuse intensity

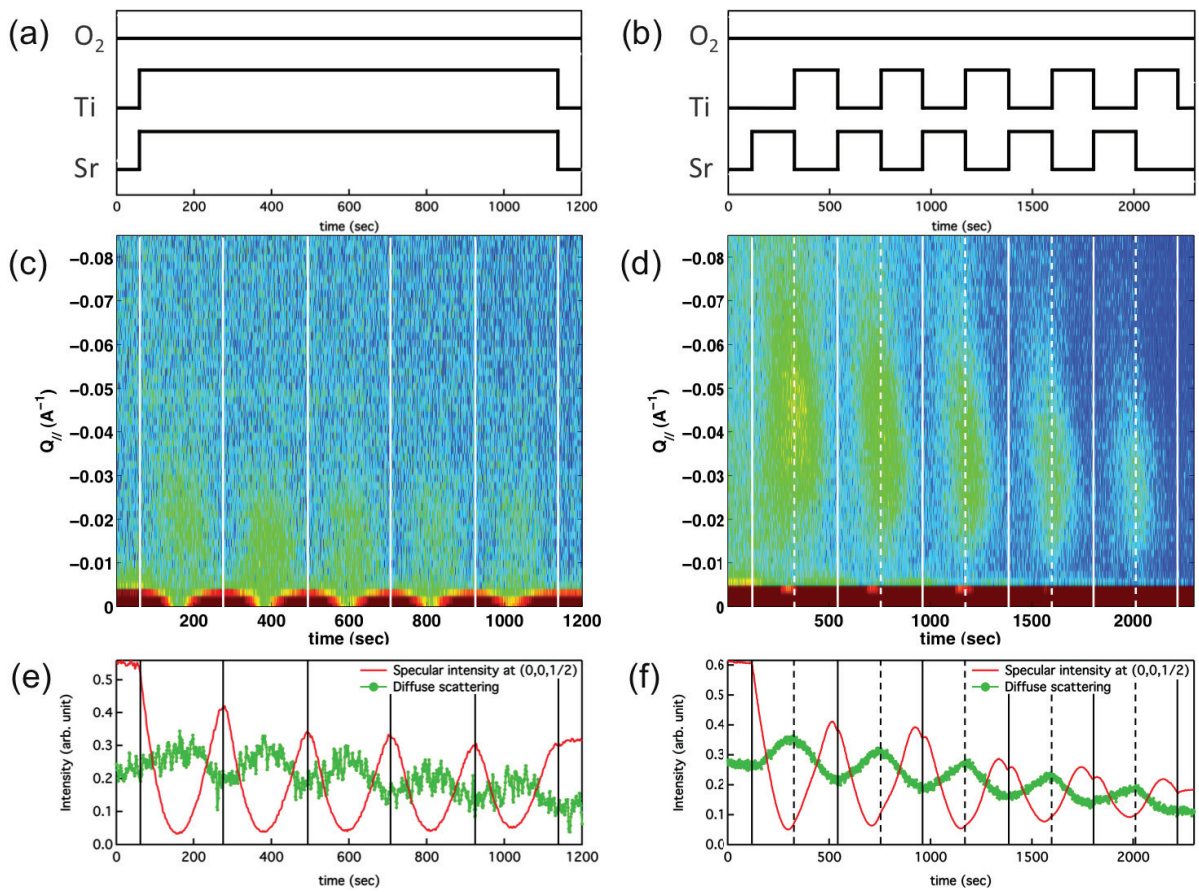

Figure 6.2. Timing diagram of the sequential deposition of strontium and titanium during the (a) codeposition and (b) shuttered deposition of five unit cells of $SrTiO_3$. Oxygen is provided continuously during both growths. Time-resolved diffuse X-ray scattering data shown in (c)(d) false color image and (e)(f) the corresponding integrated diffuse and specular intensity during $SrTiO_3$ homoepitaxy by codeposition and shuttered deposition, respectively.

rises to a maximum at a time corresponding to 50% coverage of 1-unit-cell-thick $SrTiO_3$; the peak in the diffuse scatter corresponds to a $\sim$ 40 nm in-plane correlation length. With continued growth, the specular (diffuse) intensity rises (decays) to a maximum (minimum) at 100% unit-cell coverages, consistent with a 2D island growth mode with unit-cell-high $SrTiO_3$ islands spaced $\sim$ 40 nm apart, nucleating/growing on the terraces and coalescing before the next unit cell starts [160].

Interestingly, during shuttered deposition of $SrTiO_3$, we observe similar behavior, but now the first minimum (maximum) in specular (diffuse) intensity no longer corresponds to a half unit cell coverage of $SrTiO_3$, but rather 1 ML coverage of SrO_x. However, upon deposition of TiO_y, the surface begins to smooth, leading to a maximum (minimum) in specular (diffuse) intensity with the completion of one $SrTiO_3$ unit cell. As shown in Figure 6.2(d) and (f), the process repeats with every Sr and Ti growth cycle, the only difference being progressively larger inter-island spacing and reduced diffuse intensities. It indicates that shuttered growth does not proceed by the nucleation and coalescence of single-layer-high SrO islands, followed by the same for TiO_2. Instead, the scattering indicates that the SrO grows as islands and then restructure into $SrTiO_3$ unit cells during the growth of the TiO_2 to form an atomically flat layer.

Also, the diffuse peak position shifts monotonically toward smaller values in $Q_{\|}$ direction with increasing film thickness in both codeposition and shuttered deposition. Since diffuse peak positions corresponds to a characteristic length scale of the average island separation at low layer coverage and changing to the separation between holes near layer completion, it reflects the growing surface retains a memory of the underlying layer if a new layer

nucleates before the last layer completes, and the unfilled holes becomes the adatom sinks thus reducing nucleation density and diffuse peak positions.

6.2.2. High-resolution X-ray Reflectivity

High-resolution X-ray diffraction is routinely employed to determine the composition of semiconductor epitaxial layers [164] and oxide thin films. The lattice constant of $SrTiO_3$ films is sensitive to stoichiometry. Nonstoichiometric $SrTiO_3$ films show an expansion of the out-of-plane lattice constant whether films are Sr-rich, Ti-rich [154, 165, 166] or oxygen vacancies [167, 168]. As shown in Figure 6.3, the measured X-ray scattered intensities along the (00L) CTR of the codeposited and shuttered deposited 5-unit-cell-thick films are similar, showing that the homoepitaxial $SrTiO_3$ film peaks are indistinguishable from the underlying $SrTiO_3$ substrate peak which means both samples have good stoichiometry without any observable expansion of the out-of-plane lattice constant [154]. However, intensity oscillations (thickness fringes) are observed for both $SrTiO_3$ films, despite the overlap of the film and substrate peaks, indicating smooth interfaces between the film and substrate, but also suggesting differences between deposited film and substrate [169]. Measured specular X-ray reflectivity data around STO (001) Bragg peak along (00L) CTR from $SrTiO_3$ films are compared with calculations shown in Figure 6.3 that account for the effects of film thickness, lattice parameter, c_{film}, fractional site occupancy, and an offset between film and substrate at the interface, δ_{film}, a schematic diagram of the atomic structure model was shown in the inset of Figure 6.3(b). Least-squares fitting was performed to confirm that all stoichiometric films are within 5% of the expected compositions based on shutter time adjustments except data points near the sharp STO (001) Bragg peak

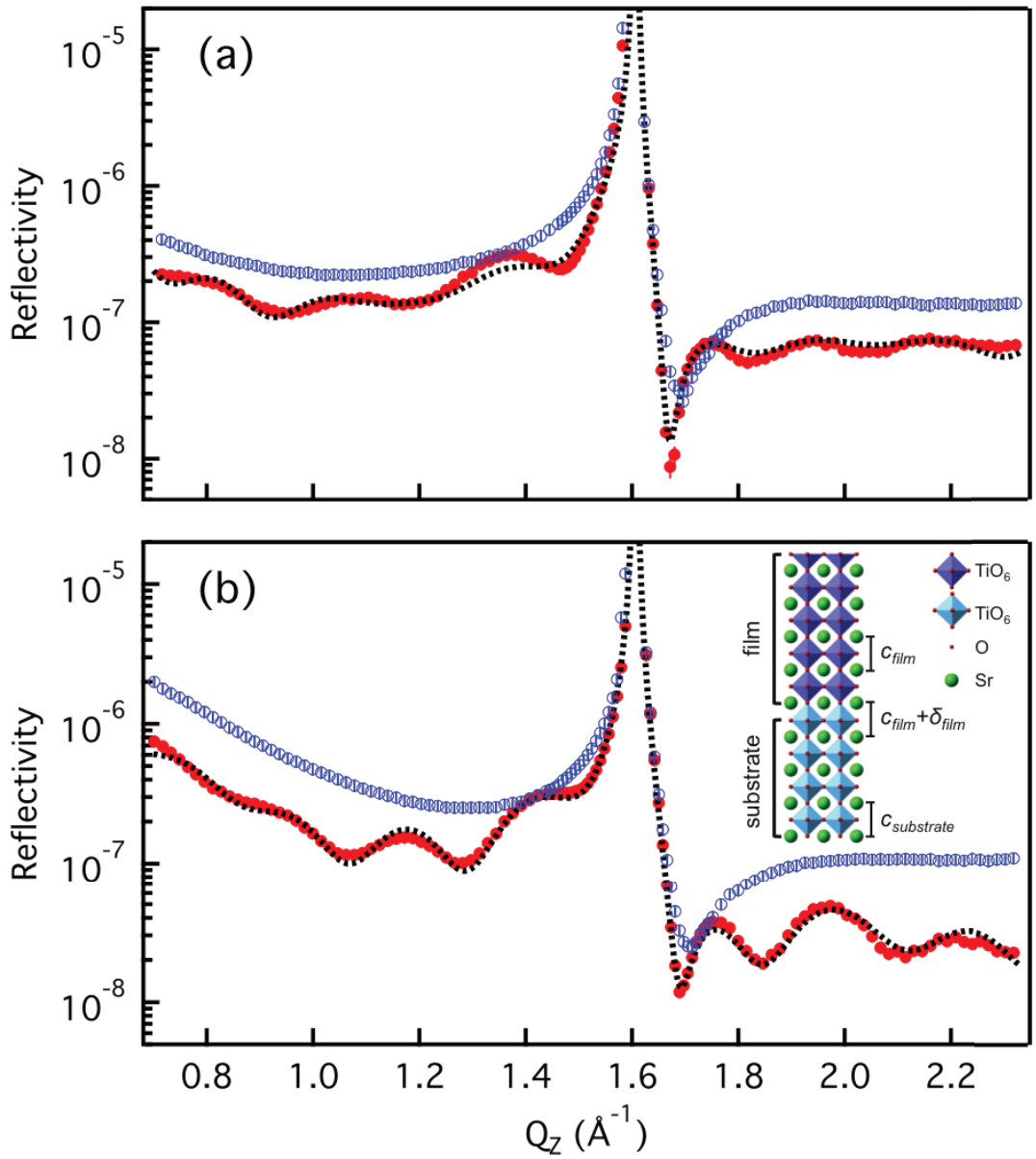

Figure 6.3. X-ray reflectivity data with error bar from bare $SrTiO_3$ substrate (blue circle), (a) codeposition and (b) shuttered deposition $SrTiO_3$ film (red dot), and fit (dotted line) for scattering along the (00L) specular CTR through the $Q_z = 1.606$ Å^{-1} (001) Bragg peaks of the $SrTiO_3$ substrate. Inset shows a schematic diagram of the atomic structure model for the fit.

were omitted from fitting because the analysis only considers scattering in the kinematical approximation [170, 86], and the fitting results are also in a good agreement with previous findings that Kiessig fringes, commonly observed even in stoichiometric homoepitaxial $SrTiO_3$ films, arise from a film/substrate interface offset [169].

6.2.3. Surface Diffuse X-ray Scattering

If in-homogeneities of the electron density such as islands are present on the surface, they scatter the incident, reflected and transmitted beams in a way that depends on

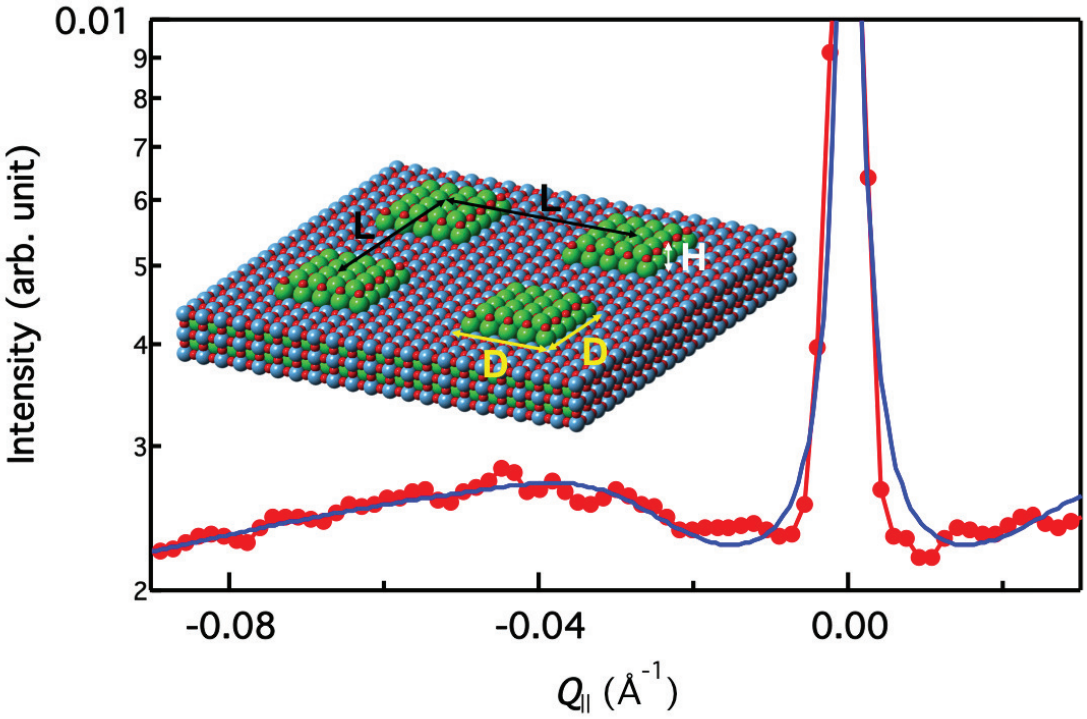

Figure 6.4. Scattering line shape at $t \approx 326$ s for shuttered growth and the best fit to a rapid analysis based on Grazing Incidence Small Angle X-ray Scattering (GISAXS) model discussed in the text. Average morphological parameters of the nanostructures: the inter-nanostructure distance L, the in-plane island size d and height H (inset).

their morphology and topography. To extract quantitative information, we analyzed our low-angle reflectivity data based on the well-known grazing incidence small angle X-ray scattering (GISAXS) model which is sensitive mainly to the morphological properties parallel with the surface (along $Q_{\parallel}$) and perpendicular to it (along Q_z) [171] is used to estimate the average morphological parameters of the nanostructures: the inter-nanostructure distance L, the in-plane island size d, and height H (as shown in the inset of Figure 6.4). In this analysis, the nanostructures are modeled by parallelepipeds without size distribution. These crude approximations are made for the sake of simplicity. The X-ray data were fit to

$$I_{fit}(Q_{\parallel}) = I_{bg} + I_0 F^2(Q_{\parallel}) S(Q_{\parallel}) \ , \tag{6.1}$$

where I_{bg} is a constant background, where I_0 is a scale factor, $F(Q_{\parallel})$ is the form factor (i.e., the amplitude of the Fourier transform) of a parallelepiped [171], and $S(Q_{\parallel})$ is the interference function calculated within the 2D-paracrystal theory assuming a square lattice [163], with the mean inter-nanostructure distance being L and the corresponding standard deviation σ. Figure 6.4 shows the single frames (time slice) from Figure 6.2(e) corresponding to $t \approx 326$ s: the frame right before closing the Sr shutter where the integrated diffuse scattering intensity is at its first maximum [Figure 6.2(f)]. Also shown are the results of the best fit with the resulting average morphological parameters of $L \approx 98$ Å, $D \approx 27.1$ Å, and $H \approx 4.2$ Å. Taking into account the difference in the electronic state of SrO in the A-site layer of $SrTiO_3$ from that in the rock salt $(SrO)_2$ layer, the obtained height (4.2 Å) can be presumed to correspond to the unit cell height (5 Å) of SrO rock salt on TiO_2-terminated $SrTiO_3$(001) [172]. Moreover, the result of the best fit (4.2 Å) is also very close to the theoretical prediction on the thickness of $(SrO)_2$ layer (4.3 Å) above

the TiO_2-terminated $SrTiO_3$(001) substrate. This results indicate the deposition of SrO grows as many small islands of two SrO atomic layers, which is in good agreement with the previous fitting results of X-ray scattered intensities along the (00L) CTR measured immediately following the shuttered deposition of nominally one SrO atomic layer at the growth temperature [57].

6.2.4. Energetics Driving Force for the Formation of Bilayer SrO Islands

Based on the predicted energetics (Figure 6.5), one expects that growth should proceed by the nucleation and coalescence of monolayer-high SrO islands, followed by the same for TiO_2. The data in Figure 6.2 and fits to the diffuse scatter, as shown in Figure 6.4, demonstrate that SrO does not wet the TiO_2-terminated surface but rather forms $\sim$ 2-ML-thick SrO_x islands with $\sim$ 10 nm inter-island spacing. The SrO_x islands then dynamically restructure into $SrTiO_3$ unit cells during the growth of the TiO_y to form an atomically flat layer.

To understand the energetic driving force for the formation of bilayer SrO islands, first-principles calculations were performed with density functional theory (DFT), as implemented in the *Vienna Ab initio Simulation Package* (VASP) [125, 143]. The PBEsol [122] functional is chosen, because of its excellence for the description of bulk $SrTiO_3$ [145]. The projector augmented wave method is used with the following potentials for $SrTiO_3$:O ($2s^2 2p^4$, E_{cut}=400.0 eV), Ti ($3p^6 3d^{10} 4s^2$, E_{cut}=274.6 eV) and Sr ($4s^2 4p^6 5s^2$,E_{cut}=229.3 eV). The plane-wave energy cutoff is set to 500 eV. The substrate is approximated with 20 atomic layers ($\sim$3.7 nm) of cubic $SrTiO_3$, with the bottom 10 atomic layers fixed to the optimized bulk positions and the other layers relaxed. To reduce the mirror interactions

between neighboring supercells, we add a vacuum slab as thick as 1.5 nm and consider dipole corrections in the out-of-plane direction. The supercells in the plane are one unit cell sizes large and the Monkhorst-Pack k-point grids for Brillouin zone sampling are $6 \times 6 \times 1$.

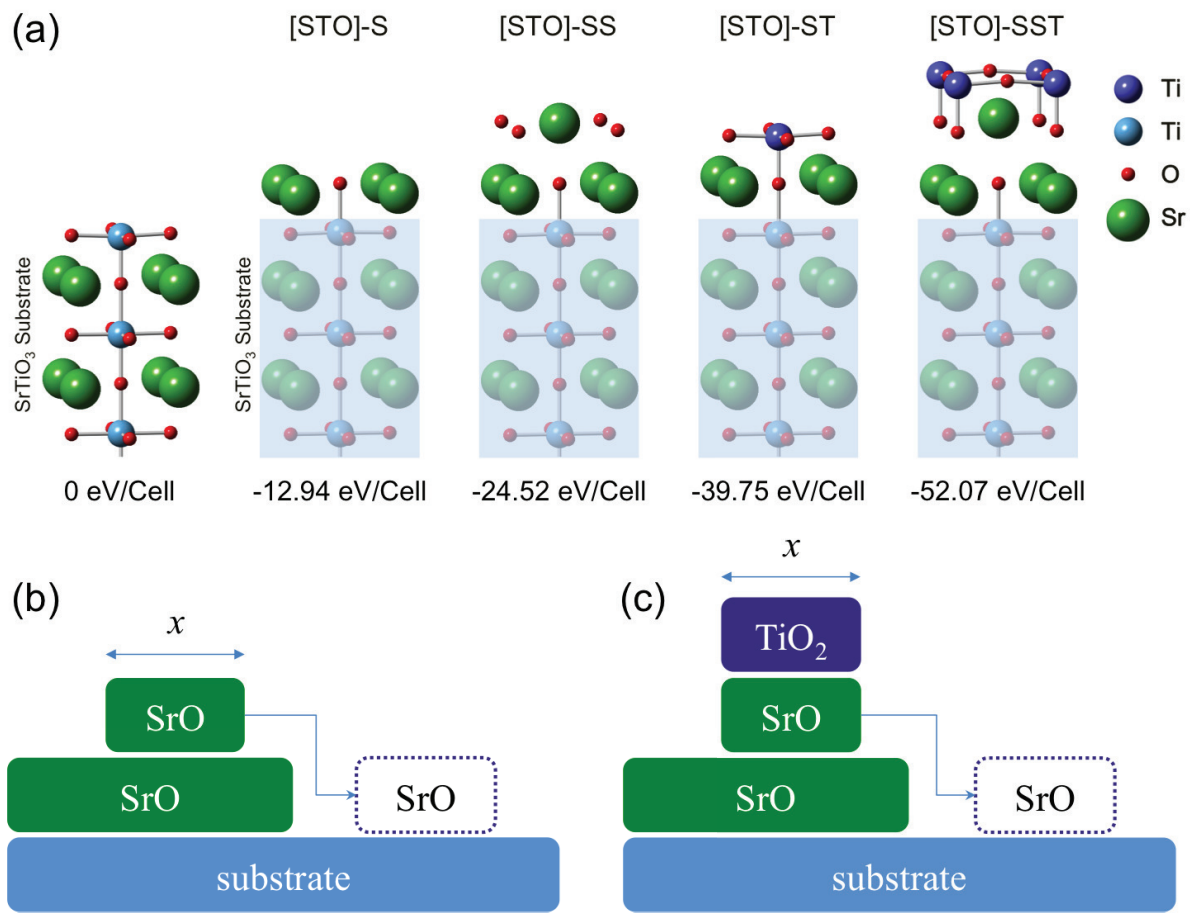

Figure 6.5. (a) Total energies per unit cell in $x-y$ plane of various stackings relative to the bare TiO_2-terminated substrate, where S, T, and [STO] represent the SrO plane, TiO_2 plane, and TiO_2-terminated $SrTiO_3$, respectively. (b) Schematic model of changing SrO bilayer island to single layer island. (c) Schematic model of smoothing the SrO bilayer island during the growth of TiO_2 layer. The boxes with dotted frames in panel (b) and (c) indicate the new positions of the SrO layer.

To identify the causes for the creation of SrO bilayer islands, we compare the energetics of SrO bilayer islands to a whole SrO layer. Figure 6.5(a) shows the energies of different stackings relative to the bare TiO_2-terminated substrate. Under the assumption that the edge effects is negligible relative to the total energy of island, the energy change from the SrO bilayer islands to a single layer [Figure 6.5(b)] equals—$12.94 \times 2x + 24.52x = -1.36x$ eV/Cell, where x is the area of the top SrO layer. Therefore, the formation of SrO islands is caused by kinetic processes even though the growth of one whole SrO layer is thermodynamically preferable. Consequently, one necessary condition of nucleation must be satisfied: the number of deposited atoms staying on the SrO monolayer island should be greater than two. Figure 6.6 shows the schematic energy landscape of a particle on a SrO monolayer island, where the diffusion barrier on the layer is E_d and the Ehrlich-Schwoebel barrier is E_e. If we assume that the particles are independent and the energy landscape has the C_∞ symmetry in $x - y$ plane, then an analytic expression can be readily obtained.

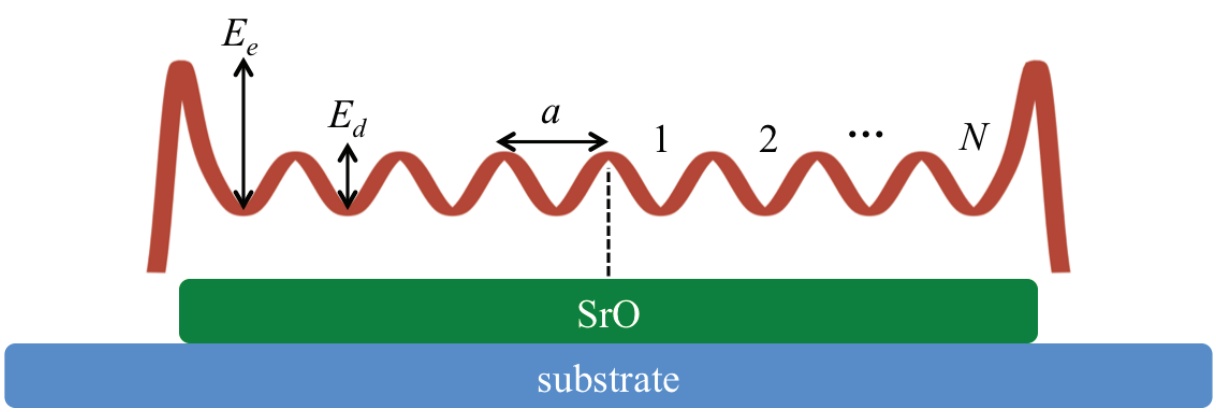

Figure 6.6. A simplified model and energy landscape (red curve) to estimate the particles staying on a SrO monolayer island. The substrate is TiO_2-terminated. The valleys, where the particles majorly reside, are numbered. The diffusion barrier E_d, Ehrlich-Schwoebel barrier E_e, and the distance of each jump, a, are labeled.

In a steady state, the particle flux though the energy peak between valley n and $n+1$ equals both the new deposited particles in the area $\pi(na)^2$ and the net atoms jumping from valley n and $n+1$, as expressed in Equation 6.2.

$$\begin{aligned} \pi(na)^2 f &= \left(\tfrac{1}{2}C_n - \tfrac{1}{2}C_{n+1}\right)\gamma e^{-E_d/(k_B T)}\ , \qquad \text{if } 1 \le n \le N-1 \\ \pi(Na)^2 f &= \tfrac{1}{2}C_N \gamma e^{-E_e/(k_B T)} \end{aligned} \tag{6.2}$$

Wherein f, C_n, and γ are the deposition flux ratio, the number of particles in the valley n, and the attempt frequency, respectively. Therefore, the total number of particles on the island can be obtained with Equation 6.3.

$$\sum_{n=1}^{N} C_n = \frac{\pi a^2 f}{\gamma e^{-E_d/(k_B T)}} \frac{N^2(N-1)^2}{2} + \frac{2\pi a^2 f}{\gamma e^{-E_e/(k_B T)}} N^3 \tag{6.3}$$

Interestingly, because the first part over the second part equals: $e^{-(E_e - E_d)/(k_B T)N/4}$, the edge-cross barrier E_e dominates Equation 6.3 at $E_e - E_d \gg k_B T$ and the diffusions apart from the edge becomes unimportant. DFT calculations indicate that the barrier E_d of the major species, Sr atom, is 0.83 eV, and the barrier E_e crossing a SrO [100] edge is 0.56 eV. If the [100] edge is attached with an extra line of Sr atoms, the barrier is increased to 0.89 eV. With the parameters $f = 6 \times 10^{-4}$ atoms/(Å^{2}sec), $a = 3.89$ Å, and $\gamma \approx 1012$ sec^{-1}, the respective critical size N_c at $\sum_{n=1}^{N_c} C_n > 2$ for the edge with and without the extra Sr atoms are found to be ~ 325 and ~ 327, which are much greater than the experiment island size range. Figure 6.7 shows the necessary barrier E_e for different critical island size N_c. One can find that in the experimental island size range, E_e needs to be 2.23 eV. The discrepancy could be ascribed to several aspects. First, the independent particle assumption underestimates the probability nucleation and thus overestimates N_c. Second,

the edge structure could be different from what assumed, which may increases E_e even more. Third, the possible defects, like vacancies, in the island may trap the adatoms and play the role of nucleus.

To find out the causes of smoothing the SrO bilayer islands during the deposition of TiO_2, we calculate the energy change of moving the top layer of the bilayer island to the substrate and putting a TiO_2 layer above the exposed SrO monolayer island, as shown in Figure 6.5(c). It turns out that the energy change of this process is $-39.75x - 12.94x + 52.07x = -0.62x$ eV/Cell, which indicates that the smoothing of SrO bilayer islands is energetically favorable.

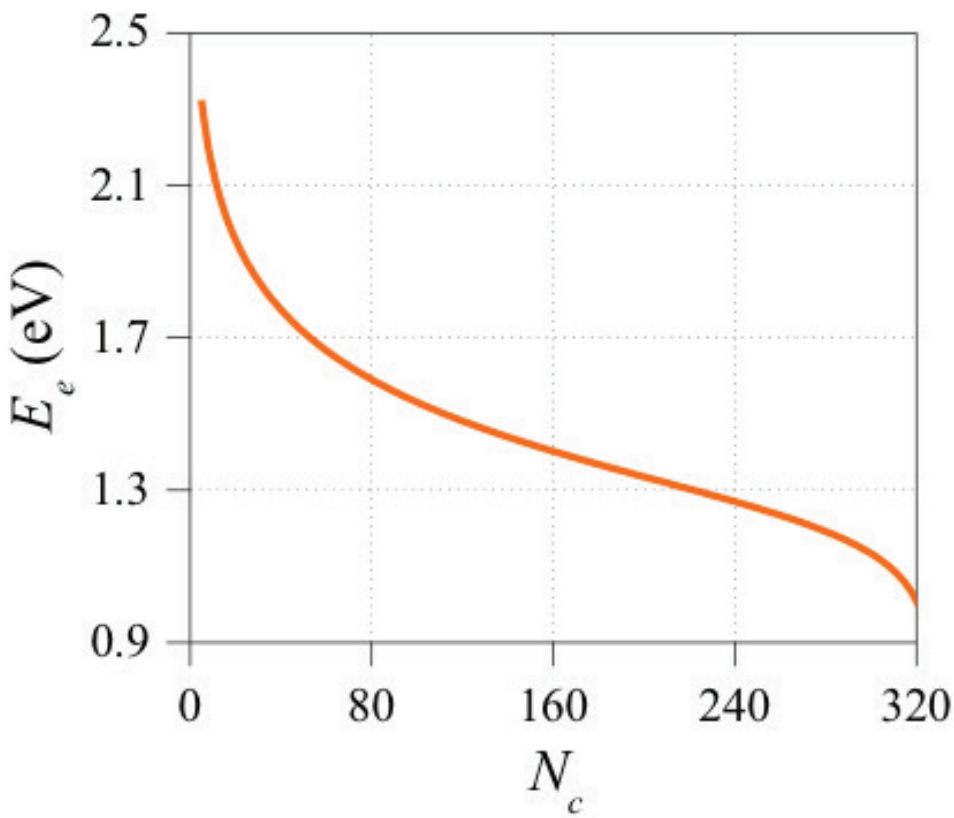

Figure 6.7. Relationship between the critical island size N_c and Ehrlich-Schwoebel barrier E_e for Sr atom based on Equation 6.3 and the parameters in the text.

Kinetically, the smoothing process could happen by the insertion of Ti/TiO_2 into the top SrO layer, which kicks out SrO molecules of the SrO layer, and the consequent diffusion of the kicked-out SrO to the substrate [57].

6.2.5. Time-resolved Diffuse X-ray Scattering Studies for Shuttered Deposition Performed in the Wrong Order

Finally, we note interesting diffuse scatter behavior when sequential deposition was performed in the wrong order, i.e., with TiO_y first deposited onto the TiO_2-terminated substrate, followed by SrO_x (i.e., TiO_y/SrO_x). As shown in Figure Figure 6.8, the initial growth of TiO_y leads to a drop in the specular intensity; however, the diffuse intensity appears to rise to a maximum at 1/2 ML coverage, returning to a minimum before the Sr shutter is open: this is what is expected for 2D island growth of 1-ML-thick TiO_2 islands (i.e., TiO_y appears to wet the TiO_2-terminated substrate). Interestingly, the same behavior occurs for the SrO_x deposition: the diffuse intensity peaks at roughly 1/2 ML coverage and smooths as the film restructures to for $SrTiO_3$, but with SrO now below the TiO_2 layer; this layer rearrangement mechanism may be similar to that observed earlier for the Ruddlesden-Popper series [57]. The second through fifth TiO_y/SrO_x cycles behave differently: the diffuse scatter continues to increase with TiO_y deposition, decreasing substantially only after the Sr shutter is open. Thus, it appears TiO_y does not wet the (TiO_2) film surface, at least with this growth rate (the rate of rise in diffuse scatter appears to decrease near the end of the TiO_y growth cycle, suggesting that the TiO_y bilayers are slowly changing to monolayers). As seen in Figure 6.8(b), the final film structure is

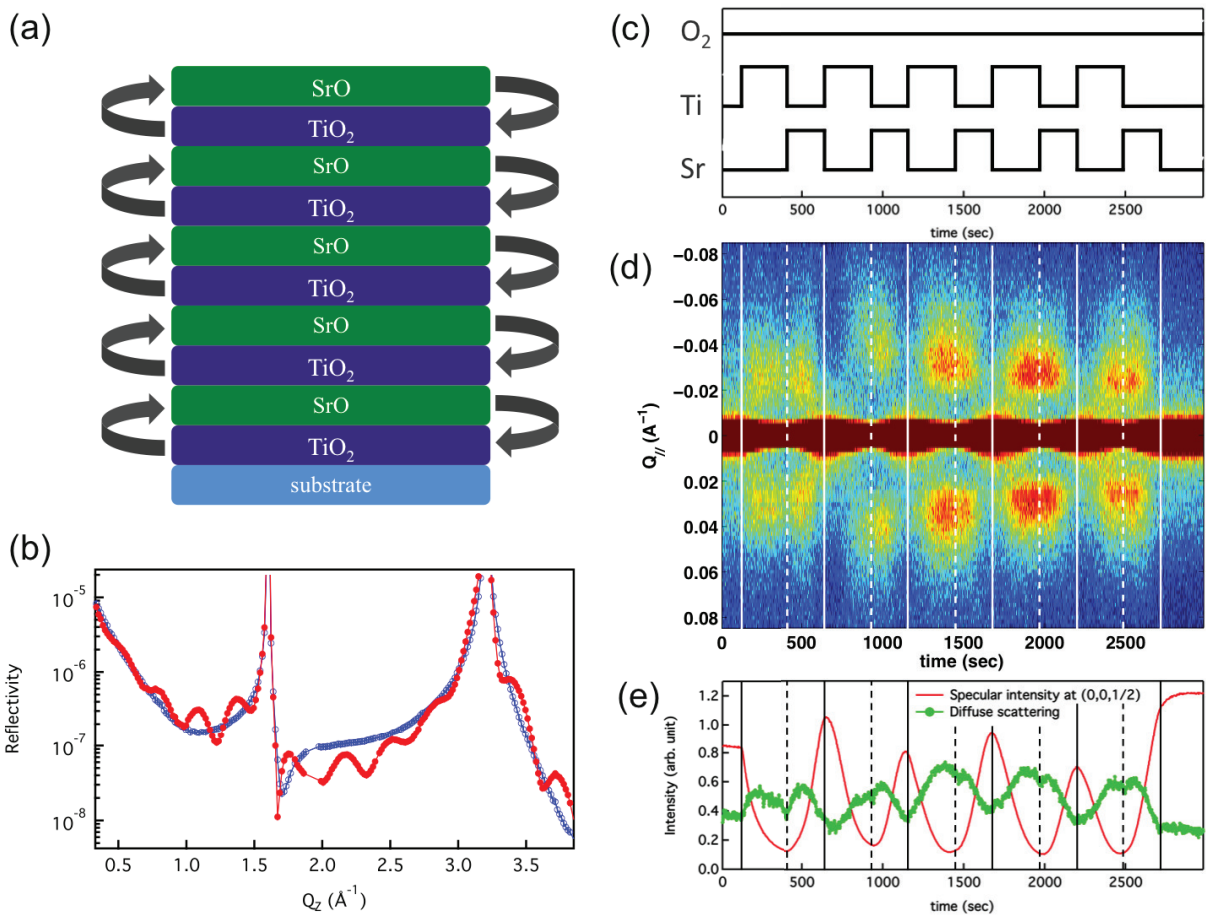

Figure 6.8. (a) A schematic diagram of the expected atomic structure of five unit cells of $SrTiO_3$ with growth sequence of TiO_2 and SrO and proposed layer swap that occurs in the real growth. (b) X-ray reflectivity data with error bar from bare $SrTiO_3$ substrate (blue circle) and shuttered-deposited $SrTiO_3$ film (red dot) with growth sequence of TiO_2 and SrO for scattering along the (00L) specular CTR through the $Q_z = 1.606$ Å^{-1} (001) Bragg peaks of the $SrTiO_3$ substrate. (c) Timing diagram of the sequential deposition of strontium and titanium during the shuttered deposition of five unit cells of $SrTiO_3$ with sequence of TiO_2 and SrO. Oxygen is provided continuously during the growths. Time-resolved diffuse X-ray scattering data shown in (d) false color image and (e) the corresponding integrated diffuse and specular intensity during $SrTiO_3$ homoepitaxy by shuttered deposition in the wrong order.

nearly identical to that for the SrO_x/TiO_y, demonstrating that layer rearrangement indeed occurred.

6.3. Summary

In conclusion, these results illustrate some of the challenges faced by thin film growth specialists and underscore the importance of gaining detailed and quantitative knowledge of the atomic-scale processes occurring in situ as these materials are grown. It provides a new path toward the realization of high-quality, single crystal films of complex oxides. In addition, it shows that the hope of building artificial new layered materials by stacking up deposited monolayers [132] must be reevaluated in view of the thermodynamical driving forces present at the high temperatures prevalent during growth.

CHAPTER 7

Effect of Polar Discontinuity on the Growth of Epitaxial $LaNiO_3$ Ultrathin Films

Overview

In an effort to scale down electronic devices to atomic dimensions, the use of transition-metal oxides may provide advantages over conventional semiconductors. Nevertheless, understanding how their correlated electronic states can be manipulated at the nanoscale remains challenging. Here, we have conducted a detailed microscopic study of epitaxial correlated metal $LaNiO_3$ ultrathin films grown on band insulator $SrTiO_3$ (001) as a function of thickness by using reactive molecular-beam epitaxy with *in situ* surface X-ray diffraction and *ex situ* soft X-ray absorption spectroscopy to explore the influence of polar mismatch on the resulting structural and electronic properties. In general, metallic $LaNiO_3$ films can effectively screen this polarity mismatch, but in the ultrathin limit, we have discovered that films are insulating and require additional chemical and structural reconstruction to compensate for such mismatch. Our data demonstrate that the initial layers on the nonpolar $SrTiO_3$ surface exhibit a smaller than expected out-of-plane lattice-spacing with a Ni valence of 2+ which indicates the formation of a new chemical phase $LaNiO_{2.5}$ (Ni^{2+}) for a few unit-cell thick films. As the film becomes thicker, the lattice constant expands to its elastic limit, and the Ni valence approaches 3+. We have discovered that

atomic reconstruction occurs at the heterointerfaces between $LaNiO_3$ thin-films and $SrTiO_3$ (001) substrates, which effectively alleviates the polarity conflict without destroying the heteroepitaxy. Our result demonstrates one of the important ways to create artificial heterostructures between polar and nonpolar complex oxides. We have demonstrated the power of artificial confinement to harness control over competing phases in complex oxides with atomic-scale precision.

7.1. Introduction

Correlated transition-metal oxides host a diverse array of electronic and magnetic properties, including high-temperature superconductivity, colossal magnetoresistance, ferroelectricity and Mott metalinsulator transitions (MITs) [17]. Functional materials based on correlated transition-metal oxides in thin film form offer new and exciting strategies for meeting many of our outstanding energy challenges [22]. The atomic-level synthesis of functional oxides and an understanding of their growth behavior provide opportunities to explore and control the intriguing properties of artificial oxide heterostructures [23, 12, 50]. Unfortunately, synthesis of such oxide films can be a major challenge even when utilizing reactive molecular-beam epitaxy (MBE), the most precise and powerful deposition technique that is often regarded to allow the construction of materials atomic plane by atomic plane which is uniquely suited to the deposition of layered oxide materials that cannot be stabilized in bulk form [130, 131, 27].

The polarity of materials and their electrostatic boundary conditions are key factors to create unprecedented electronic and magnetic properties in complex-oxide heterostructures. For example, the discontinuous polarity at the heterointerface between polar $LaAlO_3$ (LAO) and nonpolar $SrTiO_3$ (STO) [38] has resulted in confined electrons at the interface to form a two-dimensional electron gas (2DEG) [173], which exhibits intriguing properties such as metal-insulator transitions [174], colossal capacitance [175], and the coexistence of superconductivity [176] and magnetism [177]. Though the actual physical process that prevents the electric potential from diverging within the polar layer and results in this metallic behavior is still under debate, it has been unanimously concluded that the polar mismatch at the LAO/STO interface is responsible for this emergent metallic state [38].

In bulk $LaNiO_3$ (LNO), Ni is in the low-spin $3d7$ configuration with an unusual high 3+ oxidation state and is metallic, and it remains paramagnetic down to low temperature. Ultra-thin films of $LaNiO_3$ grown along the moderately polar (001) direction have been extensively investigated recently. However, it has been reported that experimentally realized LNO films and LNO/LAO superlattices on STO (001) revealed an unexpected transition to the Mott insulating with decreasing LNO thickness [178, 20, 179]. Additionally, it was established that growth of the properly stoichiometric $[LNO]_{1u.c.}/[LAO]_{1u.c.}$ (u.c=unit cell) superlattices on STO (001) requires an extra buffer layer of 1 u.c. LAO to compensate for the polar mismatch. Resonant x-ray absorption on Ni $L_{3,2}$-edge confirmed the presence of Ni^{2+} in the initial LNO layer [102].

Since the polar mismatch can have a significant effect on the initial nucleation, film growth [39] and overall material properties which is particularly crucial for ultra-thin films, the mechanism of how the polar discontinuity is compensated in real materials is with great interest towards the experimental realization of new materials with novel properties. To address this issue, we have investigated the heterointerfaces of polar LNO and nonpolar STO along the pseudo-cubic [001] direction as a model system. Here is the schematic of ionic arrangement of (001) planes in LNO/STO interface. The nominal charge density of a LaO plane is +1 because the nominal charge of the La ion is +3 and that of oxygen is -2. Similarly, the nominal charge density of a NiO_2 plane is -1 because the nominal charge of the Ni ion is +3 and that of oxygen is -2. As a result, LNO forms alternating +1e, -1e charged planes stacked along this direction, leading to polarity mismatch at the interface (Figure 7.1).

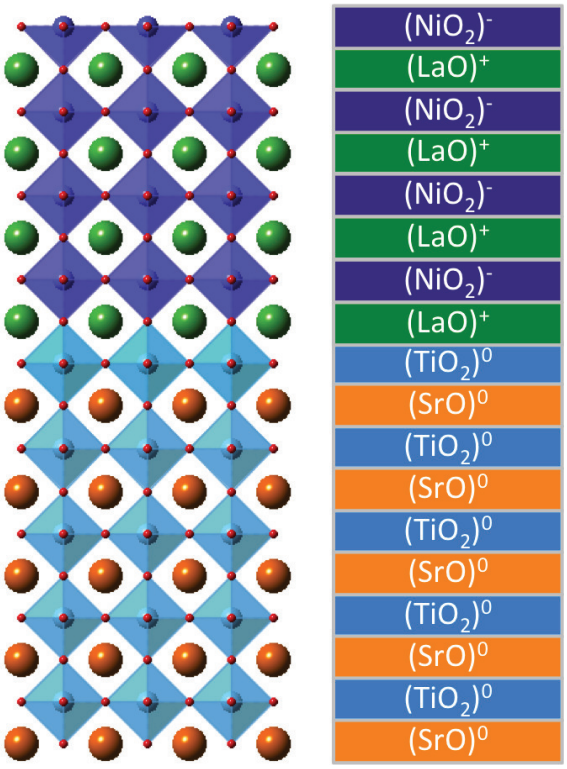

Figure 7.1. Schematic diagrams of the configurations of $LaNiO_3/SrTiO_3$ heterointerface. Along the (001) direction, $SrTiO_3$ (: SrO, TiO_2) is nonpolar while $LaNiO_3$ (: $[LaO]^{1+}$ $[NiO_2]^{1-}$) is polar.

In this chapter, we tried to understand the effect of the polar discontinuity on the growth of epitaxial LNO ultrathin films by using our newly constructed oxide MBE chamber with synchrotron radiation capability, built from an existing *in situ* X-ray chamber at beamline 33-ID-E of the Advanced Photon Source (APS) [65]. Here, we make use of reactive MBE to synthesize atomically defined layers of the correlated metal LNO down to just four pseudocubic unit cell (u.c.) thickness, epitaxially stabilized on STO (001) substrates. Combining *in situ* surface X-ray diffraction (SXRD) with ex situ soft X-ray absorption spectroscopy and electrical transport measurements, we uncover an instability towards an insulating ordered phase that abruptly onsets at 4 u.c. We use soft X-ray absorption

spectroscopy to directly track how the changes of electronic structure and charge state of Ni evolve through the thickness-driven MIT, shedding new light on how phase competition can be manipulated at the nanoscale by building up correlated quantum materials, one atomic layer at a time. The *in situ* surface X-ray diffraction measurements were performed using a monochromatic 15 keV X-ray beam and a custom reactive MBE/X-ray diffraction system installed in the 33-ID-E hutch at the Advanced Photon Source (APS). Soft X-ray absorption spectra were taken at room temperature at the 4-ID-C beamline of APS.

7.2. Experimental Results and Discussions

The LNO films were grown at 590 °C and in a background pressure of 8×10^{-6} Torr of 10% ozone, using La and Ni effusion cells. Both sources were shuttered to deposit alternating monolayer doses of LaO and NiO_2. Shutter times were initially set based on flux measurements made using a quartz crystal microbalance (QCM) located directly in front of the substrate, and then precisely tuned by optimizing Kiessig (thickness) fringes with high resolution X-ray reflection measurement on a calibration sample immediately prior to the growth of the sample sets. Before growth, STO substrates were prepared using a termination recipe to achieve a TiO_2-terminated surface [58].

7.2.1. High-resolution X-ray Reflectivity

To gain further insight into the structural quality and the chemical phase obtained during the initial growth sequence, high-resolution X-ray reflectivity has been recorded along the out-of-plane direction (00L) crystal truncation rod (CTR) Immediately following the deposition of 2nd, 4th, and 10th u.c. during the growth of a 10-unit-cell-thick LNO films

on STO (001) substrates (Figure 7.2). Data points near the sharp STO Bragg peaks were omitted for clarity. It can be readily observed that the film peak position gradually shifts toward lower L as the film thickness increasing from 2 u.c. toward 10 u.c. film during the growth which means the out-of-plane lattice constant increased toward stoichiometric LNO as the film thickness increased. The gradual shifting of the film peak could be originated from some oxygen deficient perovskites with formulae $La_nNi_nO_{3n-1}$ [180]. At the same time, the overall enhancement of electrical conductivity with increase in film thickness acts to reduce the polar catastrophe by partial metallic screening. Thus some of the oxygen

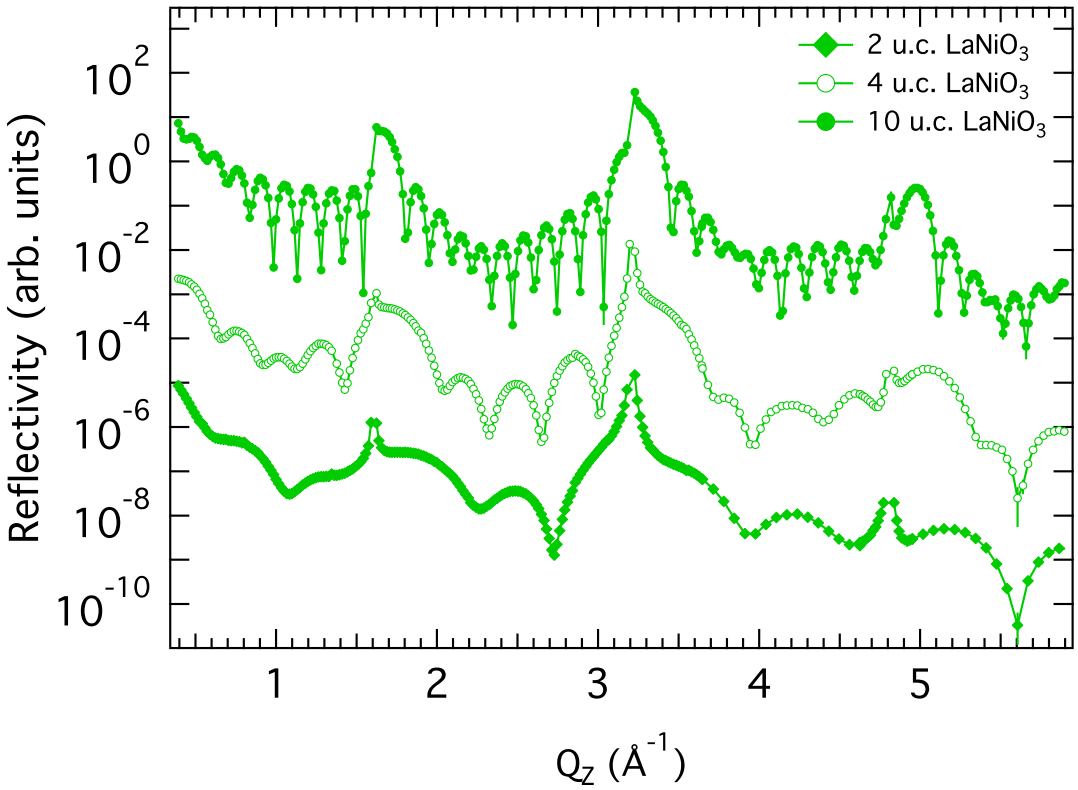

Figure 7.2. Scattered intensities along the $00L$ measured immediately after shuttered growth of 2nd, 4th, and 10th unit cell.

vacancies in $LaNiO_{2.5}$ phase [181] (formed during the first 4 u.c. growth) can be further effectively compensated by forming the $LaNiO_{2.5+\delta}$ phase as film thickness increased. This results in gradual shift of the LNO film peak position towards the stoichiometric LNO as shown in Figure 7.2. We can also conjecture, that when the metallic screening is sufficiently strong, the oxygen deficiencies are almost entirely compensated as confirmed by the LNO film peak position for 10-unit-cell-thick film.

To clarify the origin of these phenomena, a series of epitaxial ultra-thin LNO films of different thickness (ranging from 4–10 u.c.) have been grown on nonpolar STO (001)

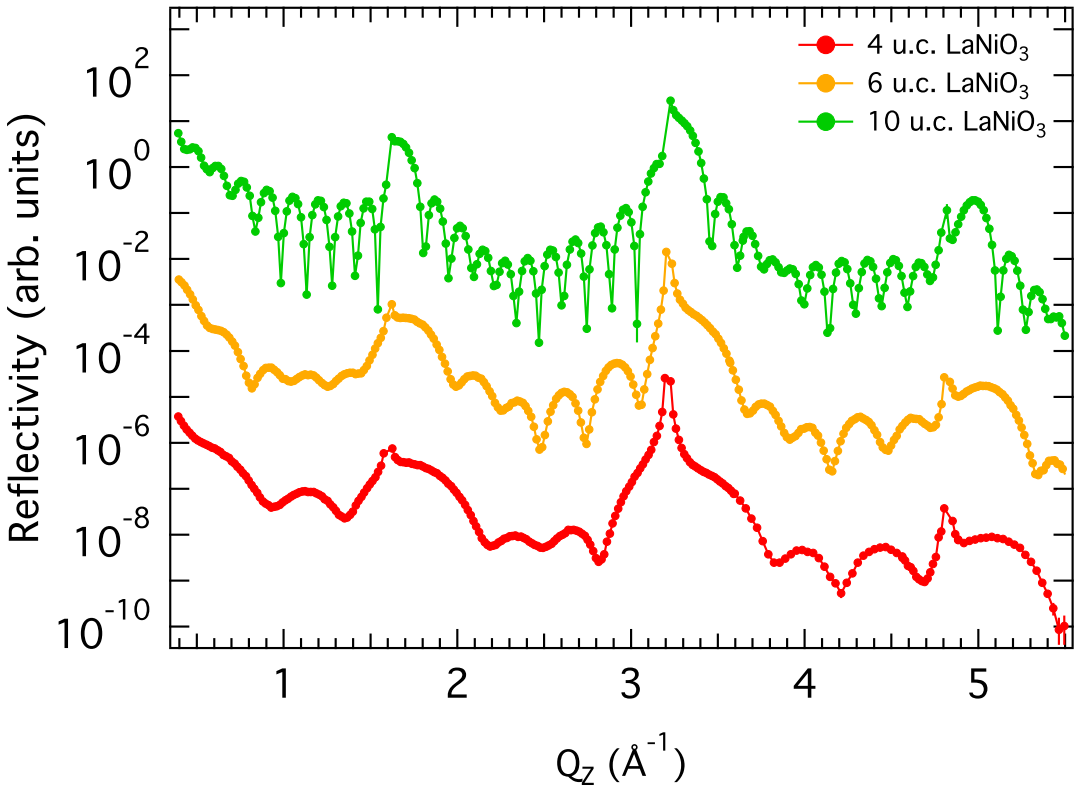

Figure 7.3. Scattered intensities along the $00L$ measured immediately after growth of 4 u.c., 6 u.c., and 10 u.c. films.

substrates, and high-resolution X-ray reflectivity has been recorded along the out-of-plane direction (00L) crystal truncation rod (CTR) under growth conditions immediately following the deposition. The X-ray results are shown in Figure 7.3, and the film peak position gradually shifts toward lower Q_z as the film thickness increasing from 4 u.c. to 10 u.c. films. Therefore, it shows the out-of-plane lattice constant increased toward stoichiometric LNO as the film thickness increased as the *in situ* measurement shown in Figure 7.2.

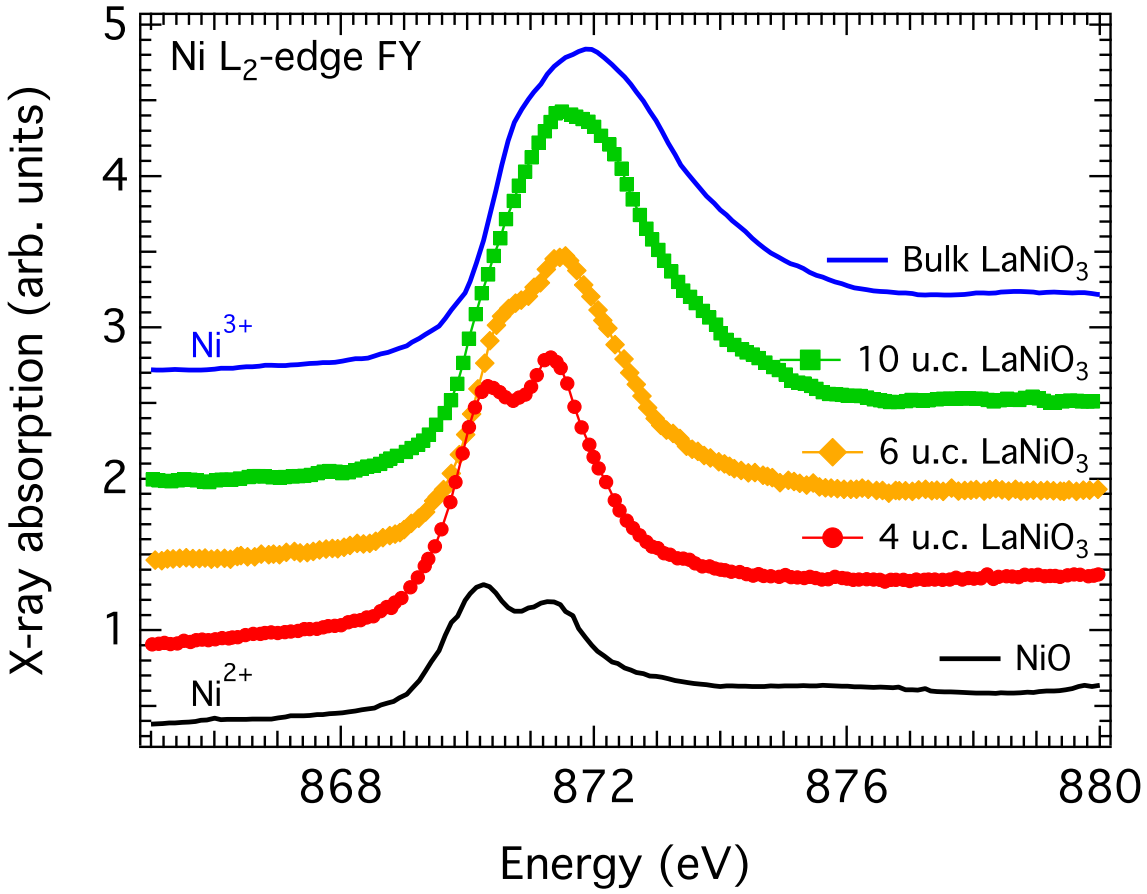

Figure 7.4. X-ray absorption spectroscopy. Ni L_2-edge XAS spectra from $LaNiO_3$ films on $SrTiO_3$ (001) with different thickness recorded in TFY mode at 300 K.

7.2.2. Resonant X-ray absorption

As shown in Figure 7.4, resonant X-ray absorption was performed on Ni L_2-edge in the bulk-sensitive fluoresce yield mode to tracked the changes of electronic structure and charge state of Ni as a function of the LNO thickness. A comparison of the line-shape and the L_2 energy position (i.e. chemical shift) for the LNO films to the well known Ni^{2+} material NiO and N^{3+} bulk LNO sample indicates that Ni ions are indeed closed to the +2 oxidation state for thinner films and increases the relative weight of Ni^{3+} ions progressively increases with the film thickness. From the chemistry perspective, the presence of oxygen vacancies should alter the Ni^{3+} charge state. Therefore, we think oxygen vacancies are formed at the interface to compensate for the polar mismatch in the initial growth of LNO. As the thickness increases, the enhancement of electrical conductivity with film thickness partially screens the interfacial field, resulting gradual compensation of oxygen vacancies.

7.2.3. Transport properties.

Finally, we turn our attention to the question of how electrical properties of ultra-thin LNO films are affected by the polar mismatch at the heterointerface. As shown in Figure 5, 10-unit-cell-thick LNO film shows bulk-like metallic behavior down to low temperature. However, as the film thickness decreases, the resistivity increases. As illustrated in Figure 7.5, 6-unit-cell-thick LNO film exhibits insulating (semiconducting) behavior starting from room temperature, and 4-unit-cell-thick LNO film becomes highly insulating with about 2 order of magnitude higher than 6-unit-cell-thick film which showing the development of a new electronic ground state of the material. While this metal-insulator transition as a function of film thickness could be linked to the effect of

reduced dimensionality but not for the highly insulating 4-unit-cell-thick film which we think it can be explained by the presence of a highly insulating $LaNiO_{2.5}$ phase because oxygen vacancies are formed at the interface to compensated for the polar mismatch in the initial growth of LNO [182, 183]. As the film thickness increases, the enhancement of electrical conductivity with film thickness partially screens the interfacial field, resulting gradual compensation of oxygen vacancies. Therefore, the oxygen deficiencies are almost entirely compensated in thicker films when the metallic screening is sufficiently strong.

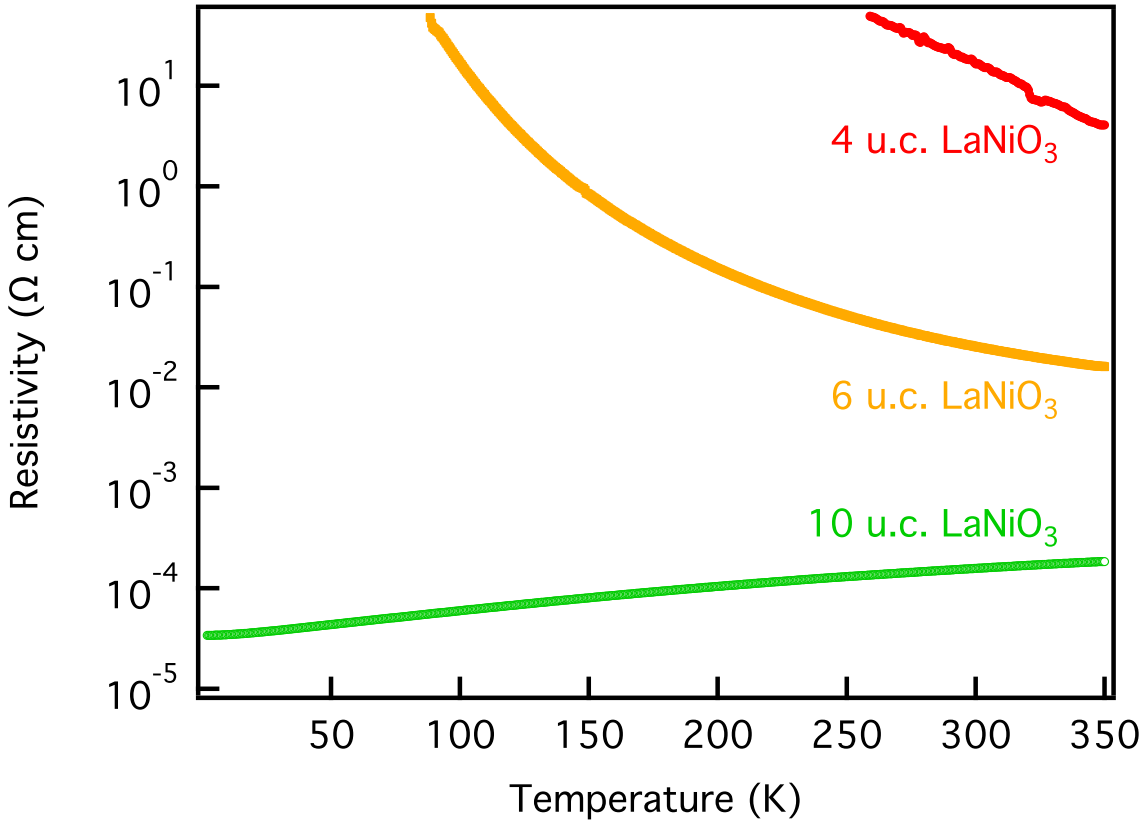

Figure 7.5. Transport properties. Resistivity as a function of temperature for $LaNiO_3$ films on $SrTiO_3$ (001) with different thickness.

7.3. Summary

In conclusion, we observed the process of the polar discontinuity effect on the growth of epitaxial LNO Ultrathin Films on STO (001). A series of epitaxial ultra-thin LNO films of different thickness (ranging from 4–10 uc) have been grown on non-polar STO (001) substrates and the process of the polar discontinuity effect at the perovskite interface has been observed. A combination of *in situ* SXRD recorded during the growth of each consecutive unit cell, ex situ transport and synchrotron based resonant X-ray spectroscopy at Ni L-edge reveal the formation of polarity stabilized new chemical phase $LaNiO_{2.5}$ (Ni^{2+}) for a few unit-cell thick films. A gradual increase of metallicity with increasing thickness serves as an additional mechanism to screen the diverging potential, leading to a sharp decrease of oxygen vacancies for thicker films and restoring nominal 3+ charge state of Ni.

CHAPTER 8

Summary and future work

8.1. Thesis summary

This work is focused on complex oxide materials, an area with immense scientific richness and outstanding potential for meeting many of our technological demands. The central goal of my work is to understand the structural and electronic behavior of ultrathin complex oxides films subjected to confinement, lattice misfit and broken symmetry at the interface. This includes the growth of complex oxides utilizing both computational studies of synthesis and an oxide molecular beam epitaxy (MBE) system with *in situ* X-ray scattering capability. The *in situ* oxide MBE system will be the first of its kind and will allow an unprecedented level of control over both stoichiometry and structure; moreover, the associated computational studies are expected to significantly advance both the materials science of growth and understanding of complex oxide phenomena.

In ultrathin films of complex oxides, strain fields at the thin film-substrate interface directly tune the local electronic states of the correlated transition metal d orbitals, from which novel functionalities and phases prohibited in bulk phases are stabilized [**18**, **19**]. We have experimentally demonstrated that the bulk crystal symmetry directs the atomic and orbital responses adopted by coherently strained $RNiO_3$ (R = La, Nd) ultrathin films. Detailed X-ray scattering and polarization-dependent X-ray absorption spectroscopy have been performed at beamlines 33-BM-C, 5-BM-D, and 4-ID-C of the Advanced Photon

Source (APS) at Argonne National Laboratory, respectively. A mathematical point group symmetry analysis of the epitaxial stabilized crystal by our collaborator James Rondinelli (Drexel University) reveals that the preferred orbital configuration adopted by the thin film is the one that stays closest to the bulk configuration, suggesting the strain-stabilized phases maintain a "memory" of their bulk state [56].

The atomic-level synthesis of functional oxides and an understanding of their growth behavior provide opportunities to explore and control the intriguing properties of artificial layered oxide heterostructures [26]. Unfortunately, synthesis of such oxide films can be a major challenge even when utilizing reactive MBE, the most precise and powerful deposition technique that is often regarded to allow the construction of materials atomic plane by atomic plane, which is uniquely suited to the deposition of layered oxide materials that cannot be stabilized in bulk form [27]. The main limitation being the lack of a rational framework to guide the process, researchers have been constrained in their ability to synthesize such layered oxide materials because of their limited control over composition and structure during deposition. Despite decades of study, a complete description of the fundamental mechanisms of oxide growth by reactive MBE is still a challenging problem.

Although there are several metal and semiconductor MBE systems worldwide with *in situ* synchrotron capabilities [184, 185, 65], for complex oxide synthesis, only a few groups have installed systems for *in situ* synchrotron studies using pulsed laser deposition (PLD) [186] and metal organic chemical vapor deposition (MOCVD) [187]. To-date, however, none of the facilities have pursued in situ oxide MBE, which is mandatory for the synthesis of layered complex oxide materials. To understand the fundamental physics of oxide growth by reactive MBE, we have upgraded an existing chamber at sector 33-ID-E

station of the APS to construct the worlds first oxide MBE system with in-situ synchrotron X-ray scattering capability and taken initial steps into both understanding the synthesis of complex oxides and achieving the desired compositional and structural control during growth by oxide MBE.

A longstanding challenge in the oxide thin film community has been the growth of $(AO)(ABO_3)_n$ Ruddlesden-Popper (RP) compounds [133]. We have utilized the *in situ* synchrotron oxide MBE to study the initial growth of the Sr_2TiO_4 phase on $SrTiO_3$ and track the dynamic evolution. To understand pathways to the growth of layered oxides, layer re-arrangement is studied by combing experiment and theory calculations done by the group led by Dane Morgan (University of Wisconsin). Theoretical calculations indicate that rearrangement can occur in many layered oxide systems and suggest a general approach that may be essential for the construction of metastable RP phases. In pursuit of growth of polar RP phases, we demonstrated the utility of the newfound growth strategy by synthesizing the first known sample of single crystalline $La_3Ni_2O_7$ thin film [57].

In addition, we have completed the first to date study of *in situ* homoepitaxial MBE growth of $SrTiO_3$, which compares shuttered deposition vs. codeposition of the constituents. The addition of *in situ* surface X-ray scattering during growth is expected to result in profound insight into our understanding of complex oxide growth. The typical *in situ* diagnostic tool for oxide MBE is reflection high energy electron diffraction (RHEED), which is an excellent growth monitor but is unable to provide the quantitative structural and compositional information that can obtain with x-rays. Since our chamber will have both in situ RHEED and X-ray capabilities, we will be able to aid other researchers in understanding their observed RHEED behavior.

Finally, in an effort to scale down electronic devices to atomic dimensions, the use of transition-metal oxides may provide advantages over conventional semiconductors. Nevertheless, understanding how their correlated electronic states can be manipulated at the nanoscale remains challenging. We have conducted a detailed microscopic study of epitaxial correlated metal $LaNiO_3$ ultrathin films grown on band insulator $SrTiO_3$ (001) as a function of thickness by using reactive molecular-beam epitaxy with *in situ* surface X-ray diffraction and *ex situ* soft X-ray absorption spectroscopy to explore the influence of polar mismatch on the resulting structural and electronic properties. Our result demonstrates one of the important ways to create artificial heterostructures between polar and nonpolar complex oxides. We have demonstrated the power of artificial confinement to harness control over competing phases in complex oxides with atomic-scale precision.

8.2. Future work

This work represents the first steps in developing a general understanding of the growth mechanisms of complex oxides and how they are influenced by properties, such as cation valence and surface polarity. Moreover, *in situ* growth studies can provide a wealth of information on not only the layer-by-layer structure but also the growth dynamics. In the future, the reactive MBE system developed at sector 33 will allow us to pursue *in situ* synchrotron studies of hybrid oxide MBE [166] to vastly improve control over stoichiometry and structure by enlarging the optimal process window for the search of novel functional complex oxides. Ultimately, these highly unique instruments will enable the necessary feedback between the design of new materials for enhanced functionality and materials synthesis.

References

[1] J. B. Goodenough. Electronic and ionic transport properties and other physical aspects of perovskites. *Rep. Prog. Phys.*, 67(11):1915–1993, 2004.

[2] William D. Nix. Mechanical Properties of Thin Films. *Metall. Trans. A*, 20A(11):2217–2245, 1989.

[3] J. H. Haeni, P. Irvin, W. Chang, R. Uecker, P. Reiche, Y. L. Li, S. Choudhury, W. Tian, M. E. Hawley, B. Craigo, A. K. Tagantsev, X. Q. Pan, S. K. Streiffer, L. Q. Chen, S. W. Kirchoefer, J. Levy, and D. G. Schlom. Room-temperature ferroelectricity in strained $SrTiO_3$. *Nature*, 430(7001):758–761, 2004.

[4] K. J. Choi, M. Biegalski, Y. L. Li, A. Sharan, J. Schubert, R. Uecker, P. Reiche, Y. B. Chen, X. Q. Pan, V. Gopalan, L.-Q. Chen, D. G. Schlom, and C. B. Eom. Enhancement of Ferroelectricity in Strained $BaTiO_3$ Thin Films. *Science*, 306(5698):1005–1009, 2004.

[5] Darrell G. Schlom, Long-Qing Chen, Chang-Beom Eom, Karin M. Rabe, Stephen K. Streiffer, and Jean-Marc Triscone. Strain Tuning of Ferroelectric Thin Films. *Annu. Rev. Mater. Res.*, 37:589–626, 2007.

[6] Maitri P. Warusawithana, Cheng Cen, Charles R. Sleasman, Joseph C. Woicik, Yulan Li, Lena Fitting Kourkoutis, Jeffrey A. Klug, Hao Li, Philip Ryan, Li-Peng Wang, M. J. Bedzyk, David A. Muller, Long-Qing Chen, Jeremy Levy, and Darrell G. Schlom. A Ferroelectric Oxide Made Directly on Silicon. *Science*, 324(5925):367–370, 2009.

[7] J.-P. Locquet, J. Perret, J. Fompeyrine, E. Mächler, J. W. Seo, and G. Van Tendeloo. Doubling the critical temperature of $La_{1.9}Sr_{0.1}CuO_4$ using epitaxial strain. *Nature*, 394(6692):453–456, 1998.

[8] S. Jin, T. H. Tiefel, M. McCormack, R. A. Fastnacht, R. Ramesha, and L. H. Chen. Thousandfold Change in Resistivity in Magnetoresistive La-Ca-Mn-O Films. *Science*, 264(5157):413–415, 1994.

[9] S. Jin, T. H. Tiefel, M. McCormack, H. M. O'Bryan, L. H. Chen, R. Ramesha, and D. Schurig. Thickness Dependence of Magnetoresistance in La-Ca-Mn-O Epitaxial-Films. *Appl. Phys. Lett.*, 67(4):557–559, 1995.

[10] T. Z. Ward, J. D. Budai, Z. Gai, J. Z. Tischler, Lifeng Yin, and J. Shen. Elastically driven anisotropic percolation in electronic phase-separated manganites. *Nat. Phys.*, 5(12):885–888, 2009.

[11] R. J. Zeches, M. D. Rossell, J. X. Zhang, A. J. Hatt, Q. He, C.-H. Yang, A. Kumar, C. H. Wang, A. Melville, C. Adamo, G. Sheng, Y.-H. Chu, J. F. Ihlefeld, R. Erni, C. Ederer, V. Gopalan, L. Q. Chen, D. G. Schlom, N. A. Spaldin, L. W. Martin, and R. Ramesha. A Strain-Driven Morphotropic Phase Boundary in $BiFeO_3$. *Science*, 326(5955):977–980, 2009.

[12] J. Chakhalian, A. J. Millis, and J. M. Rondinelli. Whither the oxide interface. *Nat. Mater.*, 11(2):92–94, 2012.

[13] James M. Rondinelli and Nicola A. Spaldin. Structure and Properties of Functional Oxide Thin Films: Insights From Electronic-Structure Calculations. *Adv. Mater.*, 23(30):3363–3381, 2011.

[14] Jiří Chaloupka and Giniyat Khaliullin. Orbital Order and Possible Superconductivity in $LaNiO_3/LaMO_3$ Superlattices. *Phys. Rev. Lett.*, 100(1):016404, 2008.

[15] P. Hansmann, Xiaoping Yang, A. Toschi, G. Khaliullin, O. K. Andersen, and K. Held. Turning a Nickelate Fermi Surface into a Cupratelike One through Heterostructuring. *Phys. Rev. Lett.*, 103(1):016401, 2009.

[16] P. Hansmann, A. Toschi, Xiaoping Yang, O. K. Andersen, and K. Held. Electronic structure of nickelates: From two-dimensional heterostructures to three-dimensional bulk materials. *Phys. Rev. B*, 82(23):235123, 2010.

[17] Y. Tokura and N. Nagaosa. Orbital Physics in Transition-Metal Oxides. *Science*, 288(5465):462–468, 2000.

[18] J. Chakhalian, J. M. Rondinelli, Jian Liu, B. A. Gray, M. Kareev, E. J. Moon, N. Prasai, J. L. Cohn, M. Varela, I-Cheng Tung, M. J. Bedzyk, S. G. Altendorf, F. Strigari, B. Dabrowski, L. H. Tjeng, P. J. Ryan, and J. W. Freeland. Asymmetric Orbital-Lattice Interactions in Ultrathin Correlated Oxide Films. *Phys. Rev. Lett.*, 107(11):116805, 2011.

[19] J. W. Freeland, Jian Liu, M. Kareev, B. Gray, J. W. Kim, P. Ryan, R. Pentcheva, and J. Chakhalian. Orbital control in strained ultra-thin $LaNiO_3/LaAlO_3$ superlattices. *Europhys. Lett.*, 96(5):57004, 2011.

[20] A. V. Boris, Y. Matiks, E. Benckiser, A. Frano, P. Popovich, V. Hinkov, P. Wochner, M. Castro-Colin, E. Detemple, V. K. Malik, C. Bernhard, T. Prokscha, A. Suter, Z. Salman, E. Morenzoni, G. Cristiani, H.-U. Habermeier, and B. Keimer. Dimensionality Control of Electronic Phase Transitions in Nickel-Oxide Superlattices. *Science*, 332(6032):937–940, 2011.

[21] Eva Benckiser, Maurits W. Haverkort, Sebastian Brück, Eberhard Goering, Sebastian Macke, Alex Frañó, Xiaoping Yang, Ole K. Andersen, Georg Cristiani, Hanns-Ulrich Habermeier, Alexander V. Boris, Ioannis Zegkinoglou, Peter Wochner, Heon-Jung Kim, Vladimir Hinkov, and Bernhard Keimer. Orbital reflectometry of oxide heterostructures. *Nat. Mater.*, 10(3):189–193, 2011.

[22] James M. Rondinelli, Steven J. May, and John W. Freeland. Control of octahedral connectivity in perovskite oxide heterostructures: An emerging route to multifunctional materials discovery. *MRS Bull.*, 37(03):261–270, 2012.

[23] Manuel Bibes, Javier E. Villegas, and Agnès Barthélémy. Ultrathin oxide films and interfaces for electronics and spintronics. *Adv. Phys.*, 60(1):5–84, 2011.

[24] W. Tian, J. H. Haeni, D. G. Schlom, E. Hutchinson, B. L. Sheu, M. M. Rosario, P. Schiffer, Y. Liu, M. A. Zurbuchen, and X. Q. Pan. Epitaxial growth and magnetic properties of the first five members of the layered $Sr_{n+1}Ru_nO_{3n+1}$ oxide series. *Appl. Phys. Lett.*, 90(2):022507, 2007.

[25] Turan Birol, Nicole A. Benedek, and Craig J. Fennie. Interface Control of Emergent Ferroic Order in Ruddlesden-Popper $Sr_{n+1}Ti_nO_{3n+1}$. *Phys. Rev. Lett.*, 107(25):257602, 2011.

[26] Che-Hui Lee, Nikolas J. Podraza, Ye Zhu, Robert F. Berger, Shaoping Shen, Michelle Sestak, Robert W. Collins, Lena F. Kourkoutis, Julia A. Mundy, Huiqiong Wang, Qingyun Mao, Xiaoxing Xi, Leonard J. Brillson, Jeffrey B. Neaton, David A. Muller, and Darrell G. Schlom. Effect of reduced dimensionality on the optical band gap of $SrTiO_3$. *Appl. Phys. Lett.*, 102(12):122901, 2013.

[27] Darrell G. Schlom, Long-Qing Chen, Xiaoqing Pan, Andreas Schmehl, and Mark A. Zurbuchen. A Thin Film Approach to Engineering Functionality into Oxides. *J. Am. Ceram. Soc.*, 91(8):2429–2454, 2008.

[28] I. Markov and S. Stoyanov. Mechanisms of epitaxial growth. *Contemp. Phys.*, 28(3):267–320, 1987.

[29] Harald Brune. Microscopic view of epitaxial metal growth: nucleation and aggregation. *Surf. Sci. Rep.*, 31(4-6):121–229, 1998.

[30] J. W. Evans, P. A. Thiel, and M. C. Bartelt. Morphological evolution during epitaxial thin film growth: Formation of 2D islands and 3D mounds. *Surf. Sci. Rep.*, 61(1-2):1–128, 2006.

[31] Scott A. Chambers. Epitaxial growth and properties of thin film oxides. *Surf. Sci. Rep.*, 39(5):105–180, 2000.

[32] S. Yadavalli, M. H. Yang, and C. P. Flynn. Low-temperature growth of MgO by molecular-beam epitaxy. *Phys. Rev. B*, 1990.

[33] P. V. Chinta and R. L. Headrick. Bimodal Island Size Distribution in Heteroepitaxial Growth. *Phys. Rev. Lett.*, 112(7):075503, 2014.

[34] Mark Huijben, Gertjan Koster, Michelle K. Kruize, Sander Wenderich, Jo Verbeeck, Sara Bals, Erik Slooten, Bo Shi, Hajo J. A. Molegraaf, Josee E. Kleibeuker, Sandra van Aert, Jeroen B. Goedkoop, Alexander Brinkman, Dave H. A. Blank, Mark S. Golden, Gustaaf van Tendeloo, Hans Hilgenkamp, and Guus Rijnders. Defect Engineering in Oxide Heterostructures by Enhanced Oxygen Surface Exchange. *Adv. Funct. Mater.*, 23(42):5240–5248, 2013.

[35] Ryota Shimizu, Katsuya Iwaya, Takeo Ohsawa, Susumu Shiraki, Tetsuya Hasegawa, Tomihiro Hashizume, and Taro Hitosugi. Atomic-Scale Visualization of Initial Growth of Homoepitaxial $SrTiO_3$ Thin Film on an Atomically Ordered Substrate. *ACS Nano*, 5(10):7967–7971, 2011.

[36] Akihiro Kushima, Sidney Yip, and Bilge Yildiz. Competing strain effects in reactivity of $LaCoO_3$ with oxygen. *Phys. Rev. B*, 82(11):115435, 2010.

[37] Ulrich Aschauer, Reto Pfenninger, Sverre M. Selbach, Tor Grande, and Nicola A. Spaldin. Strain-controlled oxygen vacancy formation and ordering in $CaMnO_3$. *Phys. Rev. B*, 88(5):054111, 2013.

[38] Naoyuki Nakagawa, Harold Y. Hwang, and David A. Muller. Why some interfaces cannot be sharp. *Nat. Mater.*, 5(3):204–209, 2006.

[39] J. L. Blok, X. Wan, G. Koster, D. H. A. Blank, and G. Rijnders. Epitaxial oxide growth on polar (111) surfaces. *Appl. Phys. Lett.*, 99(15):151917, 2011.

[40] R. Herger, P. R. Willmott, C. M. Schlepütz, M. Björck, S. A. Pauli, D. Martoccia, B. D. Patterson, D Kumah, R Clarke, Y. Yacoby, and M Döbeli. Structure determination of monolayer-by-monolayer grown $La_{1x}Sr_xMnO_3$ thin films and the onset of magnetoresistance. *Phys. Rev. B*, 77(8):085401, 2008.

[41] Tim T. Fister, Dillon D. Fong, Jeffrey A. Eastman, Peter M. Baldo, Matthew J. Highland, Paul H. Fuoss, Kavaipatti R. Balasubramaniam, Joanna C. Meador, and Paul A. Salvador. In situ characterization of strontium surface segregation in epitaxial $La_{0.7}Sr_{0.3}MnO_3$ thin films as a function of oxygen partial pressure. *Appl. Phys. Lett.*, 93(15):151904, 2008.

[42] Yizhak Yacoby, Hua Zhou, Ron Pindak, and Ivan Božović. Atomic-layer synthesis and imaging uncover broken inversion symmetry in $La_{2x}Sr_xCuO_4$ films. *Phys. Rev. B*, 87(1):014108, 2013.

[43] Edith Perret, Changyong Park, Dillon D. Fong, Kee-Chul Chang, Brian J. Ingram, Jeffrey A. Eastman, Peter M. Baldo, and Paul H. Fuoss. Resonant X-ray scattering studies of epitaxial complex oxide thin films. *J. Appl. Cryst.*, 46(1):76–87, 2013.

[44] Pavlo Zubko, Stefano Gariglio, Marc Gabay, Philippe Ghosez, and Jean-Marc Triscone. Interface Physics in Complex Oxide Heterostructures. *Annu. Rev. Condens. Matter Phys.*, 2(1):141–165, 2011.

[45] Cheng Cen, Stefan Thiel, Jochen Mannhart, and Jeremy Levy. Oxide Nanoelectronics on Demand. *Science*, 323(5917):1026–1030, 2009.

[46] J. Mannhart and D. G. Schlom. Oxide Interfaces-An Opportunity for Electronics. *Science*, 327(5973):1607–1611, 2010.

[47] A. V. Ievlev, S. Jesse, A. N. Morozovska, E. Strelcov, E. A. Eliseev, Y. V. Pershin, A. Kumar, V. Ya. Shur, and S. V. Kalinin. Intermittency, quasiperiodicity and chaos inprobe-induced ferroelectric domain switching. *Nat. Phys.*, 10(1):59–66, 2013.

[48] S. M. Nakhmanson and Ivan Naumov. Goldstone-like States in a Layered Perovskite with Frustrated Polarization: A First-Principles Investigation of $PbSr_2Ti_2O_7$. *Phys. Rev. Lett.*, 104(9):097601, 2010.

[49] James M. Rondinelli and Craig J. Fennie. Octahedral Rotation-Induced Ferroelectricity in Cation Ordered Perovskites. *Adv. Mater.*, 24(15):1961–1968, 2012.

[50] H. Y. Hwang, Y. Iwasa, M. Kawasaki, B. Keimer, N. Nagaosa, and Y. Tokura. Emergent phenomena at oxide interfaces. *Nat. Mater.*, 11(2):103–113, 2012.

[51] P. Fisher, S. Wang, M. Skowronski, P. A. Salvador, M. Snyder, and O. Maksimov. A series of layered intergrowth phases grown by molecular beam epitaxy: Sr_mTiO_{2+m}(m=1–5). *Appl. Phys. Lett.*, 91(25):252901, 2007.

[52] Bernard Mercey, Paul A. Salvador, Wilfrid Prellier, Trong-Duc Doan, Jérôme Wolfman, Maryvonne Hervieu, and Bernard Raveau. Thin film deposition: a novel synthetic route to new materials. *J. Mater. Chem.*, 9(1):233–242, 1999.

[53] S. J. May, P. J. Ryan, J. L. Robertson, J.-W. Kim, T. S. Santos, E. Karapetrova, J. L. Zarestky, X. Zhai, S. G. E. te Velthuis, J. N. Eckstein, S. D. Bader, and A. Bhattacharya. Enhanced ordering temperatures in antiferromagnetic manganite superlattices. *Nat. Mater.*, 8(11):892–897, 2009.

[54] Eric J. Monkman, Carolina Adamo, Julia A. Mundy, Daniel E. Shai, John W. Harter, Dawei Shen, Bulat Burganov, David A. Muller, Darrell G. Schlom, and Kyle M. Shen. Quantum many-body interactions in digital oxide superlattices. *Nat. Mater.*, 11(10):855–859, 2012.

[55] J. H. Haeni, C. D. Theis, and D. G. Schlom. RHEED Intensity Oscillations for the Stoichiometric Growth of $SrTiO_3$ Thin Films by Reactive Molecular Beam Epitaxy. *J. Electroceram.*, 4(2-3):385–391, 2000.

[56] I-Cheng Tung, P. V. Balachandran, Jian Liu, B. A. Gray, E. A. Karapetrova, J. H. Lee, J. Chakhalian, M. J. Bedzyk, J. M. Rondinelli, and J. W. Freeland. Connecting bulk symmetry and orbital polarization in strained $RNiO_3$ ultrathin films. *Phys. Rev. B*, 88(20):205112, 2013.

[57] J. H. Lee, G. Luo, I-Cheng Tung, S. H. Chang, Z Luo, M Malshe, M Gadre, A. Bhattacharya, S. M. Nakhmanson, J. A. Eastman, H Hong, J Jellinek, D Morgan, D. D. Fong, and J. W. Freeland. Dynamic layer rearrangement during growth of layered oxide films by molecular beam epitaxy. *Nat. Mater.*, 13(9):879–883, 2014.

[58] Gertjan Koster, B. L. Kropman, Guus J. H. M. Rijnders, Dave H. A. Blank, and Horst Rogalla. Quasi-ideal strontium titanate crystal surfaces through formation of strontium hydroxide. *Appl. Phys. Lett.*, 73(20):2920–2922, 1998.

[59] Josée E. Kleibeuker, Gertjan Koster, Wolter Siemons, David Dubbink, Bouwe Kuiper, Jeroen L. Blok, Chan-Ho Yang, Jayakanth Ravichandran, Ramamoorthy Ramesh, Johan E. ten Elshof, Dave H. A. Blank, and Guus Rijnders. Atomically Defined Rare-Earth Scandate Crystal Surfaces. *Adv. Funct. Mater.*, 20(20):3490–3496, 2010.

[60] A. Y. Cho. Epitaxy by periodic annealing. *Surf. Sci.*, 17(2):494–503, 1969.

[61] A. Y. Cho and J. R. Arthur. Molecular beam epitaxy. *Prog. Solid State Chem.*, 10:157–191, 1975.

[62] Robin F. C. Farrow. *Molecular Beam Epitaxy: Applications to Key Materials*. NoyesPublications, Park Ridge, New Jersey, 1995.

[63] M. A. Herman and H. Sitter. *Molecular Beam Epitaxy: Fundamentals and Current Status*, volume 7. Springer Series in Materials Science (Springer, Berlin 1996) p, 1997.

[64] Ayahiko Ichimiya and Philip I. Cohen. *Reflection High-Energy Electron Diffraction*. Cambridge University Press, 2004.

[65] Hawoong Hong and T.-C. Chiang. A six-circle diffractometer system for synchrotron X-ray studies of surfaces and thin film growth by molecular beam epitaxy. *Nucl. Instrum. Meth. A*, 572(2):942–947, 2007.

[66] D. G. Schlom, A. F. Marshall, J. T. Sizemore, Z. J. Chen, J. N. Eckstein, I. Bozovic, K. E. von Dessonneck, J. S. Harris, Jr., and J. C. Bravman. Molecular beam epitaxial growth of layered Bi-Sr-Ca-Cu-O compounds. *J. Cryst. Growth*, 102(3):361–375, 1990.

[67] Yoshiji Horikoshi, Minoru Kawashima, and Hiroshi Yamaguchi. Migration-Enhanced Epitaxy of GaAs and AlGaAs. *Jpn. J. Appl. Phys.*, 27(2):169–179, 1988.

[68] I. K. Robinson. Crystal truncation rods and surface roughness. *Phys. Rev. B*, 33(6):3830, 1986.

[69] R. Feidenhans'l. Surface structure determination by X-ray diffraction. *Surf. Sci. Rep.*, 10(3):105–188, 1989.

[70] I. K. Robinson and D. J. Tweet. Surface x-ray diffraction. *Rep. Prog. Phys.*, 55(5):599, 1992.

[71] Paul Fenter and Neil C. Sturchio. Mineral–water interfacial structures revealed by synchrotron X-ray scattering. *Prog. Surf. Sci.*, 77(5-8):171–258, 2004.

[72] I. K. Robinson. Surface Crystallography. In G. S. Brown and D E Moncton, editors, *Handbook on Synchrotron Radiation, Vol. 3*, pages 223–266. North Holland, New York, 1991.

[73] B. E. Warren. *X-ray Diffraction*. Dover, 1969.

[74] Jens Als-Nielsen and Des McMorrow. *Elements of Modern X-ray Physics*. Wiley, Hoboken, NJ, 2nd edition, 2011.

[75] E. Vlieg, J. F. van der Veen, J. E. Macdonald, and M. Miller. Angle Calculations for a Five-Circle Diffractometer Used for Surface X-ray Diffraction. *J. Appl. Cryst.*, 20(5):330–337, 1987.

[76] S. G. J. Mochrie. Four-Circle Angle Calculations for Surface Diffraction. *J. Appl. Cryst.*, 21(1):1–3, 1988.

[77] I. K. Robinson. Four-circle diffractometry for surfaces (invited). *Rev. Sci. Instrum.*, 60(7):1541, 1989.

[78] Martin Lohmeier and Elias Vlieg. Angle Calculations for a Six-Circle Surface X-ray Diffractometer. *J. Appl. Cryst.*, 26(5):706–716, 1993.

[79] I. K. Robinson, H. Graafsma, A. Kvick, and J. Linderholm. First testing of the fast kappa diffractometers at National Synchrotron Light Source and European Synchrotron Radiation Facility. *Rev. Sci. Instrum.*, 66(2):1765, 1995.

[80] H. You. Angle calculations for a '4S+2D' six-circle diffractometer. *J. Appl. Cryst.*, 32(4):614–623, 1999.

[81] Oliver Bunk and Martin Meedom Nielsen. Angle calculations for a z-axis/(2S+2D) hybrid diffractometer. *J. Appl. Cryst.*, 37:216–222, 2004.

[82] C. M. Schlepütz, S.O. Mariager, Stephan A. Pauli, R. Feidenhans'l, and P. R. Willmott. Angle calculations for a (2+3)-type diffractometer: focus on area detectors. *J. Appl. Cryst.*, 44:73–83, 2011.

[83] P. R. Willmott, C. M. Schlepütz, R. Herger, B. D. Patterson, O. Bunk, Ch. Brönnimann, B. Henrich, G. Hülsen, and E. F. Eikenberry. A Single-photon Counting Pixel Detector for Surface Diffraction Experiments. *Synchrotron Radiat. News*, 18(2):16–22, 2005.

[84] C. M. Schlepütz, R. Herger, P. R. Willmott, B. D. Patterson, O. Bunk, Ch. Brönnimann, B. Henrich, G. Hülsen, and E. F. Eikenberry. Improved data acquisition in grazing-incidence X-ray scattering experiments using a pixel detector. *Acta Cryst. A*, 61:418–425, 2005.

[85] P. Fenter, J. G. Catalano, C. Park, and Z. Zhang. On the use of CCD area detectors for high-resolution specular X-ray reflectivity. *J. Synchrotron Radiat.*, 13(4):293–303, 2006.

[86] Paul A. Fenter. X-ray reflectivity as a probe of mineral-fluid interfaces: A user guide. *Rev. Mineral. Geochem.*, 49(1):149–221, 2002.

[87] J. R. Fienup. Reconstruction of an object from the modulus of its Fourier transform. *Opt. Lett.*, 3(1):27–29, 1978.

[88] P. Fenter and Z. Zhang. Model-independent one-dimensional imaging of interfacial structures at ¡1Å resolution. *Phys. Rev. B*, 72(8):081401(R), 2005.

[89] Y. Yacoby, R Pindak, R MacHarrie, L Pfeiffer, L Berman, and R Clarke. Direct structure determination of systems with two-dimensional periodicity. *J. Phys. Condens. Matter*, 12(17):3929–3938, 2000.

[90] Yizhak Yacoby, Mukhles Sowwan, Edward Stern, Julie O. Cross, Dale Brewe, Ron Pindak, John Pitney, Eric M. Dufresne, and Roy Clarke. Direct determination of epitaxial interface structure in Gd_2O_3 passivation of GaAs. *Nat. Mater.*, 1(2):99–101, 2002.

[91] D. D. Fong, C Cionca, Y. Yacoby, G. B. Stephenson, J. A. Eastman, P. H. Fuoss, S. K. Streiffer, Carol Thompson, R Clarke, R Pindak, and E A Stern. Direct structural determination in ultrathin ferroelectric films by analysis of synchrotron x-ray scattering measurements. *Phys. Rev. B*, 71(14):144112, 2005.

[92] J. Stöhr and S. Anders. X-ray spectro-microscopy of complex materials and surfaces. *IBM J. Res. Dev.*, 44(4):535–551, 2000.

[93] Frank de Groot. High-Resolution X-ray Emission and X-ray Absorption Spectroscopy. *Chem. Rev.*, 101(6):1779–1808, 2001.

[94] C. T. Chen, L. H. Tjeng, J. Kwo, H. L. Kao, P. Rudolf, F. Sette, and R. M. Fleming. Out-of-Plane Orbital Characters of Intrinsic and Doped Holes in $La_{2-X}Sr_XCuO_4$. *Phys. Rev. Lett.*, 68(16):2543–2546, 1992.

[95] Sarnjeet S. Dhesi, Gerrit van der Laan, Esther Dudzik, and Alexander B. Shick. Anisotropic Spin-Orbit Coupling and Magnetocrystalline Anisotropy in Vicinal Co Films. *Phys. Rev. Lett.*, 87(6):067201, 2001.

[96] María Luisa Medarde. Structural, magnetic and electronic properties of $RNiO_3$perovskites (R= rare earth). *J. Phys. Condens. Matter*, 9(8):1679, 1997.

[97] M. Medarde, J. Mesot, S. Rosenkranz, P. Lacorre, W. Marshall, S. Klotz, J. S. Loveday, G. Hamel, S. Hull, and P. Radaelli. Pressure-induced orthorhombic-rhombohedral phase transition in $NdNiO_3$. *Physica B*, 234-236:15–17, 1997.

[98] J. B. Torrance, P. Lacorre, A. I. Nazzal, E. J. Ansaldo, and Ch. Niedermayer. Systematic Study of Insulator-Metal Transitions in Perovskites $RNiO_3$ (R = Pr, Nd, Sm, Eu) due to Closing of Charge-Transfer Gap. *Phys. Rev. B*, 45(14):8209–8212, 1992.

[99] Jian Liu, M. Kareev, B. Gray, J. W. Kim, P. Ryan, B. Dabrowski, J. W. Freeland, and J. Chakhalian. Strain-mediated metal-insulator transition in epitaxial ultrathin films of $NdNiO_3$. *Appl. Phys. Lett.*, 96(23):233110, 2010.

[100] Raoul Scherwitzl, Pavlo Zubko, I Gutierrez Lezama, Shimpei Ono, Alberto F Morpurgo, Gustau Catalan, and Jean-Marc Triscone. Electric-Field Control of the Metal-Insulator Transition in Ultrathin $NdNiO_3$ Films. *Adv. Mater.*, 22(48):5517–5520, 2010.

[101] J. L. García-Muñoz, J. Rodríguez-Carvajal, P. Lacorre, and J. B. Torrance. Neutron-Diffraction Study of $RNiO_3$ (R = La,Pr,Nd,Sm): Electronically Induced Structural-Changes Across the Metal-Insulator-Transition. *Phys. Rev. B*, 46(8):4414–4425, 1992.

[102] Jian Liu, M. Kareev, S. Prosandeev, B. Gray, P. Ryan, J. W. Freeland, and J. Chakhalian. Effect of polar discontinuity on the growth of $LaNiO_3/LaAlO_3$ superlattices. *Appl. Phys. Lett.*, 96(13):133111, 2010.

[103] Dave H. A. Blank, Gertjan Koster, Guus A. J. H. M. Rijnders, Eelco van Setten, Per Slycke, and Horst Rogalla. Epitaxial growth of oxides with pulsed laser interval deposition. *J. Cryst. Growth*, 211:98–105, 2000.

[104] M. Kareev, S. Prosandeev, J. Liu, C. Gan, A Kareev, J. W. Freeland, Min Xiao, and J. Chakhalian. Atomic control and characterization of surface defect states of TiO_2 terminated $SrTiO_3$ single crystals. *Appl. Phys. Lett.*, 93(6):061909, 2008.

[105] J. W. Freeland, J. C. Lang, G. Srajer, R. Winarski, D. Shu, and D. M. Mills. A unique polarized x-ray facility at the Advanced Photon Source. *Rev. Sci. Instrum.*, 73(3):1408, 2002.

[106] U. Gebhardt, N. V. Kasper, A. Vigliante, P. Wochner, H. Dosch, F. S. Razavi, and H.-U. Habermeier. Formation and Thickness Evolution of Periodic Twin Domains in Manganite Films Grown on $SrTiO_3$(001) Substrates. *Phys. Rev. Lett.*, 98(9):096101, 2007.

[107] A. Vailionis, H. Boschker, W. Siemons, E. P. Houwman, D. H. A. Blank, G. Rijnders, and G. Koster. Misfit strain accommodation in epitaxial ABO_3 perovskites: Lattice rotations and lattice modulations. *Phys. Rev. B*, 83(6):064101, 2011.

[108] R. Scherwitzl, P. Zubko, C. Lichtensteiger, and J.-M. Triscone. Electric-field tuning of the metal-insulator transition in ultrathin films of $LaNiO_3$. *Appl. Phys. Lett.*, 95(22):222114, 2009.

[109] Sang Soo Lee, Changyong Park, Paul Fenter, Neil C. Sturchio, and Kathryn L. Nagy. Competitive adsorption of strontium and fulvic acid at the muscovite–solution interface observed with resonant anomalous X-ray reflectivity. *Geochim. Cosmochim. Acta*, 74(6):1762–1776, 2010.

[110] William H. Press. *Numerical Recipes: The Art of Scientific Computing*. Cambridge University Press, 3rd edition, 2007.

[111] S. J. May, C. R. Smith, J.-W. Kim, E. Karapetrova, A. Bhattacharya, and P. J. Ryan. Control of octahedral rotations in $(LaNiO_3)_n/(SrMnO_3)_m$ superlattices. *Phys. Rev. B*, 83(15):153411, 2011.

[112] A. M. Glazer. Simple Ways of Determining Perovskite Structures. *Acta Cryst. A*, 31:756–762, 1975.

[113] S. J. May, J.-W. Kim, J. M. Rondinelli, E. Karapetrova, N. A. Spaldin, A. Bhattacharya, and P. J. Ryan. Quantifying octahedral rotations in strained perovskite oxide films. *Phys. Rev. B*, 82(1):014110, 2010.

[114] C. L. Jia, S. B. Mi, M. Faley, U. Poppe, J. Schubert, and K. Urban. Oxygen octahedron reconstruction in the $SrTiO_3/LaAlO_3$ heterointerfaces investigated using aberration-corrected ultrahigh-resolution transmission electron microscopy. *Phys. Rev. B*, 79(8):081405(R), 2009.

[115] A. Y. Borisevich, H. J. Chang, M. Huijben, M. P. Oxley, S. Okamoto, M. K. Niranjan, J. D. Burton, E. Y. Tsymbal, Y. H. Chu, P. Yu, R. Ramesha, S. V. Kalinin, and S. J. Pennycook. Suppression of Octahedral Tilts and Associated Changes in Electronic Properties at Epitaxial Oxide Heterostructure Interfaces. *Phys. Rev. Lett.*, 105(8):087204, 2010.

[116] Jinwoo Hwang, Jack Y. Zhang, Junwoo Son, and Susanne Stemmer. Nanoscale quantification of octahedral tilts in perovskite films. *Appl. Phys. Lett.*, 100(19):191909, 2012.

[117] J.-S. Zhou and J. B. Goodenough. Chemical bonding and electronic structure of $RNiO_3$ (R=rare earth). *Phys. Rev. B*, 69(15):153105, 2004.

[118] K. H. Ahn, T. Lookman, and A. R. Bishop. Strain-induced metal-insulator phase coexistence in perovskite manganites. *Nature*, 428(6981):401–404, 2004.

[119] Branton J. Campbell, Harold T. Stokes, David E. Tanner, and Dorian M. Hatch. ISODISPLACE: a web-based tool for exploring structural distortions. *J. Appl. Cryst.*, 39(4):607–614, 2006.

[120] J. M. Perez-Mato, D. Orobengoa, and M. I. Aroyo. Mode crystallography of distorted structures. *Acta Cryst. A*, 66:558–590, 2010.

[121] Prasanna V. Balachandran and James M. Rondinelli. Interplay of octahedral rotations and breathing distortions in charge-ordering perovskite oxides. *Phys. Rev. B*, 88(5):054101, 2013.

[122] John P. Perdew, Adrienn Ruzsinszky, Gábor I. Csonka, Oleg A. Vydrov, Gustavo E. Scuseria, Lucian A. Constantin, Xiaolan Zhou, and Kieron Burke. Restoring the Density-Gradient Expansion for Exchange in Solids and Surfaces. *Phys. Rev. Lett.*, 100(13):136406, 2008.

[123] Vladimir I. Anisimov, F. Aryasetiawan, and A. I. Lichtenstein. First-principles calculations of the electronic structure and spectra of strongly correlated systems: The LDA+U method. *J. Phys. Condens. Matter*, 9(4):767–808, 1997.

[124] S. L. Dudarev, G. A. Botton, S. Y Savrasov, C. J. Humphreys, and A. P. Sutton. Electron-energy-loss spectra and the structural stability of nickel oxide: An LSDA+U study. *Phys. Rev. B*, 57(3):1505–1509, 1998.

[125] G. Kresse and J. Furthmüller. Efficient iterative schemes for ab initio total-energy calculations using a plane-wave basis set. *Phys. Rev. B*, 54(16):11169–11186, 1996.

[126] G. Kresse and D. Joubert. From ultrasoft pseudopotentials to the projector augmented-wave method. *Phys. Rev. B*, 59(3):1758–1775, 1999.

[127] P. E. Blöchl. Projector augmented-wave method. *Phys. Rev. B*, 50(24):17953, 1994.

[128] Hendrik J. Monkhorst and James D. Pack. Special Points for Brillouin-Zone Integrations. *Phys. Rev. B*, 13(12):5188–5192, 1976.

[129] P. Lacorre, J. B. Torrance, J Pannetier, A. I. Nazzal, P. W. Wang, and C W Huang. Synthesis, Crystal-Structure, and Properties of Metallic $PrNiO_3$: Comparison with Metallic $NdNiO_3$ and Semiconducting $SmNiO_3$. *J. Solid State Chem.*, 91(2):225–237, 1991.

[130] J. N. Eckstein and I. Bozovic. High-temperature superconducting multilayers and heterostructures grown by atomic layer-by-layer molecular beam epitaxy. *Annu. Rev. Mater. Sci.*, 25(1):679–709, 1995.

[131] Hideki Yamamoto, Michio Naito, and Hisashi Sato. A New Superconducting Cuprate Prepared by Low-Temperature Thin-Film Synthesis in a Ba–Cu–O System. *Jpn. J. Appl. Phys.*, 36(3B):L341, 1997.

[132] Jean-Pierre Locquet, André Catana, Erich Mächler, Christoph Gerber, and J. Georg Bednorz. Block-by-block deposition: A new growth method for complex oxide thin films. *Appl. Phys. Lett.*, 64(3):372, 1994.

[133] S. N. Ruddlesden and P. Popper. New compounds of the K_2NiF_4 type. *Acta Cryst.*, 10(8):538–539, 1957.

[134] J. H. Haeni, C. D. Theis, D. G. Schlom, W. Tian, X. Q. Pan, H. Chang, I. Takeuchi, and X.-D. Xiang. Epitaxial growth of the first five members of the $Sr_{n+1}Ti_nO_{3n+1}$ Ruddlesden–Popper homologous series. *Appl. Phys. Lett.*, 78(21):3292, 2001.

[135] K. R. Udayakumar and Alastair N. Cormack. Structural Aspects of Phase Equilibria in the StrontiumTitaniumOxygen System. *J. Am. Ceram. Soc.*, 71(11):C469–C471, 1988.

[136] Claudine Noguera. Theoretical investigation of the Ruddlesden-Popper compounds $Sr_{n+1}Ti_nO_{3n+1}$ (n=1-3). *Philos. Mag. Lett.*, 80(3):173–180, 2000.

[137] O. Le Bacq, E. Salinas, A. Pisch, C. Bernard, and A. Pasturel. First-principles structural stability in the strontium–titanium–oxygen system. *Philos. Mag.*, 86(15):2283–2292, 2006.

[138] Michael A. Mccoy, Robin W. Grimes, and William E. Lee. Phase stability and interfacial structures in the SrO–$SrTiO_3$ system. *Philos. Mag. A*, 75(3):833–846, 1997.

[139] W. Tian, X. Q. Pan, J. H. Haeni, and D. G. Schlom. Transmission electron microscopy study of n=1–5 $Sr_{n+1}Ti_nO_{3n+1}$ epitaxial thin films. *J. Mater. Res.*, 16(7):2013–2026, 2001.

[140] Che-Hui Lee, Nathan D. Orloff, Turan Birol, Ye Zhu, Veronica Goian, Eduard Rocas, Ryan Haislmaier, Eftihia Vlahos, Julia A. Mundy, Lena F. Kourkoutis, Yuefeng Nie, Michael D. Biegalski, Jingshu Zhang, Margitta Bernhagen, Nicole A. Benedek, Yongsam Kim, Joel D. Brock, Reinhard Uecker, X. X. Xi, Venkatraman Gopalan, Dmitry Nuzhnyy, Stanislav Kamba, David A. Muller, Ichiro Takeuchi, James C. Booth, Craig J. Fennie, and Darrell G. Schlom. Exploiting dimensionality and defect mitigation to create tunable microwave dielectrics. *Nature*, 502(7472):532–536, 2013.

[141] Y. F. Nie, Y. Zhu, C.-H. Lee, L. F. Kourkoutis, J. A. Mundy, J. Junquera, Ph. Ghosez, D. J. Baek, S. Sung, X. X. Xi, K. M. Shen, D. A. Muller, and D. G. Schlom. Atomically precise interfaces from non-stoichiometric deposition. *Nat. Commun.*, 5:4530, 2014.

[142] P. R. Willmott, S. A. Pauli, R. Herger, C. M. Schlepütz, D. Martoccia, B. D. Patterson, B. Delley, R. Clarke, D. Kumah, C. Cionca, and Y. Yacoby. Structural Basis for the Conducting Interface between $LaAlO_3$ and $SrTiO_3$. *Phys. Rev. Lett.*, 99(15):155502, 2007.

[143] G. Kresse and J. Furthmüller. Efficiency of ab-initio total energy calculations for metals and semiconductors using a plane-wave basis set. *Comp. Mater. Sci.*, 6(1):15–50, 1996.

[144] S. Sekiguchi, M. Fujimoto, M. Nomura, Sung-Baek Cho, J. Tanaka, T. Nishihara, Min-Gu Kang, and Hyoung-Ho Park. Atomic force microscopic observation of $SrTiO_3$ polar surface. *Solid State Ionics*, 108(1):73–79, 1998.

[145] Roman Wahl, Doris Vogtenhuber, and Georg Kresse. $SrTiO_3$ and $BaTiO_3$ revisited using the projector augmented wave method: Performance of hybrid and semilocal functionals. *Phys. Rev. B*, 78(10):104116, 2008.

[146] Jacek Goniakowski, Fabio Finocchi, and Claudine Noguera. Polarity of oxide surfaces and nanostructures. *Rep. Prog. Phys.*, 71(1):016501, 2008.

[147] Kuan-Ting Wu, Yeong-Ah Soh, and Stephen J. Skinner. Epitaxial growth of mixed conducting layered Ruddlesden-Popper $La_{n+1}Ni_nO_{3n+1}$ (n= 1, 2 and 3) phases by pulsed laser deposition. *Mater. Res. Bull.*, 48(10):3783–3789, 2013.

[148] Z. Zhang, M. Greenblatt, and J. B. Goodenough. Synthesis, Structure, and Properties of the Layered Perovskite $La_3Ni_2O_{7-\delta}$. *J. Solid State Chem.*, 108(2):402–409, 1994.

[149] Nicole A. Benedek and Craig J. Fennie. Hybrid Improper Ferroelectricity: A Mechanism for Controllable Polarization-Magnetization Coupling. *Phys. Rev. Lett.*, 106(10):107204, 2011.

[150] Andrew T. Mulder, Nicole A. Benedek, James M. Rondinelli, and Craig J. Fennie. Turning ABO_3 Antiferroelectrics into Ferroelectrics: Design Rules for Practical Rotation-Driven Ferroelectricity in Double Perovskites and $A_3B_2O_7$ Ruddlesden-Popper Compounds. *Adv. Funct. Mater.*, 23:4810–4820, 2013.

[151] E. Vlieg, A. W. Denier van der Gon, J. F. van der Veen, J. E. Macdonald, and C. Norris. Surface X-Ray Scattering during Crystal Growth: Ge on Ge (111). *Phys. Rev. Lett.*, 61(19):2241, 1988.

[152] Masamitu Takahasi, Yasuhiro Yoneda, Hirotane Inoue, Naomasa Yamamoto, and Jun'ichiro Mizuki. X-Ray Diffractometer for Studies on Molecular-Beam-Epitaxy Growth of III–V Semiconductors. *Jpn. J. Appl. Phys.*, 41(Part 1, No. 10):6247–6251, 2002.

[153] Guus J. H. M. Rijnders, Gertjan Koster, Dave H. A. Blank, and Horst Rogalla. In situ monitoring during pulsed laser deposition of complex oxides using reflection high energy electron diffraction under high oxygen pressure. *Appl. Phys. Lett.*, 70(14):1888–1890, 1997.

[154] C. M. Brooks, L. Fitting Kourkoutis, T. Heeg, J. Schubert, D. A. Muller, and D. G. Schlom. Growth of homoepitaxial $SrTiO_3$ thin films by molecular-beam epitaxy. *Appl. Phys. Lett.*, 94(16):162905, 2009.

[155] Dillon D. Fong and Carol Thompson. In Situ Synchrotron X-Ray Studies of Ferroelectric Thin Films. *Annu. Rev. Mater. Res.*, 36(1):431–465, 2006.

[156] D. D. Fong, C. A. Lucas, M.-I. Richard, and M. F. Toney. X-Ray Probes for In Situ Studies of Interfaces. *MRS Bull.*, 35(07):504–513, 2010.

[157] Aaron Fleet, Darren Dale, A. R. Woll, Y. Suzuki, and J. D. Brock. Multiple Time Scales in Diffraction Measurements of Diffusive Surface Relaxation. *Phys. Rev. Lett.*, 96(5):055508, 2006.

[158] J. D. Ferguson, G. Arikan, D. S. Dale, A. R. Woll, and J. D. Brock. Measurements of Surface Diffusivity and Coarsening during Pulsed Laser Deposition. *Phys. Rev. Lett.*, 103(25):256103, 2009.

[159] C. D. Theis and D. G. Schlom. Cheap and stable titanium source for use in oxide molecular beam epitaxy systems. *J. Vac. Sci. Technol. A*, 14(4):2677–2679, 1996.

[160] G. Eres, J. Z. Tischler, M. Yoon, B. C. Larson, C. M. Rouleau, D. H. Lowndes, and P. Zschack. Time-resolved study of $SrTiO_3$ homoepitaxial pulsed-laser deposition using surface x-ray diffraction. *Appl. Phys. Lett.*, 80(18):3379, 2002.

[161] P Hahn, J Clabes, and M. Henzler. LEED-investigations and work-function measurements of the first stages of epitaxy of tungsten on tungsten (110). *J. Appl. Phys.*, 51(4):2079, 1980.

[162] M. C. Bartelt and J. W. Evans. Nucleation and growth of square islands during deposition: Sizes, coalescence, separations and correlations. *Surf. Sci.*, 298(2):421–431, 1993.

[163] A Guinier. *X-Ray Diffraction in Crystals, Imperfect Crystals, and Amorphous Bodies.* Dover, New York, 1994.

[164] Mario Birkholz. *Thin Film Analysis by X-Ray Scattering.* WILEY-VCH, Weinheim, 2006.

[165] Tsuyoshi Ohnishi, Keisuke Shibuya, Takahisa Yamamoto, and Mikk Lippmaa. Defects and transport in complex oxide thin films. *J. Appl. Phys.*, 103(10):103703, 2008.

[166] B. Jalan, Roman Engel-Herbert, Nicholas J Wright, and Susanne Stemmer. Growth of high-quality $SrTiO_3$ films using a hybrid molecular beam epitaxy approach. *J. Vac. Sci. Technol. A*, 27(3):461, 2009.

[167] E. J. Tarsa, E. A. Hachfeld, F. T. Quinlan, J. S. Speck, and M. Eddy. Growth-related stress and surface morphology in homoepitaxial $SrTiO_3$ films. *Appl. Phys. Lett.*, 68(4):490–492, 1996.

[168] T Ohnishi, M. Lippmaa, T Yamamoto, S Meguro, and H. Koinuma. Improved stoichiometry and misfit control in perovskite thin film formation at a critical fluence by pulsed laser deposition. *Appl. Phys. Lett.*, 87(24):241919, 2005.

[169] James M LeBeau, Roman Engel-Herbert, B. Jalan, Joël Cagnon, P. Moetakef, Susanne Stemmer, and G. B. Stephenson. Stoichiometry optimization of homoepitaxial oxide thin films using x-ray diffraction. *Appl. Phys. Lett.*, 95(14):142905, 2009.

[170] Carol Thompson, Christopher M. Foster, J. A. Eastman, and G. B. Stephenson. Observation of the polarization of domains in ferroelectric thin films using x-ray interference. *Appl. Phys. Lett.*, 71(24):3516–3518, 1997.

[171] Gilles Renaud, Rémi Lazzari, and Frédéric Leroy. Probing surface and interface morphology with Grazing Incidence Small Angle X-Ray Scattering. *Surf. Sci. Rep.*, 64(8):255–380, 2009.

[172] R Takahashi, Y Matsumoto, T Ohsawa, M. Lippmaa, M. Kawasaki, and H. Koinuma. Growth dynamics of the epitaxial SrO film on $SrTiO_3$(001). *J. Cryst. Growth*, 234(2):505–508, 2002.

[173] A. Ohtomo and H. Y. Hwang. A high-mobility electron gas at the $LaAlO_3/SrTiO_3$ heterointerface. *Nature*, 427(6973):423–426, 2004.

[174] W. M. Lü, X. Wang, Z. Q. Liu, S. Dhar, A. Annadi, K. Gopinadhan, A. Roy Barman, H. B. Su, T. Venkatesan, and Ariando. Metal-insulator transition at a depleted $LaAlO_3/SrTiO_3$ interface: Evidence for charge transfer induced by $SrTiO_3$ phase transitions. *Appl. Phys. Lett.*, 99(17):172103, 2011.

[175] Guneeta Singh-Bhalla, Christopher Bell, Jayakanth Ravichandran, Wolter Siemons, Yasuyuki Hikita, Sayeef Salahuddin, Arthur F. Hebard, Harold Y. Hwang, and Ramamoorthy Ramesha. Built-in and induced polarization across $LaAlO_3/SrTiO_3$ heterojunctions. *Nat. Phys.*, 7(1):80–86, 2011.

[176] N. Reyren, S. Thiel, A. D. Caviglia, L. Fitting Kourkoutis, G. Hammerl, C. Richter, C. W. Schneider, T. Kopp, A.-S. Rüetschi, D. Jaccard, M. Gabay, D. A. Muller, J.-M. Triscone, and J. Mannhart. Superconducting Interfaces Between Insulating Oxides. *Science*, 317(5842):1196–1199, 2007.

[177] A. Brinkman, M. Huijben, M. van Zalk, J. Huijben, U. Zeitler, J. C. Maan, W. G. van der Wiel, G. Rijnders, D. H. A. Blank, and H. Hilgenkamp. Magnetic effects at the interface between non-magnetic oxides. *Nat. Mater.*, 6(7):493–496, 2007.

[178] Jian Liu, S. Okamoto, M. van Veenendaal, M. Kareev, B. Gray, P. Ryan, J. W. Freeland, and J. Chakhalian. Quantum confinement of Mott electrons in ultrathin $LaNiO_3/LaAlO_3$ superlattices. *Phys. Rev. B*, 83(16):161102(R), 2011.

[179] R. Scherwitzl, S. Gariglio, M. Gabay, P. Zubko, M. Gibert, and J.-M. Triscone. Metal-Insulator Transition in Ultrathin $LaNiO_3$ Films. *Phys. Rev. Lett.*, 106(24):246403, 2011.

[180] Michel Crespin, Pierre Levitz, and Lucien Gatineau. Reduced Forms of $LaNiO_3$ Perovskite. Part 1.—Evidence for New Phases: $La_2Ni_2O_5$ and $LaNiO_2$. *J. Chem. Soc. Faraday Trans. 2*, 79(8):1181, 1983.

[181] José Antonio Alonso and María Jesús Martínez-Lope. Preparation and Crystal Structure of the Deficient Perovskite $LaNiO_{2.5}$, Solved From Neutron Powder Diffraction Data. *J. Chem. Soc. Dalton Trans.*, 1995(17):2819, 1995.

[182] R. D. Sánchez, M. T. Causa, A. Caneiro, A. Butera, M. Vallet-Regí, M. J. Sayagués, J. González-Calbet, F. García-Sanz, and J. Rivas. Metal-insulator transition in oxygen-deficient $LaNiO_{3-x}$ perovskites. *Phys. Rev. B*, 54(23):16574, 1996.

[183] Masanori Kawai, Satoru Inoue, Masaichiro Mizumaki, Naomi Kawamura, Noriya Ichikawa, and Yuichi Shimakawa. Reversible changes of epitaxial thin films from perovskite $LaNiO_3$ to infinite-layer structure $LaNiO_2$. *Appl. Phys. Lett.*, 94(8):082102, 2009.

[184] R. Baudoing-Savois, M. De Santis, M. C. Saint-Lager, P. Dolle, O. Geaymond, P. Taunier, P. Jeantet, J. P. Roux, G. Renaud, A. Barbier, O. Robach, O. Ulrich, A. Mougin, and G. Bérard. A new UHV diffractometer for surface structure and real time molecular beam deposition studies with synchrotron radiations at ESRF. *Nucl. Instrum. Meth. B*, 149(1):213–227, 1999.

[185] Bernd Jenichen, Wolfgang Braun, Vladimir M. Kaganer, Alexander G. Shtukenberg, Lutz Däweritz, Carl-Günther Schulz, Klaus H. Ploog, and Alexei Erko. Combined molecular beam epitaxy and diffractometer system for in situ x-ray studies of crystal growth. *Rev. Sci. Instrum.*, 74(3):1267, 2003.

[186] P. R. Willmott, C. M. Schlepütz, B. D. Patterson, R. Herger, M. Lange, D. Meister, D. Maden, Ch. Brönnimann, E. F. Eikenberry, G. Hülsen, and A. Al-Adwan. In situ studies of complex PLD-grown films using hard X-ray surface diffraction. *Appl. Surf. Sci.*, 247(1-4):188–196, 2005.

[187] R.-V. Wang, G. B. Stephenson, D. D. Fong, F. Jiang, P. H. Fuoss, J. A. Eastman, S. K. Streiffer, K. Latifi, and Carol Thompson. Real time x-ray observation of lattice pulling during growth of epitaxial $Pb(Zr,Ti)O_3$ films. *Appl. Phys. Lett.*, 89(22):221914, 2006.

APPENDIX A

Notes on Oxide MBE Growth Details

A.1. Oxide substrate preparation

Substrate preparation is a very important step to achieve the successful growth of epitaxial thin films since the quality of the substrate surface, which acts as a template for the epitaxial growth, will affect that of the films grown on. The substrate for thin film growth needs to have an atomically smooth surface and a known atomic layer complete termination. The following is the substrate preparation recipe for $SrTiO_3$ (001). The TiO_2-terminated (001) $SrTiO_3$ substrates were prepared by the recipe from G. Koster [58]:

1. Clean $SrTiO_3$ substrates in acetone, isopropanol, and deionized (DI) water for ~ 10 min in each solution in ultrasonic.
2. Etch in Buffered hydrofluoric acid (BHF) for 30 sec (this step will remove SrO and leave single TiO_2-terminated surface).
3. Rinse in DI water and blow dry with nitrogen gas.
4. Anneal $SrTiO_3$ substrates in dedicated tube furnace in flowing 99.994% pure O_2 atmosphere (UHP oxygen) at 950 °C for 1 hr.

A.2. Sample Preparation

1. Mount substrates on the substrate plates using silver paint.
2. Heat the substrate plate at 200 °C for 10 min.
3. Cool down for another 10 min.

A.3. Quartz Crystal Microbalance (QCM)

MBE deposition of certain materials requires that the elemental sources be supplied to the surface in the correct ratio to create a film of the desired stoichiometry. This can be a challenging task, especially for multi-component materials. The stoichiometry control, to the first order, is calibrated using a quartz crystal microbalance (QCM) that is placed in front of the substrate. This microbalance determines the fluxes of the individual molecular beams and is also used to check the stability of the individual sources.

The temperature of the sources is adjusted using the QCM so that the fluxes of the individual molecular beams correspond to a 200 $\sim$ 300 seconds for one monolayer coverage of the substrate at the position for X-ray diffraction. Calibration with the QCM typically gives an accuracy of $\pm 5\%$.

A.4. Metal Sources

The strontium source was a Veeco low temperature effusion cell loaded with 99.99% pure strontium dendritic metal pieces in a pyrolytic boron nitride (pBN) crucible. The usual evaporation temperature of Sr is around 385 °C to get desired flux.

The titanium source was a Mini Ti-Ball^{TM}. The usual evaporation temperature of Ti was 44 $\sim$ 46 A depends on the condition of the Ti-Ball. Increase the temperature slowly when heat up the Ti-Ball.

The lanthanum source was a Veeco high temperature effusion cell loaded with 99.9% pure lanthanum metal rods Lanthanum rod (6.35mm (0.25in) dia $\times$ 25mm length) in a W crucible. The usual evaporation temperature of La is around 1350 °C to get desired flux. Since the melting point (M.P.) of La is around 920 °C, change the temperature of the effusion cell slowly aross the M.P. Set the ramp rate to 2 °C/min or lower when the temperature is M.P.$\pm$100°C.

The nickel source was a Veeco high temperature effusion cell loaded with 99.995% pure nickel metal slugs in an alumina crucible. The usual evaporation temperature of Ni is around 1130 °C to get desired flux.

A.5. Oxidation

To oxidize the films, a molecular beam consisting of pure oxygen, pure ozone, or a mixture of oxygen and ozone ($\sim$ 10% O_3) was used. The mixture was produced by passing pure oxygen through an ozone generator, and its output flowed continuously into the chamber through a leak valve travels down a water-cooled electropolished stainless steel tube that is directed perpendicular and close to the substrate surface.

During growth, the background pressure of the chamber was increased with this O_2/O_3 mixture from a base pressure of $\sim 5 \times 10^{-7}$ to 9×10^{-6} torr. This pressure was maintained after growth until the sample had cooled to room temperature to limit oxygen vacancies in the deposited film.

A.5.1. 10% Ozone operation

To turn ON the ozone system:

Make sure Oxygen cylinder is open.

1. Open Delivery (generally open)
2. Open Collect
3. Stop Pump
4. Close Roughing
5. Turn on the ozone generator
6. Slowly increase output power to 100%
7. Open leak valve

To turn OFF the ozone system:

1. Close All-metal valve
2. Slowly decrease output power to 0% 3. Turn off the ozone generator
4. Wait few minutes
5. Start Pump and open Roughing (Once you press roughing, the exhaust valve on roughing line is closed.)
6. Close Collect
7. Close Oxygen cylinder
8. Open Green valve on the line

A.5.2. 100% Ozone operation

A. Set up:

Assemble Silica gel and connect everything, this includes Pt100 thermometer, resistance heater, LN2 Level controllers LC-10, camera, oxygen lines, oxygen valves, and nitrogen lines.

B. Bake out:

1. Go to "Start Up" mode. (It should automatically start roughing pump.)
2. Set the setpoint of the still to 90°C.
3. Bake the still until the pressure of the still below 50 mTorr.
4. Pump the thermal insulation part of liquid nitrogen reservoir.
5. Go to "Service" mode (F1+F3 on the panel display)
6. Open the delivery valve to pump the delivery line (connection pipe to chamber) as well

C. Cool down:

1. After bake out, set the still to 20°C.
2. Wait until the still cools down to room temperature.
3. Turn on nitrogen cylinder to flow dry N_2 to the camera. (The regulator of the nitrogen cylinder should be $\sim$ 15 psi to avoid water condenses on the camera and outside of the stiller.)
4. Fill the liquid nitrogen (LN2) reservoir. (With about 3/4 turn on the LN2 dewar, the LN2 reservoir will be full in $\sim$ 8 mins.)
5. Go to "Start Up" mode.
6. Set the setpoint of the still to −155°C and "START." (Now it should open the valve

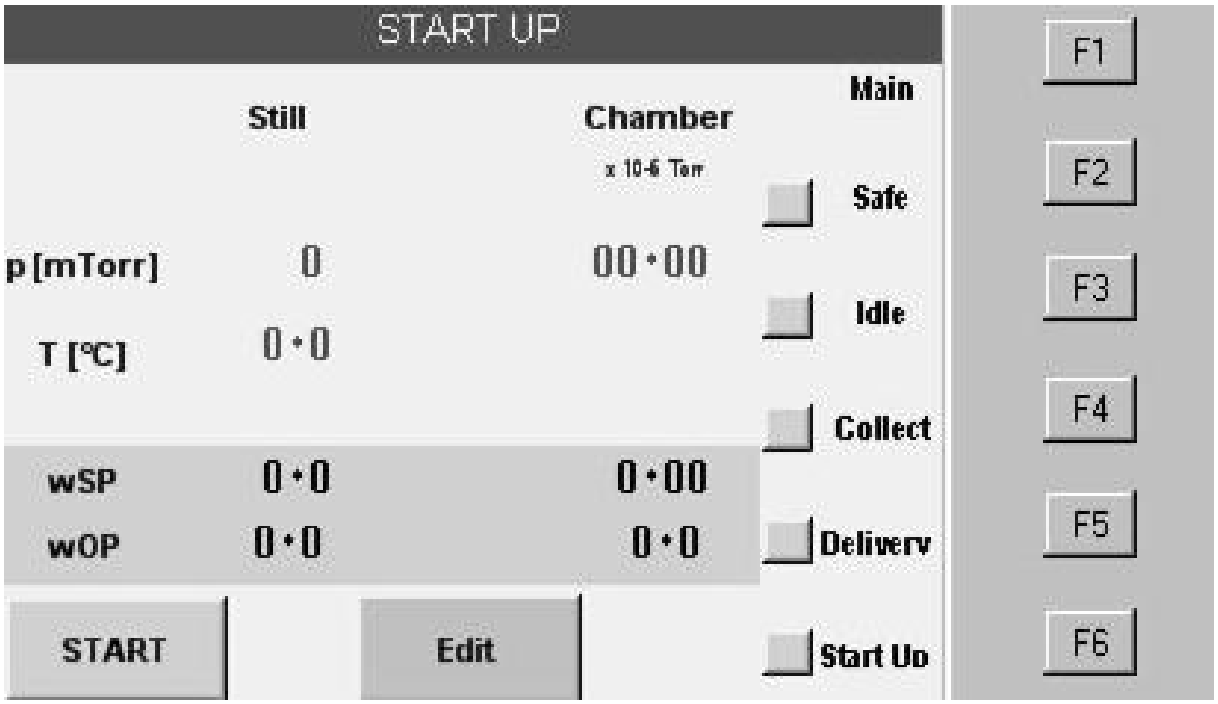

Figure A.1. Start Up mode screen

between the LN2 container which contains the still and LN2 reservoir and start to cool down the system.)

7. After the system is reached the setpoint, refill the LN2 reservoir again to make sure it is full .

D. Collect :

Make sure Oxygen cylinder is open.

1. Turn on the ozone generator.

2. Slowly increase output power to 100%. (Both lights on the ozone generator should be on, indicating that the ozone generator is now under remote control and not enabled yet.)

3. Switch to “Collect” mode.

- The valve between the ozone generator and the still should be open as displayed on the computer (Figure A.2).
- Check the oxygen flow meter again and adjust to the flow to be 15 psi.
- One light on the generator should be off now, indicating ozone generator is enabled.

6. Typical collect time is 20 $\sim$ 30 mins. (Monitor the color of the still, the silica gel should become deep purple (Figure A.4) indicating the presence of ozone. The still temperature will increase to about $-127°$C.

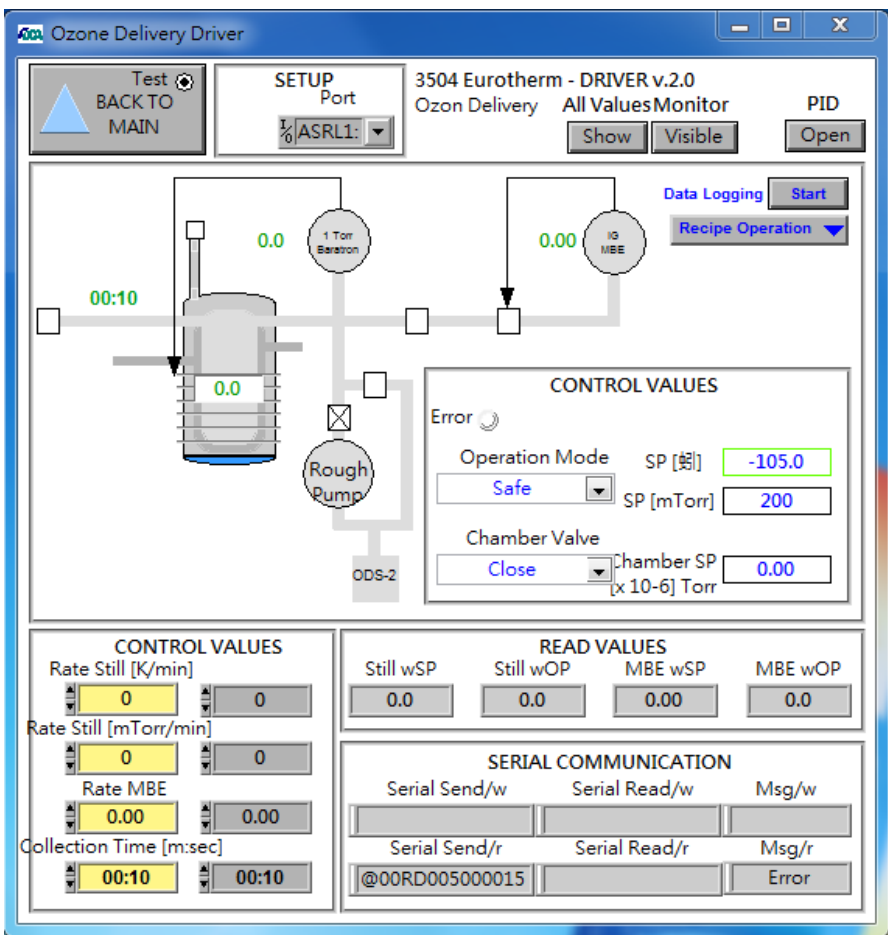

Figure A.2. DCA software

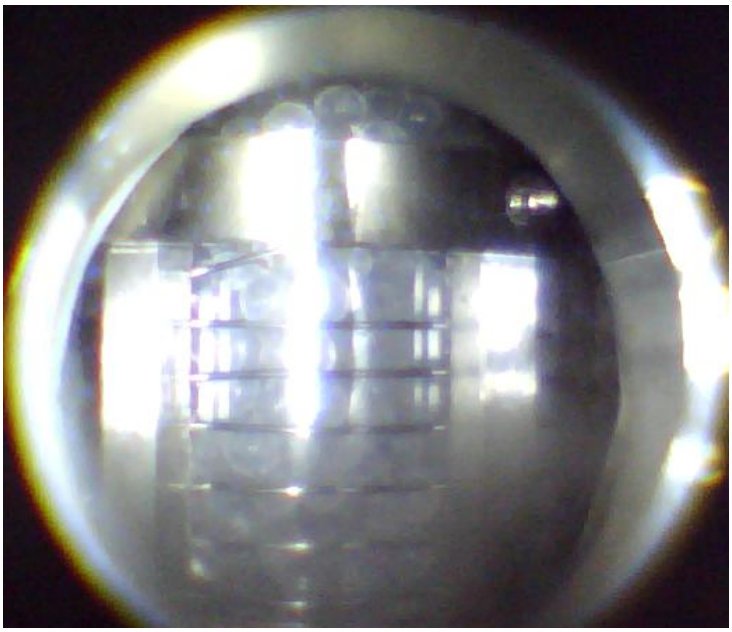

Figure A.3. Still Image before accumulation

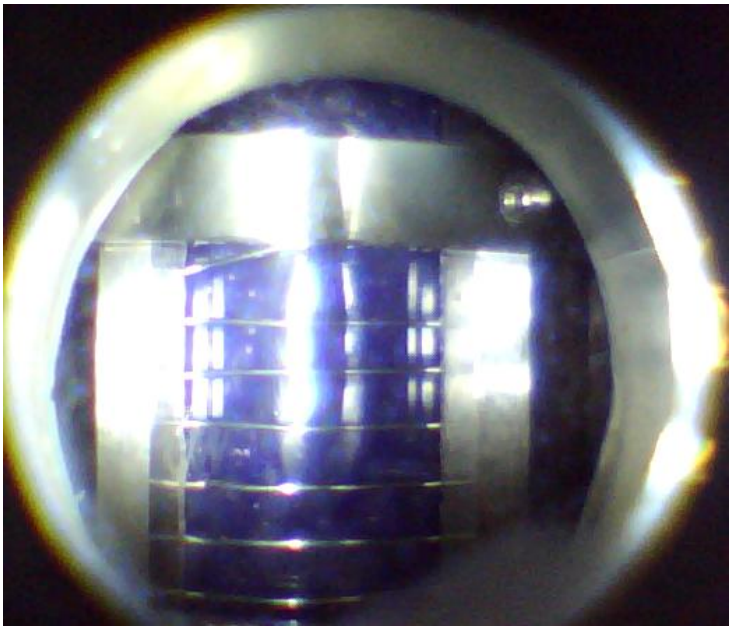

Figure A.4. Still Image after accumulated for 30 min

E. Idle:

1. After the ozone collection finished, the system will automatically switch to “Idle” mode.

2. The pump will be switched back on to pump the system.

3. Slowly decrease the output power of the ozone generator to 0% and turn it off.

4. Turn off the oxygen line as well.

5. Wait until the still pressure below 100 mTorr. (It might take a while.)

6. After the still pressure has dropped down, gradually tune the setpoint of the still temperature to get the still pressure around 150 mTorr.

F. Delivery :

⋆ Make sure the leak valve on the chamber is close.

1. Go to “Delivery” mode.

2. Open the ”Chamber Valve’ on the computer (Figure A.2).

- Note: The ”Chamber Valve’ actually doesn’t exist in our system. We took it out because it affected the ozone concentration delivered to the oxide MBE chamber.

3. Put the still pressure setpoint to the current still pressure value ($\sim$ 150 mTorr) and put the chamber pressure setpoint to the desire value.

4. Carefully open the leak valve to increase the chamber pressure to desired value. (typically no more than 1×10^{-6} Torr)

5. In principle, the chamber pressure could be varied either by tuning the still pressure or manually adjusting the leak valve on the chamber.

- Make sure the dry N2 line is always maintained at 15 psi.
- The LN2 reservoir should be refilled every 1.5 hours for $\sim$ 8 mins.

- The still pressure and temperature should be checked from time to time to make sure the ozone supply system is stable.

G. Kill ozone:

1. Close the "Chamber Valve'.

2. Switch to "Safe" mode.

3. Load and start the bake out recipe. (Make sure the dry N_2 line will continue to flow during the slowly warming up process.)

Vita

Education:

Ph.D. Northwestern University, Evanston, IL, U.S.A.

Materials Science and Engineering, expected Dec 2014

Advisor: Prof. Michael J. Bedzyk; Dr. John W. Freeland

GPA: 3.82/4.00

M.S. National Taiwan University, Taipei, Taiwan

Electronics Engineering, 2007

Dissertation: The Mechanisms of Electric-Field-Directed Growth of Silicon Nanowires

GPA: 4.00/4.00

B.S. National Taiwan University, Taipei, Taiwan

Materials Science and Engineering, 2005

GPA: 3.77/4.00

Research Experience:

Jan 2010–present Graduate Research Assistant

Advisor: Dr. John W. Freeland

Magnetic Materials Group, Advanced Photon Source,

Argonne National Laboratory

- Synchrotron Surface X-ray Diffraction and Synchrotron X-ray Absorption Spectroscopy, X-ray Magnetic Circular Dichroism (XMCD).
- Understanding the magnetic and electronic properties of complex oxides both in the bulk and at surfaces and interfaces.
- Novel oxide thin film growth using reactive molecular beam epitaxy (MBE).
- Ultra-high vacuum (UHV) work, maintenance of the *in situ* oxide MBE system at Sector 33 of Advanced Photon Source.

Teaching Experience:

Winter 2011,2012 Teaching Assistant

Department of Materials Science and Engineering,

Northwestern University

MAT SCI 361-Crystallography and Diffraction

- Instructor: Prof. Michael Bedzyk
- Helped professor create course materials, teach lab and grade homework

Awards and Honors:

Dec 2014	Material Research Society Graduate Student Silver Award
Mar 2014	American Physical Society Ovshinsky Student Travel Award
2007	Member of The Phi Tau Phi Scholastic Honor Society of Republic of China
2001, 2005	Presidential Award, National Taiwan University (NTU), Taipei, Taiwan

Publications:

(1) I. C. Tung, G. Luo, J. H. Lee, S. H. Chang, D. Morgan, H. Hong, D. D. Fong, M. J. Bedzyk, J. W. Freeland, "Effect of Polar Discontinuity on the Growth of Epitaxial $LaNiO_3$ Ultrathin Films", (In Preparation).

(2) I. C. Tung, G. Luo, Z. L. Luo, J. H. Lee, S. H. Chang, D. Morgan, H. Zhou, H. Hong, M. J. Bedzyk, J. W. Freeland, D. D. Fong, "Time-resolved in-situ X-ray Study of Homoepitaxial $SrTiO_3$ Growth Using Reactive Molecular-Beam Epitaxy", (In Preparation).

(3) J. H. Lee, G. Luo, I. C. Tung, S. H. Chang, Z. Luo, M. Malshe, M. Gadre, A. Bhattacharya, S. M. Nakhmanson, J. A. Eastman, H. Hong, J. Jellinek, D. Morgan, D. D. Fong, and J. W. Freeland, "Dynamic layer rearrangement during growth by oxide molecular beam epitaxy", *Nat. Mater.* **13**, 879 (2014).

(4) I. C. Tung, P. V. Balachandran, Jian Liu, B. A. Gray, E. A. Karapetrova, J. H. Lee, J. Chakhalian, M. J. Bedzyk, J. M. Rondinelli, J. W. Freeland, "Connecting bulk symmetry and orbital polarization in strained $RNiO_3$ ultrathin films", *Phys. Rev. B* **88**, 205112 (2013).

(5) J. Hoffman, I. C. Tung, B. Nelson-Cheeseman, M. Liu, J. W. Freeland, A. Bhattacharya, "Charge transfer and interfacial magnetism in $(LaNiO_3)_n/(LaMnO_3)_2$ superlattices", *Phys. Rev. B* **88**, 144411 (2013).

(6) D. Meyers, E. J. Moon, M. Kareev, I. C. Tung, B. A. Gray, J. Liu, M. J. Bedzyk, J. W. Freeland, J. Chakhalian, "Epitaxial stabilization of ultra-thin films of $EuNiO_3$", *J. Phys. D: Appl. Phys.* **46**, 385303 (2013).

(7) H. J. Jeen, W. S. Choi, M. D. Biegalski, C. M. Folkman, I. C. Tung, D. D. Fong, J. W. Freeland, D. Shin, H. Ohta, M. F. Chisholm, H. N. Lee, "Reversible redox reactions in an epitaxially stabilized $SrCoO_x$ oxygen sponge", *Nat. Mater.* **12**, 1057 (2013).

(8) B. A. Gray, E. J. Moon, I. C. Tung, M. Kareev, Jian Liu, D. J. Meyers, M. J. Bedzyk, J. W. Freeland, J. Chakhalian, "Enhanced Spin and Electronic Reconstructions at the Cuprate-Manganite Interface", arXiv:1301.3736.

(9) J. Chakhalian, J. M. Rondinelli, J. Liu, B. A. Gray, M. Kareev, E. J. Moon, N. Prasai, J. L. Cohn, M. Varela, I. C. Tung, M. J. Bedzyk, S. G. Altendorf, F. Strigari, B. Dabrowski, L. H. Tjeng, P. J. Ryan, J. W. Freeland, "Asymmetric orbital-lattice interactions in ultrathin correlated oxide films", *Phys. Rev. Lett.* **107**, 116805 (2011).

Selected Conference Presentations

(1) "Real-Time X-Ray Study of Structural Evolution during Layer-by-Layer Growth of $SrTiO_3$", Oral Presentation, Materials Research Society Fall Meeting, December 2014, Boston, MA.

(2) "Effect of Polar Discontinuity on the Growth of Epitaxial $LaNiO_3$ Ultrathin Films", Oral Presentation, American Physical Society March Meeting, March 2014, Denver, CO.

(3) "Time-resolved in-situ X-ray Study of Homoepitaxial $SrTiO_3$ Growth Using Reactive Molecular-Beam Epitaxy", Poster Presentation, Materials Research Society Spring Meeting, April 2013, San Francisco, CA.

(4) "Influence of Symmetry on the Octahedral Rotations of Epitaxial $RNiO_3$ Thin Films", Oral Presentation, American Physical Society March Meeting, February 2012, Boston, MA.

(5) "Structural Effects on the Electronic Properties of Epitaxially Strained $RNiO_3$ Thin Films", Oral Presentation, American Physical Society March Meeting, March 2011, Dallas, TX.

Skills:

(1) Languages: Chinese, English

(2) Technical Software: Matlab, Maple, Mathematica, Igor, LabView, LaTeX

(3) Programming Languages: C/C++, Visual Basic

Membership:

- American Physical Society
- Materials Research Society